

DYNAMICS OF THE TURKISH STRAITS SYSTEM :A NUMERICAL STUDY  
WITH A FINITE ELEMENT OCEAN MODEL BASED ON AN  
UNSTRUCTURED GRID APPROACH

A THESIS SUBMITTED TO  
THE GRADUATE SCHOOL OF MARINE SCIENCES  
OF  
MIDDLE EAST TECHNICAL UNIVERSITY

BY

ÖZGÜR GÜRSES

IN PARTIAL FULFILLMENT OF THE REQUIREMENTS  
FOR  
THE DEGREE OF DOCTOR OF PHILOSOPHY  
IN  
PHYSICAL OCEANOGRAPHY

MARCH 2016



Approval of the thesis:

**DYNAMICS OF THE TURKISH STRAITS SYSTEM :A NUMERICAL STUDY  
WITH A FINITE ELEMENT OCEAN MODEL BASED ON AN  
UNSTRUCTURED GRID APPROACH**

submitted by **ÖZGÜR GÜRSES** in partial fulfillment of the requirements for the degree of **Doctor of Philosophy in Physical Oceanography Department, Middle East Technical University** by,

Prof. Dr. Ahmet Kideyş  
Dean, Graduate School of **Marine Sciences**

\_\_\_\_\_

Prof. Dr. Ahmet Kideyş  
Head of Department, **Physical Oceanography**

\_\_\_\_\_

Prof. Dr. Emin Özsoy  
Supervisor, **Oceanography Department, METU**

\_\_\_\_\_

**Examining Committee Members:**

Prof. Dr. Emin Özsoy  
Oceanography Department, METU

\_\_\_\_\_

Assoc. Prof. Dr. Bettina Andrea Fach Salihoğlu  
Oceanography Department, METU

\_\_\_\_\_

Assist. Prof. Dr. Şadi Sinan Arkin  
Oceanography Department, METU

\_\_\_\_\_

Assoc. Prof. Dr. Murat Gündüz  
Institute of Marine Sciences and Technology, DEU

\_\_\_\_\_

Assoc. Prof. Dr. Ufuk Utku Turunçoğlu  
Informatics Institute, ITU

\_\_\_\_\_

**Date:**

\_\_\_\_\_



**I hereby declare that all information in this document has been obtained and presented in accordance with academic rules and ethical conduct. I also declare that, as required by these rules and conduct, I have fully cited and referenced all material and results that are not original to this work.**

Name, Last Name: ÖZGÜR GÜRSES

Signature :



# ABSTRACT

## DYNAMICS OF THE TURKISH STRAITS SYSTEM :A NUMERICAL STUDY WITH A FINITE ELEMENT OCEAN MODEL BASED ON AN UNSTRUCTURED GRID APPROACH

Gürses, Özgür

Ph.D., Department of Physical Oceanography

Supervisor : Prof. Dr. Emin Özsoy

March 2016, 141 pages

This thesis presents the application of the finite element ocean model to the Turkish Strait System (TSS) which connects the two nearly-enclosed marginal water bodies of the Black and Mediterranean Seas through the narrow, non-straight and elongated Bosphorus and Dardanelles Straits and the Marmara Sea in between.

The Turkish Strait System is a key gateway between the Black and the Mediterranean Seas and includes narrow channels where two-layer exchange flow develops.

Being the only salt source in the Black Sea and additional brackish water source in the North Aegean Basin, TSS poses wide range of physical processes in temporal and spatial scale. Adequate and effective numerical representation of this large spectrum is a grand challenge and still beyond today's classical Ocean General Circulation Models (OGCM). In this work, we focused on a new regional implementation of an unstructured mesh based multi-resolution ocean model (the Finite Element Ocean Model, FEOM) with refinement up to  $\sim 65$  m in its connecting straits while keeping a coarse resolution no more than  $\sim 1,6$  km in the Marmara Sea and  $\sim 5$  km setup in the adjacent reservoirs. This model forms the basis of hindcast simulations in conjunction with sensitivity experiments for the year 2008.

Nonlinear hydraulic transitions and stratified turbulent exchange flow through the nar-

row straits and over steep topography exemplifies the complexity in the Turkish Strait System. Correct reproduction of such processes in this region strictly depends on the accuracy of the topography as well as the complex coastal geometry. Consequently, a new bathymetry is produced by merging available data sets of different sources, such as multi-beam surveys or the digitized information from the bathymetric charts. ArcGIS software provided necessary tools for the extraction of the consistent coastal information.

Unlike a few previous studies, this is the first comprehensive study enabling the representation of the entire TSS without nesting. Thanks to its that multi-resolution flexibility and numerically efficient algorithm, FEOM is a versatile alternative not only for global climate studies but also for regional oceanographic applications.

We perform a-year long simulations that were forced with the realistic atmosphere of the year 2008, the period of available data. The results are assessed by focusing mostly on stability of the pycnocline and the variability of the volume transports across the Bosphorus and Dardanelles. The Black Sea freshwater input is a key element to obtain correct stratification in the Marmara Sea as well as the Bosphorus volume fluxes. The model captures the flow reversal of the upper layer, so-called Orkoz, during the passage of southwesterly storms over the region. Hindcast results are compared to observational datasets (partly independent) collected over two months (April and October 2008).

Hindcast simulations includes almost all forcing functions in the system. It is of importance to assess the model response to various coefficients and forcing perturbations. Therefore, series of simulations are presented which are based on idealized lock-exchange initial conditions. Numerical calculations show that the main circulation patterns are produced well and consistent with previous modeling and observational studies. The interface which is the region of rapid salinity and temperature change between quasi-homogeneous upper and lower layers is sloped steeply throughout the Bosphorus and the Dardanelles Straits indicating that mass and momentum transfer between the these layers are important.

**Keywords:** Turkish Strait System, Finite Element Ocean Modeling, Unstructured Grid

# ÖZ

## TÜRKÇE TEZ BAŞLIĞI

Gürses, Özgür

Doktora, Fiziksel Oşinografi Bölümü

Tez Yöneticisi : Prof. Dr. Emin Özsoy

Mart 2016 , 141 sayfa

Bu tez, sonlu elemanlar okyanus modelinin neredeyse kapalı Karadeniz ve Akdeniz su kütlelerini düz-olmayan ve uzun İstanbul ve Çanakkale Boğazları ile bunların arasındaki Marmara Denizi aracılığıyla bağlayan Türk Boğazlar Sistemine (TBS) tatbikini sunar.

Türk Boğazları Sistemi, Karadeniz ve Akdeniz arasında önemli bir geçittir ve iki tabakalı iki yönlü akımların geliştiği dar kanalları kapsar.

Karadeniz'deki tek tuz kaynağı ve Kuzey Ege Havzası'ndaki az tuzlu su kaynağı olarak TBS zamansal ve mekansal ölçekte çok çeşitli fiziksel süreçleri ortaya çıkarır. Bu geniş bir yelpazede yeterli ve etkili sayısal gösterim büyük bir çaba gerektirir ve hala bugünün klasik Okyanus Genel Sirkülasyon Modellerinin (OGSM) ötesindedir. Bu çalışmada, düşük çözünürlük yapısını Marmara Denizi'de 1,6 km'yi geçirmeyip bitişik rezervuarlarda 5 km'de tutarken bunları bağlayan Boğazlarda yaklaşık 65 m'ye kadar rafine eden yapısal olmayan model ağ tabanlı, çoklu çözünürlüklü okyanus modelinin (the Finite Element Ocean Model, FEOM) yeni bir bölgesel uygulamasına odaklandık. Bu model 2008 yılı için duyarlılık deneyleri ile birlikte hindcast simülasyonlarının temelini oluşturur.

Doğrusal olmayan hidrolik geçişler ve dar boğazlarından ve sarp topografya üzerinden tabakalı türbülanslı değişim akışı Türk Boğazları Sistemde karmaşıklığın örneği-

dir. Bu işlemlerin bu bölgede yeniden doğru üretimi tam anlamıyla topografya doğruluğuna ve karmaşık kıyı geometrisine bağlıdır. Sonuç olarak, çok ışınlı deniz araştırmaları veya sayısallaştırılmış batimetrik çizelge bilgileri gibi farklı kaynaklardan, mevcut veri setleri birleştirilmesi ile yeni bir batimetri üretilmiştir. ArcGIS yazılımı tutarlı kıyı bilgilerin çıkarılması için gerekli araçları sağladı.

Daha önceki birkaç çalışmadan farklı olarak bu çalışma yuvalama tekniği olmadan tüm TSS temsiliyi sağlayan ilk kapsamlı çalışmadır. Çoklu çözünürlük esnekliği ve sayısal verimli algoritma sayesinde FEOM sadece küresel iklim çalışmaları için değil, aynı zamanda bölgesel oşinografik uygulamalar için de çok yönlü bir alternatiftir.

Mevcut verilere dönemi olan 2008 yılının gerçekçi atmosfer kuvveti ile bir yıllık uzun simülasyonlar gerçekleştirildi. Sonuçlar çoğunlukla piknoklin ve İstanbul ve Çanakkale Boğazı boyunca hacim taşımaları değişkenliği istikrarı odaklanarak değerlendirildi. Karadeniz tatlı su girişi Marmara Denizi'nde doğru tabakalaşmanın yanı sıra boğaz hacim akılarını da elde etmek için önemli bir unsurdur. Model bölge üzerinde güneybatıya fırtınalar geçişi sırasında üst tabakanın tersine akışını, Orkoz denilen, yakalar. Hindcast sonuçları iki ayda (Nisan ve Ekim 2008) toplanan gözlemsel veri setleri (kısmen bağımsız) ile karşılaştırılmıştır.

Hindcast simülasyonları sistemdeki hemen hemen tüm kuvvet fonksiyonlarını içerir. Modelin çeşitli katsayıları ve kuvvet dengesizliklerine tepkisini değerlendirmek önem taşımaktadır. Bu nedenle, idealize edilmiş kilit-değişimi başlangıç koşullarına dayalı bir dizi simülasyon sunulmuştur. Sayısal hesaplamalar, üretilen ana dolaşım şekli önceki modelleme ve gözlemsel çalışmalarıyla tutarlı olduğunu göstermektedir. Yarı-homojen üst ve alt katmanları arasındaki hızlı tuzluluk ve sıcaklık değişiminin olduğu arayüzeyin İstanbul ve Çanakkale boğazları boyunca dik eğimi bu katmanlar arasındaki kütle ve momentum transferinin önemli olduğunu belirtir.

**Anahtar Kelimeler:** Türk Boğazlar Sistemi, Sonlu Elemanlar Okyanus Modeli, Farklı Tipolojiye Sahip Çözüm Ağı



*to my families*

## ACKNOWLEDGMENTS

I am grateful to my supervisor Prof. Dr. Emin Özsoy for making the opportunity for me to take part at the Physical Oceanography Group under the Institute of Marine Sciences (IMS) - Middle East Technical University (METU) and for his encouragement, enthusiasm and guidance in assisting me throughout this challenging research study.

I would like to thank Prof Dr. Ahmet Erkan Kideyş and Assoc. Prof. Dr. Barış Salihoğlu letting me to conduct my research at IMS-METU.

I thank my committee members Assoc. Prof. Bettina Andrea Fach Salihoğlu, Assoc. Prof. Murat Gündüz, Assoc. Prof. Ufuk Utku Turunçoğlu and Assist. Prof. Şadi Sinan Arkin for insight, suggestions and support.

Albeit different sources, CTD, ADCP and bathymetry data I used during my work are kindly provided by IMS-METU based on ship time on the R/V Bilim and I am grateful to all the staff for their collaboration and contributions.

I have enjoyed my time at Alfred Wegener Institute (AWI) where I adopted the Finite Element Ocean Modeling (FEOM) to the Turkish Strait System (TSS). I thank Dr. Ralph Timmermann and members of the Climate Dynamics group for their refreshing comments during the discussion sessions.

I am not able to list all the people at the Istituto Nazionale di Geofisica e Vulcanologia (INGV) contributed this study, but I want to especially thank Prof. Nadia Pinardi for constructive comments and Mr. Ali Aydoğdu who put effort on extension of this study. I will always remember them.

And, special thanks go to my other colleagues and friends at IMS-METU, AWI and INGV who made my time enjoyable.

And, most importantly, none of this would have been possible without the love of my family.

Finally, I am deeply grateful to my wife Claudia for her patience, support and care.

This study was funded by numerous projects such as the bilateral research project 111Y344 entitled ‘High Reynolds Number Turbulent Mixing in Bosphorus Strait’ supported by the Turkish Scientific and Technical Research Council (TÜBİTAK) and the travel support jointly provided by the German Ministry of Education during 2012-

2014. I also acknowledge the support obtained through Helmholtz Association during my research time at AWI. Besides, I would like to thank to INGV for its support through the FP7 project under the MyOcean2 ve MyOcean Follow projects devoted to operate the Ocean Monitoring and Forecasting component of the GMES Marine Service (OMF/GMS) during 2012/2015. The data from the MOMA <sup>1</sup> (Meteoroloji / Oşinografi Mükemmeliyet Ağı Projesi) real-time network of sensors and instrumentation, satellite remote sensing, the archive of oceanographic data of the IMS and of the currently running projects were made available for this study.



---

<sup>1</sup> <http://moma.ims.metu.edu.tr>

## TABLE OF CONTENTS

ABSTRACT . . . . .	v
ÖZ . . . . .	vii
ACKNOWLEDGMENTS . . . . .	x
TABLE OF CONTENTS . . . . .	xii
LIST OF TABLES . . . . .	xv
LIST OF FIGURES . . . . .	xvi
LIST OF ABBREVIATIONS . . . . .	xxii
CHAPTERS	
1 INTRODUCTION . . . . .	1
2 GENERAL CHARACTERISTICS . . . . .	9
2.1 Geometric Features . . . . .	9
2.2 Assembling the fine resolution bathymetry of the Turkish Straits System . . . . .	12
2.3 Hydrographic Characteristics . . . . .	13
2.4 Review of earlier modeling efforts . . . . .	27
3 FINITE ELEMENT OCEAN MODEL . . . . .	33
3.1 Governing Equations . . . . .	34



3.2	Mesh Generation . . . . .	36
3.2.1	2D Mesh (Surface Mesh) . . . . .	37
3.2.2	3D Mesh . . . . .	38
3.3	Mathematical structure . . . . .	39
3.3.1	Characteristic Galerkin Method . . . . .	41
3.3.2	Momentum and vertically integrated continuity . . . . .	43
3.3.2.1	Matrix form . . . . .	45
3.3.3	Vertical velocity . . . . .	48
3.3.4	Biharmonic Viscosity . . . . .	51
3.3.5	Boundary Conditions on Rigid Walls . . . . .	52
3.3.6	Temperature and salinity . . . . .	53
4	MODEL SIMULATIONS . . . . .	57
4.1	Parameterization of subgrid-scale processes . . . . .	57
4.2	Initial and Boundary Conditions . . . . .	60
4.2.1	Model setup with Atmospheric forcing . . . . .	63
4.2.2	Wind Field . . . . .	63
4.2.3	Surface Heat Flux . . . . .	64
4.2.4	Correction of atmospheric forcing fields against land contamination . . . . .	68
4.2.5	Model Setup With Black Sea Net Flux . . . . .	69
5	TSS LOCK-EXCHANGE MODEL WITH IDEALIZED INITIAL CONDITIONS . . . . .	73

5.1	The BASIC Experiment . . . . .	74
5.1.1	Marmara Sea circulation . . . . .	74
5.2	Temporal evolution of the flow in the straits . . . . .	76
5.3	Sensitivity tests . . . . .	79
5.3.1	Impact of horizontal and vertical mesh resolution . . . . .	79
5.3.2	Impact of horizontal viscosity and diffusivity coefficients . . . . .	82
5.3.3	Persistent wind field . . . . .	84
6	THE RESPONSE OF THE TSS UNDER EXTERNAL FORCING . . . . .	87
6.1	Model assessment with focus on the Marmara Sea . . . . .	88
6.2	Model assessment with focus on Bosphorus Strait . . . . .	95
6.2.1	The role of sea level . . . . .	100
7	DISCUSSION . . . . .	103
7.1	Impacts of inputs on the TSS exchange fluxes and Marmara Sea Ecosystem . . . . .	107
8	SUMMARY AND CONCLUSION . . . . .	113
APPENDICES		
A	VERTICAL RESOLUTION . . . . .	131
B	WATER FLUX FORMULATION . . . . .	133
CURRICULUM VITAE . . . . .		139

## LIST OF TABLES

### TABLES

Table 4.1 Summary of the CTD stations selected for the lock-exchange experiment (see Figure 4.1). AS, MS and BS stand for Aegean Sea, Marmara Sea and Black Sea, respectively. . . . .	61
Table 5.1 Horizontal and vertical mesh resolution in experiments BASIC, LOW_VERT, LOW_HORIZ_1.25 and LOW_HORIZ_1.5. Abbreviations: Bosp-Bosphorus Strait, Dar-Dardanelles Strait, MS-Marmara Sea, AS-Aegean Sea and BS-Black Sea. . . . .	79
Table 5.2 Sensitivity experiments testing the impact of horizontal viscosity and diffusivity coefficients. . . . .	82
Table 6.1 Average and standard deviation of simulated and observed ( <i>Jarosz et al.</i> , 2011a) volume transports through the northern and southern cross strait sections of the Bosphorus and the Dardanelles for the period of September-December 2008. . . . .	99
Table 6.2 Correlation between simulated (experiment BBInc) and observed ( <i>Jarosz et al.</i> , 2011a) volume transports through the northern and southern cross strait sections of the Bosphorus and the Dardanelles. . . . .	99
Table 7.1 Seasonal and annual fluxes of nitrate and phosphate exchanged between the adjacent seas through the Bosphorus and Dardanelles Straits for the period of 1990-2000 (after ( <i>Polat et al.</i> , 1998; <i>Tuğrul and Beşiktepe</i> , 2007)). . . . .	109
Table A.1 Model z-layers with depths in m. . . . .	131
Table A.2 Model z-layers with depths in m. . . . .	132

## LIST OF FIGURES

### FIGURES

- Figure 1.1 Location and bathymetry of a) the Turkish Strait System, b) the Bosphorus Strait and c) the Dardanelles Strait. . . . . 7
- Figure 2.1 Moderate Resolution Imaging Spectroradiometer (MODIS) image taken on May 25, 2015 displays near peak bloom predominated by *Emiliana huxleyi*. . . . . 11
- Figure 2.2 Data sets used to generate the bathymetric chart of the TSS. . . . . 13
- Figure 2.3 TSS Black Sea exit bathymetry: Continental shelf canyon structures. 13
- Figure 2.4 Left panel: Map of the Golden Horn, the Bosphorus and adjacent area from *Marsigli* (1681). Right panel: Table showing density fluctuations of the Bosphorus waters according to the seasons, as measured from an observation point at Galata. . . . . 15
- Figure 2.5 R/V BİLİM stations surveyed in September 1994 and the salinity distribution along the Bosphorus Strait and adjacent areas based on continuous profiles (after *Gregg et al.* (1999)). . . . . 16
- Figure 2.6 Left panel: Salinity section under calm and moderate winds on 21 November 1986. Right panel: Salinity section after a period of strong southwesterly winds on 16 January 1987. Plots are from *Latif et al.* (1991). 19
- Figure 2.7 Steady-state mean fluxes ( $\text{km}^3/\text{yr}$ ) through the Turkish Straits System and between its individual compartments (after *Beşiktepe* (2003), top panel) and anomalies of the seasonal cycle of net transport through the Bosphorus Strait based on data from the 1923-1997 period (replotted from *Peneva et al.* (2001), bottom panel). . . . . 19

Figure 2.8	The volumetric flow rate in the upper layer, defined as $Q_1$ (open symbols), and in the bottom layer, defined as $Q_2$ (filled symbols), of the Bosphorus versus net flow $Q$ . Here circles and squares represent the data of Merz ( <i>Möller, 1928</i> ) and ( <i>Özsoy et al., 1986, 1988</i> ), respectively. The solid curves represent the result from a simple model ( <i>Maderich and Konstantinov, 2002</i> ) (conversion factor: $1 \text{ m}^3/\text{s} = 0.0315 \text{ km}^3/\text{yr}$ ). . . . .	20
Figure 2.9	Examples of surface salinity distributions (top panel) and horizontal circulation patterns (bottom panel) in the Sea of Marmara (from <i>Beşik-tepe et al. (1994)</i> ). . . . .	23
Figure 2.10	Transects of salinity (top panel) and temperature (bottom panel) across the TSS, along the main axis extending from the Aegean Sea to the Black Sea through the Dardanelles Strait (0-120 km), Marmara Sea (120-300 km) and Bosphorus Strait (300-340 km). The data was collected on board of R/V Bilim-2 during a field survey in May 2007. . . . .	24
Figure 2.11	Upper layer average salinity variations along the main axis of the Turkish Straits System in different months sampled by cruise data (taken from <i>Ünlüata et al., 1990</i> ). . . . .	24
Figure 2.12	Marmara Sea salinity variations in April 1995: at 5 m depth (top panel), and west to east along the main axis (bottom panel). . . . .	25
Figure 2.13	Salinity distribution and the line of zero velocity (black line) in the Bosphorus obtained from a three dimensional hydrodynamic model (ROMS) of the Bosphorus exchange flow ( <i>Sözer, 2013</i> ). The boundary conditions are defined by adjacent basin properties after <i>Gregg and Özsoy (2002)</i> with an imposed barotropic flux of $5600 \text{ m}^3/\text{s}$ , GLS turbulence parameterization and a minimum horizontal resolution of 50 m. . . . .	28
Figure 4.1	Top: Horizontal resolution of the surface mesh (in km). Bottom: Vertical resolution and depth relation of the FEOM mesh. The horizontal axis depicts the vertical layer thickness and the vertical axis shows the depth in m in logarithmic scale. . . . .	58
Figure 4.2	Vertical profiles of potential temperature (left), salinity (middle) and potential density (right) representative for the Aegean Sea (red), Black Sea (blue) and Marmara Sea (green) used for lock exchange initial conditions. . . . .	61
Figure 4.3	Assignment of the profiles depicted in Figure 4.2 to the respective basins, i.e. the Aegean Sea (red), Black Sea (blue) and Marmara Sea (green). . . . .	62

Figure 4.4	Time series of the wind stress (top panel) and wind stress curl (bottom panel) averaged over the TSS region. . . . .	63
Figure 4.5	Spatial distribution of the wind stress of the ECMWF atmospheric data averaged over April 2008 (left) and over October 2008 (right) in the TSS domain. Wind stress is split into its zonal and meridional components. . . . .	64
Figure 4.6	Time series of the net surface heat flux and its components computed according to the formulation by <i>Pettenuzzo et al.</i> (2010) averaged over the Marmara Sea. $Q_{net}$ , $Q_s$ , $Q_b$ , $Q_e$ and $Q_h$ represent net heat flux (black), shortwave (red), longwave (blue), latent heat (brown) and sensible heat (green) fluxes, respectively. . . . .	68
Figure 4.7	ECMWF 2 m air temperature field over the Mediterranean Sea before the creeping algorithm (top left), after the first iteration (top right), after 30 iterations (bottom left) and the difference prior and post creeping algorithm (bottom right). . . . .	69
Figure 4.8	Eight matrices created using the land-sea masked 2 m air temperature field. . . . .	70
Figure 4.9	Difference in 2 m air temperature before and after the 30th sea over land iteration. . . . .	70
Figure 4.10	Monthly mean climatological freshwater input ( $-E + P + R$ ) of the Black Sea from <i>Kara et al.</i> (2008) used in experiment BBInc. . . . .	71
Figure 5.1	Surface, 10 m, 20 m, 50 m level circulation in m/s in the Marmara Sea averaged over the last month of simulation BASIC (from top to bottom). Note that different color scales are used for different depths. . . . .	75
Figure 5.2	Snapshots of potential density along the Thalweg of the Bosphorus (from south to north, left panel) and Dardanelles (from south to north, right panel) at the initial state and after 1, 3, 5 and 7 days (from top to bottom). The x-axis denotes the distance in km. . . . .	77
Figure 5.3	Time series of total kinetic energy averaged over the Marmara Sea (top panel) and upper layer (red), lower layer (blue) and net (green) volume transport through section B1 (see Figure 1.1 for the location of the section, bottom panel). . . . .	78
Figure 5.4	Horizontal velocity (in m/s) along the thalweg of the Bosphorus (from south to north) averaged over the last month of simulation BASIC. Contour lines are plotted at an interval of 1 m/s. Circles denote the points where flow has shear instabilities defined by the Richardson number less than 0.25. . . . .	78

Figure 5.5 Simulated density along the Thalweg of the Bosphorus (left) and surface circulation in m/s (right) in the Marmara Sea averaged over the last month of the simulation for experiments BASIC, LOW_VERT, LOW_HORIZ_1.25 and LOW_HORIZ_1.5 (top to bottom). . . . .	80
Figure 5.6 Simulated isopycnals (13.6, 14, 16, 22, 26 and 28 kg/m <sup>3</sup> ) along the Thalweg of the Bosphorus for BASIC (black line) and sensitivity experiments (a) LOW_VISC, (b) HIGH_DIFF and (c) LOW_DIFF (red lines) averaged over the last month of simulation. . . . .	83
Figure 5.7 Simulated surface circulation in m/s (upper panel) and salinity in psu (lower panel) in the Marmara Sea averaged over April 2008 for experiment WIND_SW(left panel) and experiment WIND_NE (right panel) . . .	85
Figure 5.8 Density field (kg/m <sup>3</sup> ) along the Bosphorus Strait averaged over the last month of the simulation for experiments BASIC (top), WIND_SW (middle) and WIND_NE (bottom). . . . .	86
Figure 6.1 Simulated surface circulation in m/s (upper panel) and salinity in psu (lower panel) in the Marmara Sea averaged over April 2008 for experiment BBExc (left panel) and experiment BBInc (right panel). . . . .	89
Figure 6.2 The same as Figure 6.1, but for October 2008. . . . .	89
Figure 6.3 Positions of CTD stations collected during the SESAME cruise in April 2008 (top left). Potential temperature (top right), salinity (bottom left) and potential density (bottom right) measured at the corresponding stations. . . . .	90
Figure 6.4 Same as Figure 6.3, but for October 2008. . . . .	90
Figure 6.5 T-S diagram of profiles in the Marmara Sea for the time periods of April (red) and October 2008 (blue) from SESAME observations and FEOM hindcast simulations BBExc (left) and BBInc (right). Measurements and values from the model simulations are denoted by circles and crosses, respectively. . . . .	91
Figure 6.6 Vertical profiles of temperature and salinity in the surface layers of the Marmara Sea averaged over all stations. Model results are interpolated onto the position of the CTD stations for simulations BBExc (blue) and BBInc (red). Black lines represent the observations. Solid and dashed lines indicate profiles for April and October 2008, respectively. . . . .	93

Figure 6.7	Accumulated root-mean-square errors between simulated and observed temperature (upper panel) and salinity profiles (lower panel) in the Marmara Sea for April 2008. The left panel shows root-mean-square errors for experiment BBExc, the right panel for experiment BBInc. . . . .	94
Figure 6.8	The same as Figure 6.7, but for October 2008. . . . .	94
Figure 6.9	Simulated depth of the sigma-25 layer averaged over the Marmara Sea for the experiments BBExc (blue) and BBInc (red). . . . .	95
Figure 6.10	Time series of the simulated along-strait velocity profiles (m/s) in the middle of the Section B1 (top) and close to the Asian coast on Section B1 (middle) and cross-strait velocity profiles in the middle of the Section B1 (bottom) for the year 2008. . . . .	96
Figure 6.11	Observed along-strait velocity profiles (top and middle) and across-strait velocity profiles (bottom) in the same locations as described in Figure 6.10 for September to December 2008, taken from <i>Jarosz et al.</i> (2011a). . . . .	97
Figure 6.12	Thalweg section of potential density along the Bosphorus from observations in September 1994 (top panel) and from simulation BBInc in September 2008 (bottom panel). . . . .	98
Figure 6.13	Timeseries of detrended simulated (solid line) and observed (dotted line) volume transport through the section B4 (Northern Bosphorus). Observations are from <i>Jarosz et al.</i> (2011a) . . . . .	99
Figure 6.14	Simulated surface currents on November 21, 2008 in the Bosphorus (top left) and on November 20, 2008 in the Dardanelles (bottom left) and surface currents averaged over November 2008 (right). . . . .	101
Figure 6.15	Net simulated transport through the Section A (blue) and sea surface height difference (green) between the Black and Aegean Seas and its steric (red) and bottom pressure components (cyan). . . . .	102
Figure 7.1	SAR (synthetic aperture radar) satellite image showing fine flow features near the Marmara exit of the Bosphorus Strait on May 29, 1995. . . . .	104
Figure 7.2	Landsat 8 satellite image showing the blooms in the Marmara Sea on May 17, 2015. . . . .	105
Figure 7.3	The Moderate Resolution Imaging Spectroradiometer (MODIS) on NASA's Terra satellite captured bloom events in the Sea of Marmara on May 23 (left) and May 25 (right), showing a coccolithophore bloom developed in the Turkish Straits System. . . . .	105



Figure 7.4 Aqua-MODIS recorded features in the Sea of Marmara on April 27, 2013 shows possible Trichodesmium blooms in the Turkish Straits System. . . . . 106

Figure 7.5 Red patches appeared on coastal band of Tekirdag in the Marmara Sea, which might be as a result of an increase in the population of probably dinoflagellates. courtesy: DHA; 2013, April 26. . . . . 110



## LIST OF ABBREVIATIONS

$a$	radius of earth
$A_h$	lateral momentum diffusion coefficient
$A_o$	water vapor and ozone absorption
$A_v$	vertical momentum diffusion coefficient
$A_{v0}$	background vertical momentum diffusion coefficient
<i>ADCP</i>	Acoustic Doppler Current Profiler
<i>AS</i>	Aegean Sea
<i>Bosp</i>	Bosphorus
<i>BS</i>	Black Sea
$C$	tracer
<i>CIL</i>	cold intermediate layer
$C_d$	bottom drag coefficient
$C_e$	atmosphere-ocean transfer coefficient for the exchange of sensible heat
$C_h$	atmosphere-ocean transfer coefficients for the exchange of latent heat
$C_p$	specific heat capacity of water
<i>CTD</i>	conductivity temperature depth
<i>Dar</i>	Dardanelles
$E$	evaporation
<i>EMT</i>	East Mediterranean Transient
<i>FEOM</i>	Finite Element Ocean Model
<i>FESOM</i>	Finite Element Sea-Ice Ocean Model
$F^{salt}$	virtual salt flux into the ocean
$F_{P-E}^{salt}$	virtual salt flux into the ocean due to precipitation minus evaporation
$F_{ice}^{salt}$	virtual salt flux into the ocean due to ice melting
$F_{runoff}^{salt}$	virtual salt flux into the ocean due to river runoff
$f$	Coriolis parameter

$g$	gravitational acceleration
$H(x, y)$	ocean bottom depth
$h$	the sun's hour angle
$J_o$	solar constant
$K_h$	lateral diffusivity
$K_v$	vertical diffusivity
$K_{v0}$	background vertical diffusivity
$L_e$	latent heat of vaporization or sublimation
$\mathbf{k}$	vertical unit vector
<i>MOMA</i>	Meteoroloji / Oşinografi Mükemmeliyet Ağı Projesi
<i>MS</i>	Marmara Sea
$N$	buoyancy frequency
$\mathbf{n}$	2D unit normal vector
$\mathbf{n}_3$	3D unit normal vector
<i>OGCM</i>	Ocean General Circulation Model
$p$	hydrostatic pressure
$P$	precipitation
$Q_{diff}$	diffused sky radiation
$Q_{dir}$	attenuated direct solar radiation on the ocean surface
$Q_l$	net long wave radiative flux
$Q_{lat}$	turbulent flux of latent heat
$Q_{ld}$	long wave downward radiative flux
$Q_s$	short wave radiative flux
$Q_c$	conductive heat flux
$Q_o$	radiation at the top of the atmosphere
$Q_{sens}$	turbulent flux of sensible heat
$Q_{tot}$	total radiation from the top of the atmosphere
$q$	surface flux
$q_a$	specific humidity of air
$q_s$	artificial saturated specific humidity for sea surface temperature
$R$	river runoff
$R_i$	Richardson number
<i>ROMS</i>	Regional Ocean Modeling System

$S$	salinity
$S_s$	salinity of the oceanic surface layer
$S_{ref}$	reference salinity
$S_{sn}$	sources and sinks in the snow thickness continuity equation
<i>SESAME</i>	Southern European Seas: Assessing and Modeling Ecosystem changes
<i>SSH</i>	sea surface height
<i>SST</i>	sea surface temperature
$T$	potential temperature
$T_a$	air temperature at 10 m
$T_f$	freezing point of sea water
$T_s$	potential temperature of the oceanic or ice surface layer
$t$	time or julian day
<i>TSS</i>	Turkish Straits System
$z$	zenith angle
$\mathbf{u}$	horizontal ocean velocity
$\mathbf{u}_s$	horizontal ocean velocity of the surface layer
$\mathbf{u}_{10}$	horizontal wind field at 10 m height
$\mathbf{u}_{ice}$	sea ice velocity
$\mathbf{u}^*$	auxiliary horizontal velocity
$\mathbf{v}$	3D ocean velocity
$w$	vertical velocity
$\alpha$	space dependent albedo
$\beta$	noon solar altitude in degrees
$\epsilon$	emissivity
$\delta$	sun declination angle
$\dot{\epsilon}$	tensor of deformation rates
$\eta$	sea surface height
$\lambda$	longitude
$\Phi$	vertical velocity potential
$\rho$	mean density of sea water
$\rho_0$	deviation from the mean density of sea water
$\rho_a$	air density
$\sigma$	stress tensor

$\theta$	latitude
$\tau$	atmospheric transmission coefficient
$\tau_o$	ocean surface stress
$\Omega$	model domain
$\Gamma_1, \Gamma_2, \Gamma_3$	boundaries of the domain $\Omega$
$\nabla$	2D gradient and divergence operator
$\nabla_3$	3D gradient and divergence operator
$\Delta$	square root of the surface triangle area





# CHAPTER 1

## INTRODUCTION

The aim of this study is to simulate the ocean circulation, hydrography and volume fluxes in the Turkish Straits System (TSS) realistically and to understand the impact of the Black Sea freshwater budget on the TSS. For this task, the Finite Element Ocean Model (FEOM), an ocean general circulation model operating on unstructured meshes, is adopted for the TSS. The TSS links the Black Sea to the Aegean Sea (namely, the Mediterranean Sea) via the Marmara Sea, the Bosphorus and the Dardanelles Straits (Figure 1.1).

The ocean circulation in the TSS is characterized by a two-layer flow. The upper layer flow leaves the Black Sea with an annual mean surface salinity of about  $\sim 18$ , while the lower layer flow originating from the Mediterranean Sea has typical salinity values of  $\sim 39$ . Salt conservation for the Black Sea therefore implies a ratio of about 2:1 between the net outflux and the influx at the Bosphorus (*Ünlüata et al.*, 1990). The annual fresh water flux into the Black Sea by rivers and rainfall is greater than the loss by evaporation. The remaining amount is balanced by the net flux through the TSS. *Ünlüata et al.* (1990) estimated precipitation (P), river runoff (R) and evaporation (E) for the Black Sea and quantified as  $300 \text{ km}^3/\text{yr}$ ,  $352 \text{ km}^3/\text{yr}$  and  $353 \text{ km}^3/\text{yr}$ , respectively, resulting in a net flux (P+R-E) of  $300 \text{ km}^3/\text{yr}$ .

The currents and the circulation developed both within the TSS and in the exit regions are characterized by an exchange flow regime primarily driven by density, sea level and barometric pressure differences across the system (*Marsigli*, 1681; *Defant*, 1961; *Özsoy et al.*, 1986; *Oğuz*, 2005; *Sözer*, 2013). Various key processes determine the flow characteristics in the TSS. First, the geometry plays an important role in direct-

ing and locally intensifying the flow. Hydraulic controls at natural barriers in the two straits as well as their exit channels appear to regulate the flow. The presence of a sill (depth: 60 m) and a contraction (width: 700 m, depth: 110 m) located in the Bosphorus serve to establish a unique case of the 'maximal exchange' regime as described by *Farmer and Armi (1986); Armi and Farmer (1987)*. The 'maximal exchange' regime was confirmed by experimental measurements (*Özsoy et al., 2001*) and demonstrated later through 3D modeling (*Sözer, 2013*). The Dardanelles, however, possess a sub-maximal exchange regime due to a single control at the Nara Passage (*Oğuz and Sur, 1989*). At the exits of both control sections, the flow intensifies either near the surface or near the bottom, eventually leading to dissipation in the form of hydraulic jumps. Second, observed volume fluxes (*Ünlüata et al., 1990*), hydrographic observations (*Gregg et al., 1999; Gregg and Özsoy, 1999, 2002*) and model results (*Sözer, 2013*) reveal the important role of turbulent mixing and entrainment on the evolution of waters in transit through the TSS. Third, the combined effect of winds and barometric pressure variations superposed on the net flow through the TSS influences the internal structure of currents and the position of the interface, often leading to short-term changes and intermittent blocking of either the upper or the lower layers of the Bosphorus. Strong southerly winds create blocking of the upper layer flow, while northerly winds create the same for the lower layer flow (*Latif et al., 1991*).

Surface buoyant jets and bottom dense water plumes at the junctions of the straits contribute to mixing (*Beşiktepe et al., 1994; Özsoy et al., 2001*). For instance the jet entering the Marmara Sea from the Bosphorus greatly influences and in the absence of wind forcing largely determines the circulation in the Marmara Sea, as shown by drifter observations of *Gerin et al. (2013)*. A basin-wide anticyclonic eddy embedded in an S-shaped meander current extending from the Bosphorus to the Dardanelles seems to be a basic pattern. The lower layer flow of Mediterranean water entering through the Dardanelles Strait moves in the opposite direction and finally flows out from the Bosphorus in the form of a bottom plume spreading on the Black Sea shelf (e.g. *Latif et al., 1991; Özsoy et al., 2001; Beşiktepe, 2003*).

Numerical simulations reveal physical insight into the circulation and transport through the TSS. However, numerical modeling of the TSS and its role in coupling the adjacent seas is a grand challenge. First of all, resolving the complex topography is re-



quired. In particular, the Marmara Sea dynamics is largely influenced by the Bosphorus and Dardanelles Strait inflow/outflow where cross-sections are less than 1 km wide (the minimum width of the Bosphorus is  $\sim 700$  m). Secondly, when modeling the fjord-like two-layer flow in the Turkish Straits one should consider very special turbulent mixing regimes (*Gregg and Özsoy, 2002; Jarosz et al., 2011a, 2012*), with rapid response of the shallow upper layer to driving forces, high shear and inhomogeneities. *Oğuz and Sur (1989)* showed with a two-layer model that upper layer flow is controlled hydraulically at Nara Passage and the Dardanelles-Aegean Sea Junction. *Kanarska and Maderich (2008)* highlighted the effect of turbulent friction and entrainment on the flow dynamics using a model based on three-layer hydraulic theory and identified the control section to be the Nara Passage. *Demyshev and Dovgaya (2007)* developed a 3D ocean model for the Marmara Sea. They showed that the main basin-wide anticyclonic surface circulation is dependent on the Bosphorus intrusion into the Marmara Sea. Their simulation did not include any surface heat and water fluxes. An application of the Regional Ocean Modeling System (ROMS) to the Marmara Sea was used to investigate the sensitivity of stratification and surface circulation to atmospheric forcing and Bosphorus inflow (*Chiggiato et al., 2012*). A two-layer hydraulic model (*Oğuz et al., 1990; Oğuz, 2005*) revealed the control mechanism on upper and lower layer flows considering the critical composite Froude Number at the northern and southern sills and at the contraction zones. However, a shortcoming of all these studies is that they are restricted to parts of the TSS. So far, a numerical model covering the entire system of basins with sufficient resolution to reproduce the physics with realistic seasonal variability is missing.

The TSS is an important navigation and energy route as it connects diverse marine basins (*Akten, 2004*). Moreover, it plays a key role in the dynamics of the sensitive ecosystems of the adjacent basins. The thin layer of dense bottom water exiting the northern Bosphorus is the only salinity source of the Black Sea. This layer determines the salt budget in the Black Sea as well as carries dissolved inorganic nitrate and phosphate affecting its ecological system (*Tuğrul et al., 2002*). In the Mediterranean, the relatively fresh Dardanelles outflow alters the North Aegean surface water masses and currents (*Kourafalou and Tsiaras, 2007*). Anomalously low Dardanelles outflow when combined with cold atmospheric weather fronts may lead to dense wa-

ter formation and triggers the East Mediterranean Transient (EMT) event (*Zervakis et al.*, 2000, 2004).

In this study the ocean general circulation model FEOM is applied since it is particularly suitable to model the TSS. The choice of the discretization of the governing equations, the finite element method, allows us to employ unstructured surface meshes. This allows for local horizontal mesh refinement in areas of particular dynamic or scientific interest. The model has been successfully applied to study the flow through the narrow straits of the Canadian Arctic Archipelago (*Wekerle et al.*, 2013).

The model realistically represents the geometry of the TSS, but uses idealized initial conditions. As initial condition, three different salinity and temperature profiles are prescribed for Aegean, Marmara and Black Seas, letting the flow through the straits adjust freely to the density gradient. This lock-exchange experiment allows us to develop a basic understanding of the multi-scale dynamical behavior of the TSS to forcing functions, especially monthly changes in the Black Sea freshwater budget. Besides, it provides a more realistic estimate of transport through the TSS which plays an important role in the hydrological cycle at regional scale.

This study aims first to create a state-of-the-art ocean model that allows for a faithful representation of the dynamical and mixing roles of the Bosphorus Strait together with the interconnected basins of the Marmara and the Black Seas, thus providing a coherent methodology to analyze coupling between these seas. Second, it quantifies two important driving mechanisms of the system: the atmospheric forcing and the Black Sea freshwater budget. That is one of the unique scientific contributions this study is bringing. Moreover, the model system is foreseen to become a forecasting tool in a strategically important, active industrial-economic zone of Turkey, leading to analyses of the effects of atmosphere-ocean interaction and of possible coupled ecosystem development in future.

The specific scientific objectives of this study are:

- to improve the scientific understanding of the TSS by constructing a well resolved, high level, physically representative predictive model of its hydrodynamics, utilizing the finite element / unstructured grid approach and High Per-

formance Computation (HPC) opportunities

- to answer the presently unresolved problem of the Mediterranean – Black Seas coupling, through improved representation of the TSS response in an extremely complicated environmental setting
- to establish improved estimates of transport through the TSS and to contribute information on the hydrological cycle at regional scale
- to provide a better understanding of the Marmara Sea circulation / mixing processes and to show their contributions to hydrology and ecosystems of the adjacent seas
- to provide a basic understanding of the multi-scale dynamical responses of the TSS to the forcing agents
- to evaluate the performance and capabilities of the employed modern ocean model in the rather extreme environment of the TSS (e.g. blocking events)
- to develop forecasting capabilities for the TSS region, and to provide data for possible parameterizations, thus interconnecting and improving the quality of existing forecasts in the adjoining areas of the Mediterranean and Black Seas.

The processes that determine the fate of the transition at the TSS are highly nonlinear and non-uniform in their nature. Sharp topographical gradients of the straits, contrasts between the continental shelf and deep topographies of the Marmara and Black Seas, combined with the sharp density stratification are some of the most extreme situations. The shear and small scale turbulence of the exchange flow at the straits requires the model to be eddy resolving at relevant scales, while the expected jet flows require a good level of horizontal resolution and/or parameterization. The surface and dense water overflows from straits into adjacent domains are in the form of jets and plumes, again with strong currents and re-circulations, driving convective activity. All these features put capabilities of modern ocean models to test, requiring the non-hydrostatic and nonlinear dynamics to be represented at adequate resolution. A series of earlier attempts aimed to develop separate predictive models of the individual straits and the Marmara Sea basin. Computationally, the ability to represent the entire TSS at

full resolution requires finite element / unstructured grid approach and powerful High Performance Computation methodology.

This study is organized as follows. In chapter 2, a general description of the TSS bathymetry, hydrography and circulation based on measurements is presented. In chapter 3, the model equations, discretization and setup is described. Chapter 4 is devoted to sensitivity experiments investigating the impact of mesh resolution, horizontal viscosity and diffusivity coefficients and persistent wind direction. In chapter 5, dynamical changes of the TSS are discussed from the Black Sea freshwater budget point of view. This thesis closes with a discussion and conclusions.



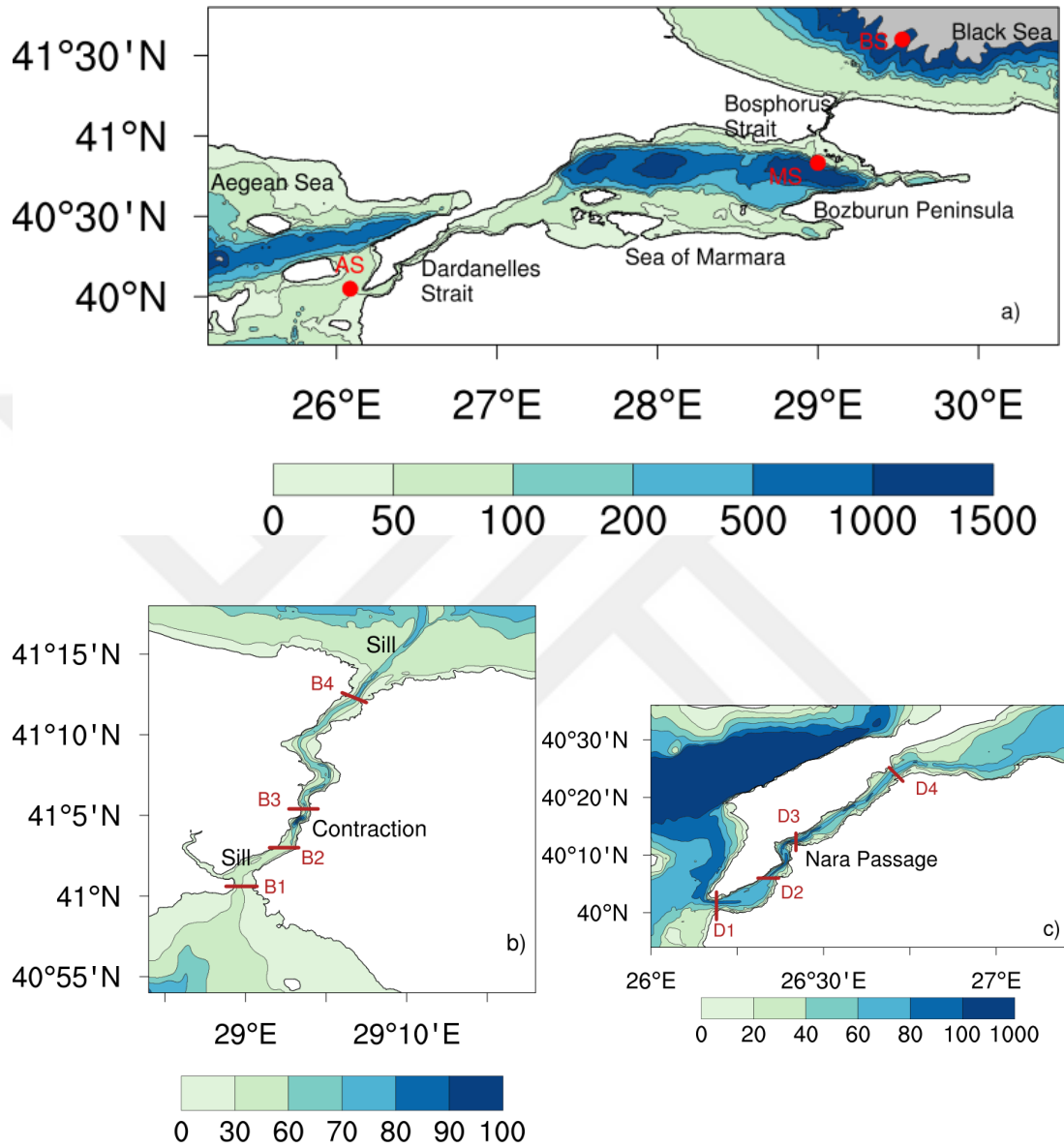


Figure 1.1: Location and bathymetry of a) the Turkish Strait System, b) the Bosphorus Strait and c) the Dardanelles Strait.



## CHAPTER 2

### GENERAL CHARACTERISTICS

In this chapter, the present general characteristics of the TSS will be presented. First, the bathymetry of the TSS will be described. Second, a review of the oceanographic measurements conducted and the circulation in this region will be presented. Third, the outcomes of previous modeling studies will be mentioned in detail. In the last part, a new bathymetry merged for this model application will be explained.

#### 2.1 Geometric Features

The Turkish Strait System (TSS) is a water passage connecting the Black Sea to the Aegean Sea (namely, the Mediterranean Sea) through the Bosphorus and Dardanelles Straits, with the Sea of Marmara in between Figure 2.1. The Bosphorus Strait is the most significant part of the TSS as it controls mainly the water exchange between the Black Sea and the Marmara Sea, by extension via the Dardanelles, the Aegean and Mediterranean Seas (Özsoy *et al.*, 1986; Ünlüata *et al.*, 1990).

The Bosphorus is a narrow, elongated strait with sharp turns and variable width and depth in its course (Figure 1.1b). It has a total length of  $\sim 35$  km and the width of the channel varies between 0.65 km and 3.5 km at the surface with an average value of 1.3 km. The width reduces toward the bottom to an average value of 500 m at 50 m depth. The depth varies considerably along the Bosphorus. The northern half of the Bosphorus possesses large shallow areas in the vicinity of the coastlines (depth  $\leq 10$  m) compared to the southern section. The depth varies between 28 m and 105 m and the average depth of the entire strait is 38 m (Sözer, 2013). The deepest part of the

strait coincides with the narrowest section at the '*contraction*' and is situated around  $41^{\circ} 5' N$ , approximately 12 km from the Bosphorus-Marmara Sea junction.

Prominent geometric features of the Bosphorus besides the contraction are the two sills: one located between the contraction and the southern exit and another one situated slightly north of the Black Sea exit. The southern sill is located 3.5 km north of the southernmost reach of Bosphorus (Figure 1.1b). Its central ridge rises to about 28 m and is flanked by two 40 m deep channels on both sides (Sözer, 2013). The northern sill is located just about 2 km north of the Bosphorus - Black Sea junction, inside a narrow canyon, with a crest of 63 m that first extends in the northeast direction from the strait axis and then bends towards the northwest direction. This geometric feature is significant in controlling the dense water plume that migrates from the Bosphorus onto the the Black Sea shelf and sinks along continental slope into the deep layers of the Black Sea. The northern sill and the contraction serve as the topographic features responsible for the hydraulic controls in which the Bosphorus is ideally defined as in a '*maximal-exchange*' regime.

The orientation of the Bosphorus increases the complexity of the flow leading to flow separation and eddy circulation in bays. The Bosphorus turns sharply about its average orientation. Starting from south to north, it first turns over the south sill by  $90^{\circ}$  clockwise. Along the contraction it bends  $60^{\circ}$  counterclockwise and then bends back by nearly the same amount immediately to the north. It twists  $128^{\circ}$  counterclockwise over a few kilometers along the northern part, and then remains fairly straight north of position 22 km (Sözer, 2013).

The Dardanelles Strait is a 62 km long and 1.2 to 7 km wide narrow strait connecting the Aegean Sea with the Sea of Marmara (Figure 1.1c). It lies between the peninsula of Gallipoli in Europe (northwest) and the mainland of Asia Minor (southeast). The average depth of the strait is 55 m and the maximum depth is more than 100 m in the narrowest central section. The most conspicuous feature in Dardanelles is the sharp turn in channel direction located at the Nara Passage. The strait channel extends in a funnel shape across the Marmara shelf towards the deep basin through a canyon. Across the strait the topography generally takes the valley form except the wider region where it is gentle. The shallow regions (depth  $\leq 10$  m) are larger on the Asian



side compared to the European coast.

The Marmara Sea is a small inland sea located between 40°-41.5° N and 27°-30° E. It extends ~240 km in east-west direction and ~70 km in north-south direction. It has a surface area of ~11500 km<sup>2</sup> a volume of 3380 km<sup>3</sup>. The shore line including the Bosphorus and the Dardanelles is 1189 km in long. The length of the Asian and the European shore lines are 663 km and 264 km, respectively (*Beşiktepe et al.*, 1994). A wide continental shelf (depth less than ~100 m) occupies the southern part of the basin, while a narrow continental shelf 2-13 km in width runs along the northern coast. Three sub-basins (of maximum depths 1097 m, 1389 m and 1238 m), separated by two sills (depth ~700 m), are aligned from west to east. The straits are connected to the adjacent basins through canyons. A submarine canyon of 75 m depth leads from the Dardanelles Strait, connecting to the western depression of the Marmara Sea (*Ergin et al.*, 1993; *Beşiktepe et al.*, 1994). The eastern depression is connected to the southern exit of the Bosphorus with a 70 m-deep canyon.

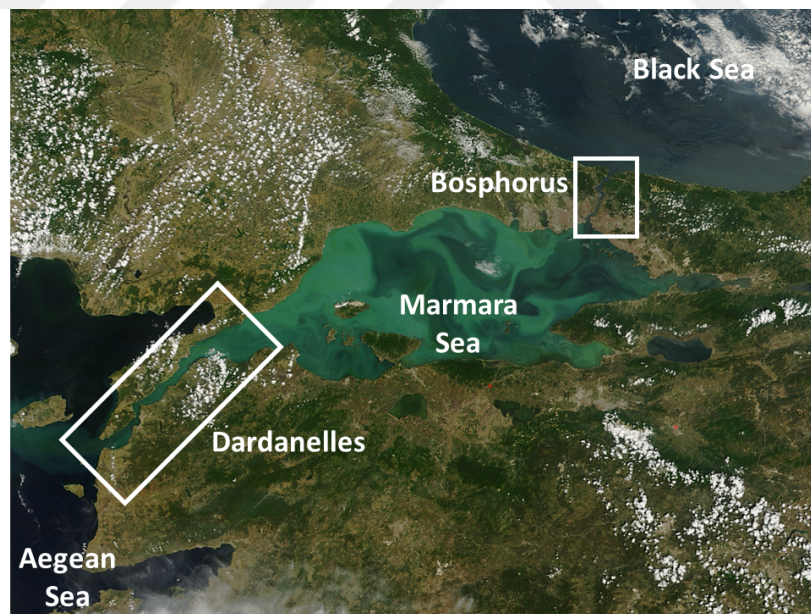


Figure 2.1: Moderate Resolution Imaging Spectroradiometer (MODIS) image taken on May 25, 2015 displays near peak bloom predominated by *Emiliana huxleyi*.

## 2.2 Assembling the fine resolution bathymetry of the Turkish Straits System

Through various physical/biochemical processes taking place within its domain, the TSS determines the exchange between the Black Sea and the Mediterranean Sea. The experimental studies and the accurate representation of these processes in models of the exchange critically depends on exact knowledge of the detailed bathymetry of the system. The region is characterized by widest continental shelves of Turkish Seas neighboring deep basins, various shallow and deep sills, canyons and channels with large topographic variations. Standard datasets, such as the General Bathymetric Chart of the Oceans (GEBCO) proved to be unsuitable for the area of interest, in particular the Bosphorus and Dardanelles are not sufficiently resolved. Responding to the need to resolve great variations, bathymetric data from various sources and with different characteristics have been merged, harmonized and obtained primarily for use in modeling and experimental studies. Therefore, a higher resolution bathymetric data set was generated by carefully matching and combining bathymetric data from different sources. A high-resolution (20 m gridded) bathymetric dataset at the Straits has been kindly made available by the colleague Erkan Gökaşan (*Gökaşan et al.*, 2005, 2007) with the permission of the Turkish Navy, Navigation, Hydrography and Oceanography Office. Other data sources for the Black Sea shelf area, including multi-beam surveys obtained by the R/V ALLIANCE and ADCP soundings by R/V BILIM (*Özsoy et al.*, 2001) have been used to correct biases and to have enhanced representation of bottom features in this area. The coverage of all these datasets is shown in Figure 2.2. The bathymetry for the remaining part of the model domain is based on the GEBCO gridded data with a resolution of 30 arc-seconds.

Using the Generic Mapping Tools (GMT) (*Wessel et al.*, 2013), randomly spaced data points were bi-linearly interpolated onto a 50 m resolution evenly spaced regular grid. Arbitrarily located data points are brought into a mean position, thereafter a surface is fitted to the evenly spaced data points with a tension factor of 0.25. Each data set is assigned to a weighing factor based on its reliability for an overview of all datasets). The resulting TSS Black Sea Junction bathymetry with its continental shelf canyon details is depicted in Figure 2.3.

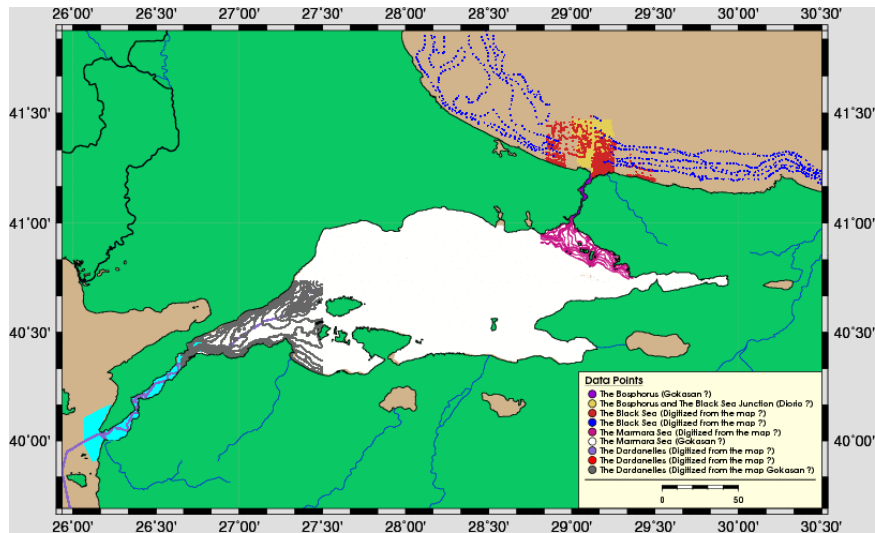


Figure 2.2: Data sets used to generate the bathymetric chart of the TSS.

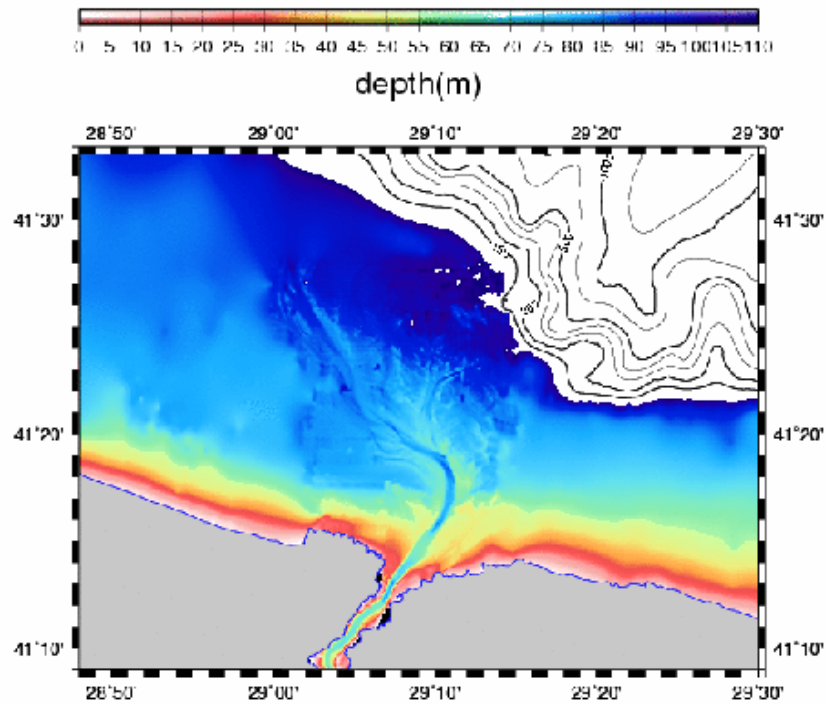


Figure 2.3: TSS Black Sea exit bathymetry: Continental shelf canyon structures.

### 2.3 Hydrographic Characteristics

The Bosphorus and Dardanelles Straits and the Marmara Sea are characterized by a two-layer exchange flow with a strong pycnocline maintained by density and sea level gradients between the Black Sea and the Aegean Sea. In the upper layer, Black

Sea waters flow towards the Mediterranean and in the lower layer, Mediterranean waters flow towards the Black Sea. The key driving mechanisms leading the two-layer exchange flow are the horizontal density gradient between the Mediterranean and the Black Sea and the positive freshwater balance in the Black Sea resulting in higher sea-level. The excess water produces a net barotropic flow towards the Mediterranean Sea under normal wind conditions.

The hydrographic characteristics of the water masses in the TSS have been reported in several publications (e.g. *Möller (1928)*; *Oğuz et al. (1990)*; *Ünlüata et al. (1990)*).

### **The Bosphorus**

The earliest observations and experiments on density driven exchange flows have been performed by *Marsigli (1681)* in the 17<sup>th</sup> century. He observed the density difference between the surface layers and the bottom waters and concluded that near surface currents are originated from the lighter Black Sea whereas in deeper parts should be from the Sea of Marmara (Figure 2.4). He also concluded that heavier water flowed from the Sea of Marmara into the Bosphorus because of its weight. He supported his findings through a laboratory experiment. In his experimental setup, he used a tank split into two parts by a wall with two holes at the surface and at the bottom. One part was filled with light water and the other with heavy dense water. He demonstrated that water bodies with different densities would build up the exchange flow between the two parts (*Defant, 1961*).

Following *Marsigli (1681)*, the systematic survey of the TSS is initiated to obtain basic understanding in early 20<sup>th</sup> century by English, Russian, Danish and German observers (*Wharton, 1872*; *Makarov, 1885*; *Nielsen, 1912*; *Möller, 1928*). There has been a large discussion among oceanographers on the blockage of the Bosphorus flow. *Tuğrul et al. (1946)* studied the hydrography of the Bosphorus strait. His hypothesis based on the assumption that the Mediterranean originated heavy water is mixed into the upper layer water from the Black Sea continuously on its course and is returned back to the Marmara Sea again. He also performed laboratory experiments to understand the vertical distribution of tracers in the Bosphorus Strait. Missing bathymetric information from the Black Sea-Bosphorus Junction and incorrect esti-

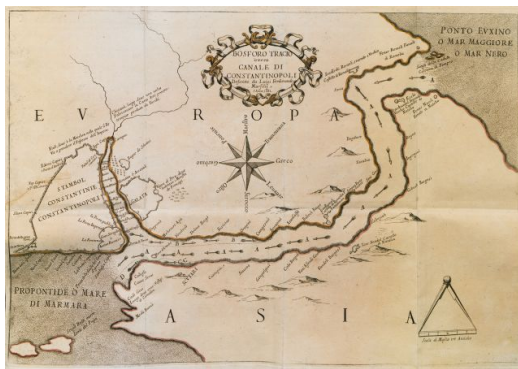


TAVOLA DELLE OSSERVAZIONI FATTE NEL CANALE DI COSTANTINOPOLI DALLA PARTE DI GALATA, IN FACCIATA alla punta del Serraglio, per conoscere il Flutto, e Sifflato che sui si trova. Il Palmi Romano è la misura da noi per maggior chiarezza usata. In Firenze, e Parisi. Il Livello dell'acqua del Palazzo d'Orsi è quello di più, e di meno. Sarà la correzione di differenza. Pag. 117.

Giorno.	Levan del Sole.	Merzognono.	Tramonto del Sole.	None.	Vento.
1681-01-01	0	0	0	0	0
1681-01-02	0	0	0	0	0
1681-01-03	0	0	0	0	0
1681-01-04	0	0	0	0	0
1681-01-05	0	0	0	0	0
1681-01-06	0	0	0	0	0
1681-01-07	0	0	0	0	0
1681-01-08	0	0	0	0	0
1681-01-09	0	0	0	0	0
1681-01-10	0	0	0	0	0
1681-01-11	0	0	0	0	0
1681-01-12	0	0	0	0	0
1681-01-13	0	0	0	0	0
1681-01-14	0	0	0	0	0
1681-01-15	0	0	0	0	0
1681-01-16	0	0	0	0	0
1681-01-17	0	0	0	0	0
1681-01-18	0	0	0	0	0
1681-01-19	0	0	0	0	0
1681-01-20	0	0	0	0	0
1681-01-21	0	0	0	0	0
1681-01-22	0	0	0	0	0
1681-01-23	0	0	0	0	0
1681-01-24	0	0	0	0	0
1681-01-25	0	0	0	0	0
1681-01-26	0	0	0	0	0
1681-01-27	0	0	0	0	0
1681-01-28	0	0	0	0	0
1681-01-29	0	0	0	0	0
1681-01-30	0	0	0	0	0
1681-01-31	0	0	0	0	0
1681-02-01	0	0	0	0	0
1681-02-02	0	0	0	0	0
1681-02-03	0	0	0	0	0
1681-02-04	0	0	0	0	0
1681-02-05	0	0	0	0	0
1681-02-06	0	0	0	0	0
1681-02-07	0	0	0	0	0
1681-02-08	0	0	0	0	0
1681-02-09	0	0	0	0	0
1681-02-10	0	0	0	0	0
1681-02-11	0	0	0	0	0
1681-02-12	0	0	0	0	0
1681-02-13	0	0	0	0	0
1681-02-14	0	0	0	0	0
1681-02-15	0	0	0	0	0
1681-02-16	0	0	0	0	0
1681-02-17	0	0	0	0	0
1681-02-18	0	0	0	0	0
1681-02-19	0	0	0	0	0
1681-02-20	0	0	0	0	0
1681-02-21	0	0	0	0	0
1681-02-22	0	0	0	0	0
1681-02-23	0	0	0	0	0
1681-02-24	0	0	0	0	0
1681-02-25	0	0	0	0	0
1681-02-26	0	0	0	0	0
1681-02-27	0	0	0	0	0
1681-02-28	0	0	0	0	0
1681-02-29	0	0	0	0	0
1681-03-01	0	0	0	0	0
1681-03-02	0	0	0	0	0
1681-03-03	0	0	0	0	0
1681-03-04	0	0	0	0	0
1681-03-05	0	0	0	0	0
1681-03-06	0	0	0	0	0
1681-03-07	0	0	0	0	0
1681-03-08	0	0	0	0	0
1681-03-09	0	0	0	0	0
1681-03-10	0	0	0	0	0
1681-03-11	0	0	0	0	0
1681-03-12	0	0	0	0	0
1681-03-13	0	0	0	0	0
1681-03-14	0	0	0	0	0
1681-03-15	0	0	0	0	0
1681-03-16	0	0	0	0	0
1681-03-17	0	0	0	0	0
1681-03-18	0	0	0	0	0
1681-03-19	0	0	0	0	0
1681-03-20	0	0	0	0	0
1681-03-21	0	0	0	0	0
1681-03-22	0	0	0	0	0
1681-03-23	0	0	0	0	0
1681-03-24	0	0	0	0	0
1681-03-25	0	0	0	0	0
1681-03-26	0	0	0	0	0
1681-03-27	0	0	0	0	0
1681-03-28	0	0	0	0	0
1681-03-29	0	0	0	0	0
1681-03-30	0	0	0	0	0
1681-03-31	0	0	0	0	0

Figure 2.4: Left panel: Map of the Golden Horn, the Bosphorus and adjacent area from Marsigli (1681). Right panel: Table showing density fluctuations of the Bosphorus waters according to the seasons, as measured from an observation point at Galata.

mation of the northern sill depth (50 m) were the weakness of his hypothesis. Later, Pektaş (1953) claimed that the flow was seasonally blocked under certain conditions whereas Bogdanova (1961, 1965) explained the mechanism that lead to the presence of the Mediterranean water in the Black Sea based on current maps as a result of the prevailing wind conditions over the region and the continuity equation. A concise review about the dynamics of the Bosphorus is given by Ünlüata and Oğuz (1983). Based on the data collected between 1983-1984, Büyükközden et al. (1983) investigated the fate of the Mediterranean water in the Bosphorus and in the Black Sea. A similar study was performed by Tolmazin (1985) the data used were collected far from the Bosphorus-Black Sea Junction. He showed that the Mediterranean water spreads on the Black Sea shelf and follows the route to northeast and then northwest direction. Yüce (1990) showed that the northern sill does not prevent the outflow of the Mediterranean water into the Black Sea and observed high salinity areas ( $\geq 34.0$ -37.3 psu) which are located on the northeast translation route. A review of earlier hydrographic studies in the TSS has been compiled by Ünlüata et al. (1990). Based on the mass balance (Knudsen formula) and the results of Özsoy et al. (1986, 1988), he was able to calculate volume transports in each layer and the corresponding long term mean salinities.

High-resolution salinity measurements conducted during September 1994 with Acous-



tic Doppler Current Profiler (ADCP) and Advanced Microstructure Profiler (AMP) along the Bosphorus are depicted in Figure 2.5. *Gregg et al. (1999)*; *Gregg and Özsoy (2002)* found that the along-channel variation of salinity shows a considerable amount of turbulent mixing and entrainment. The net volume flux is calculated as  $176.7 \text{ km}^3/\text{y}$  towards the Marmara Sea (*Gregg and Özsoy, 2002*) which is lower than the long term estimate of  $\sim 300 \text{ km}^3/\text{y}$  reported by *Ünlüata et al. (1990)*. The hydraulic controls at sill and contraction constitute a unique example of the maximal exchange regime, as foreseen by the cardinal work of *Farmer and Armi (1986)*. *Gregg and Özsoy (2002)* noted the role of frictional effects for the lower net flux. Furthermore, based on ADCP measurements they calculated the two-layer composite Froude number and showed the presence of hydraulic control over the northern sill. However, they failed to demonstrate controls within the constriction, and the southern sill because of lack of data within  $\sim 10 \text{ m}$  layers near the surface and the bottom.

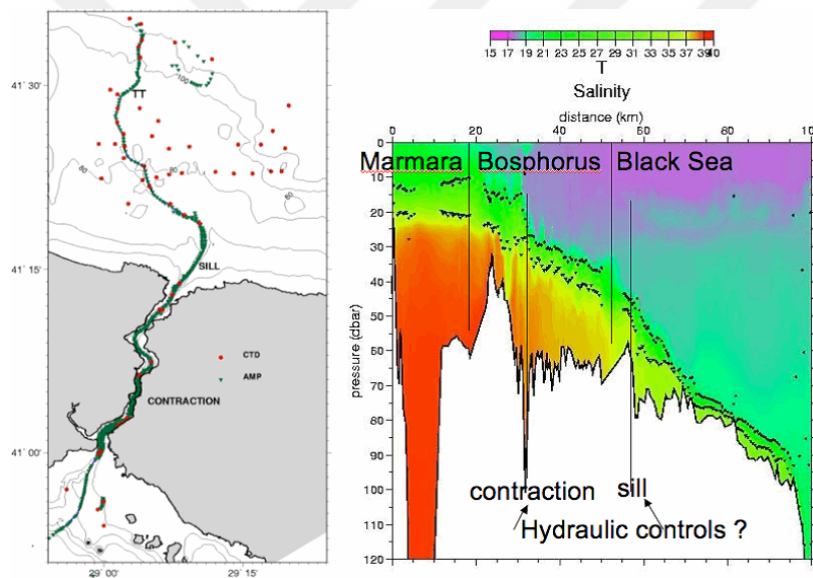


Figure 2.5: R/V BİLİM stations surveyed in September 1994 and the salinity distribution along the Bosphorus Strait and adjacent areas based on continuous profiles (after *Gregg et al. (1999)*).

The details of temperature distribution are not important in the Bosphorus since the density is mainly governed by salinity variations. In the absence of current measurements salinity can be useful to separate the interface from the upper (limits of 18-23 psu) and lower layers (33-38 psu) as depicted by *Oğuz et al. (1990)*. The changes in the salinity field along the Bosphorus are non-linear, corresponding to hydraulic

adjustments occurring apparently in the vicinity of distinctive geometric features of the contraction and the northern and southern sills as shown in Figure 2.5. Moreover, abrupt expansion of the southern Bosphorus intensifies the surface flow in its Marmara Sea Junction resulting in thicker interfacial layer and forming the Bosphorus jet (*Oğuz, 2005*) with a salinity of 21-22 psu. Considerable interfacial mixing and entrainment takes place in the Bosphorus resulting in a total increase of about 3 psu in the upper layer between the two ends of the strait. *Beşiktepe et al. (1994)* highlighted the role of the Bosphorus jet being responsible from half of the mixing in the Marmara Sea. The upper layer enters the Marmara Sea above a depth of about 25 m and proceeds offshore. The upper layer salinity is in the range of  $23 \pm 2$  psu, reaching a maximum in winter as a result due to wind mixing and reduction of the influx from the Black Sea. Upper layer temperature drops to  $7^{\circ}\text{C}$  in winter and rises up to  $22^{\circ}\text{C}$  in summer. In the bottom layer, the temperature is almost constant with an average value of  $14.48^{\circ}\text{C}$  and salinity with an average value of 38.52 psu filling the Bosphorus. As the bottom waters migrate to the north, the layer thickness decreases progressively. In the northern Bosphorus, the interface is relatively sharper with an average thickness of about 5 m located at the depth of 40 to 50 m (*Latif et al., 1991; Oğuz, 2005*). After the northern sill, Marmara water follows a channel, the so called pre-Bosphorus channel, in the Black Sea with a maximum salinity of 36.5 psu below a depth of 50 m and disperses onto the Black Sea continental shelf and successively sinks into the deep layers along the continental slope.

*Çetin (1999)* showed upper-layer salinity range as  $17.5 \pm 1$  and upper-layer temperature value altering between  $4^{\circ}\text{C}$  in the winter and  $22^{\circ}\text{C}$  in the summer on the northern part of the Bosphorus between 1992 and 1998. These findings are in agreement with the values reported by (*Özsoy and Ünlüata, 1997*). The decrease in freshwater input into the Black Sea and increase in the wind stress magnitude is responsible from the larger surface salinities in the winter in the Black Sea. The lower layer salinity is directly related to the Marmara Sea outflow into the Black Sea modified by the Bosphorus dynamics. The range of the temperature and salinity in the bottom layer ranges between  $13^{\circ}\text{C}$  and  $15^{\circ}\text{C}$  and 35 and 37 psu, respectively (*Latif et al., 1991*).

The above investigations are based on long term observational data, therefore have a sampling period on the order of months. However, considerable short term fluctua-

tions are likely to be observed in the Bosphorus as shown with along-strait salinity sections by *Latif et al.* (1991). The water transport to the Marmara Sea through the Bosphorus Strait may be cut or even become reversed in situations when the southwesterly storms pass over the TSS especially in winter months, as indicated by the measurements of *Gunnerson and Özturgut* (1974); *Latif et al.* (1991); *Jarosz et al.* (2011a). Conversely, when high freshwater input from the Black Sea combine with northeasterly winds, the Marmara Sea outflow into the Black Sea may come to halt (*Özsoy et al.*, 1986, 1988). *Latif et al.* (1991) demonstrates that under calm or moderate winds the average situation is the well-known two-layer flow regime in the Bosphorus (Figure 2.6, upper panel). The salinity section on 16 January 1987 depicts the departure from the mean conditions after a period of strong southwesterly winds which resulted in the blocking of the upper layer flow of Black Sea origin. Figure 2.6 (bottom panel) shows 24-28 isohalines rise and reach to the surface indicating the increase in vertical mixing and the swelling of the interfacial layer throughout the strait. *Jarosz et al.* (2011a) established a quantitative relation between the observed stratification and the strength of the exchange by velocity measurements. They estimated the strength of the flow on the basis of observations of wind speed and direction. *Sümer and Bakıoğlu* (1981); *Gregg et al.* (1999) noted that additional to the dynamical forces such as wind and barometric pressure, a net sea level difference of 50 cm between the ends of the Bosphorus is required for the lower layer blocking and  $\leq 10$  cm difference is needed to arrest the upper layer. The results of an idealized hydrodynamic models of the Bosphorus produced comparable results (*Sözer and Özsoy*, 2002).

As mentioned above, *Ünlüata et al.* (1990); *Beşiktepe et al.* (1993, 1994) computed the steady-state average volume fluxes through the TSS with a box model, using salinity measured in the Black, Marmara and Aegean Seas (Figure 2.7, top panel). Based on this method, *Beşiktepe* (2003) computed the seasonal cycle. As the total freshwater input (precipitation and river runoff account for 300 km<sup>3</sup>/yr and 350 km<sup>3</sup>/yr, respectively) is twice as large as the loss in the Black Sea (evaporation constitutes 350 km<sup>3</sup>/yr), the same ratio is implied between upper and lower layer fluxes in the Bosphorus. The computations also show large upward entrainment fluxes in the Marmara Sea and in the Dardanelles Strait due to wind mixing, making the exchange fluxes at the Aegean exit two to three times larger than those in the Bosphorus, and



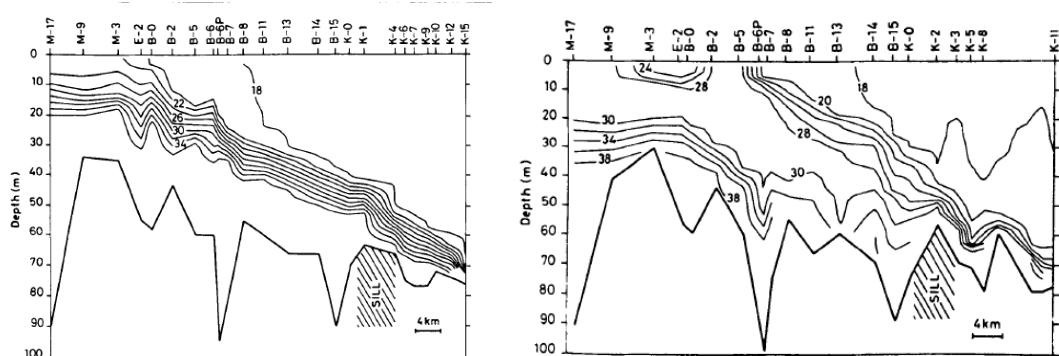


Figure 2.6: Left panel: Salinity section under calm and moderate winds on 21 November 1986. Right panel: Salinity section after a period of strong southwesterly winds on 16 January 1987. Plots are from *Latif et al. (1991)*.

with a smaller difference (30%) between the upper and lower layer fluxes. According to *Beşiktepe (2003)*, the transport through the TSS increases in spring, and weakens markedly in autumn (within a margin of about  $\sim 40\%$  of the annual mean) in response to the changing freshwater input to the Black Sea.

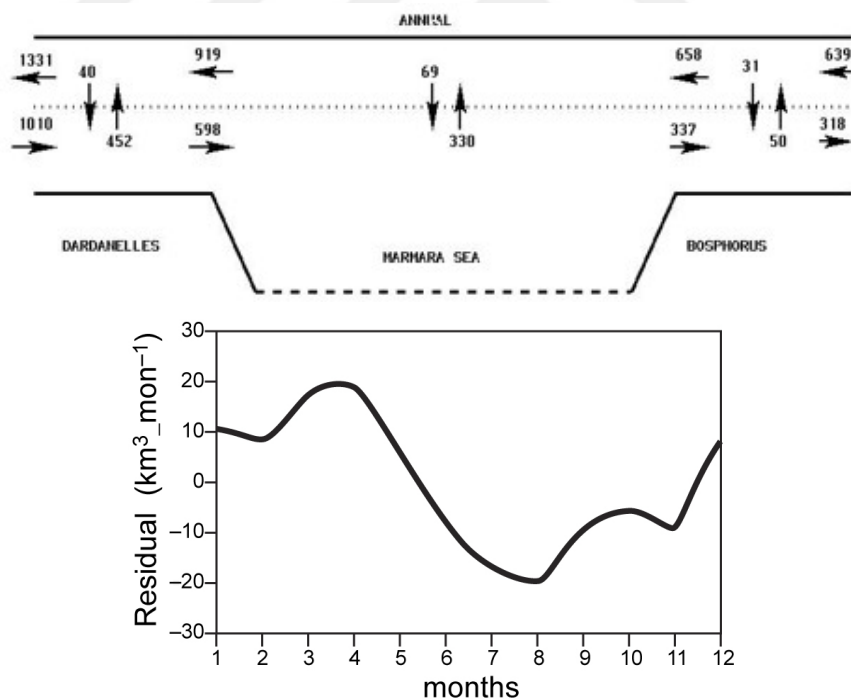


Figure 2.7: Steady-state mean fluxes ( $\text{km}^3/\text{yr}$ ) through the Turkish Straits System and between its individual compartments (after *Beşiktepe (2003)*, top panel) and anomalies of the seasonal cycle of net transport through the Bosphorus Strait based on data from the 1923-1997 period (replotted from *Peneva et al. (2001)*, bottom panel).

Seasonal anomalies of the net transport through the Bosphorus were also indirectly estimated by *Peneva et al. (2001)* and *Stanev and Peneva (2002)* based on long-term measurements and sea level variations in the Black Sea (Figure 2.7, bottom panel). One issue with indirect estimates is the availability and quality of the data. Comparing deviations of  $\sim 240 \text{ km}^3/\text{yr}$  in Figure 2.7 (bottom panel) with the mean transport of  $320 \text{ km}^3/\text{yr}$  computed by *Beşiktepe (2003)*, seasonal variations would be  $\sim 75\%$  of the mean, that is considerably larger than the  $\sim 40\%$  estimated by *Beşiktepe (2003)* from mass budget calculations. These differences arise from data uncertainties as well as differences in averaging (monthly versus seasonal) applied to the data. However, both methods yield the same general pattern of seasonal variation.

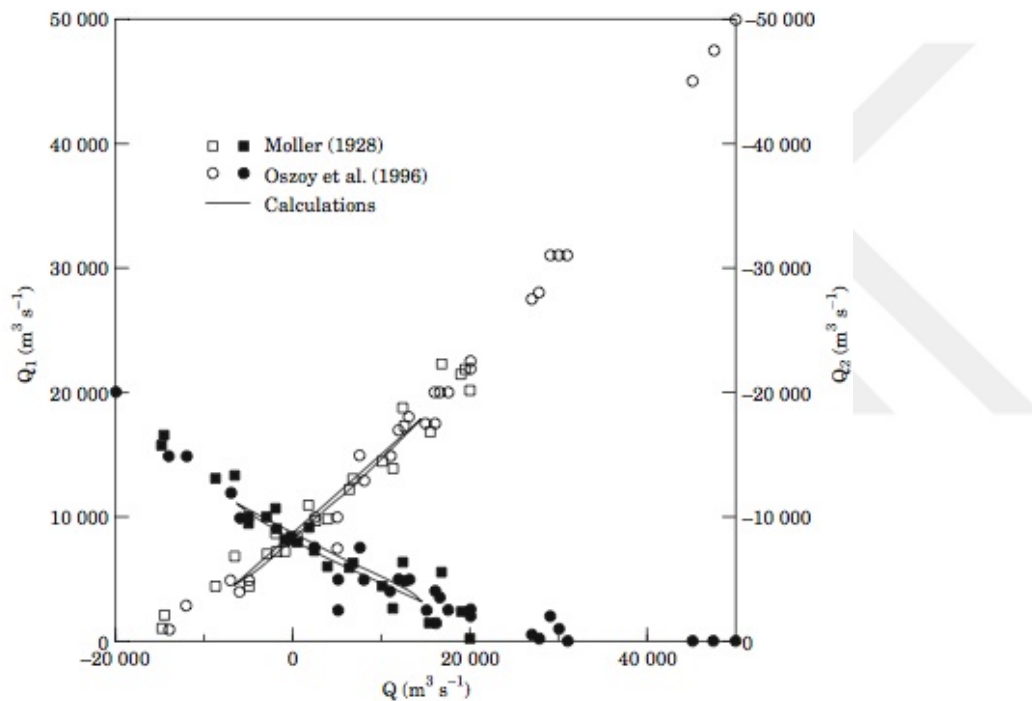


Figure 2.8: The volumetric flow rate in the upper layer, defined as  $Q_1$  (open symbols), and in the bottom layer, defined as  $Q_2$  (filled symbols), of the Bosphorus versus net flow  $Q$ . Here circles and squares represent the data of Merz (*Möller, 1928*) and (*Özsoy et al., 1986, 1988*), respectively. The solid curves represent the result from a simple model (*Maderich and Konstantinov, 2002*) (conversion factor:  $1 \text{ m}^3/\text{s} = 0.0315 \text{ km}^3/\text{yr}$ ).

Directly measured fluxes from ship mounted ADCP measurements in the Bosphorus (*Özsoy et al., 1986, 1988*) show the same seasonal trends as reviewed above (Figure

2.8). These measurements reveal maxima of about  $Q_1 = 1600 \text{ km}^3/\text{yr}$  and  $Q_2 = 630 \text{ km}^3/\text{yr}$  for the upper and lower layers respectively, indicating instantaneous fluxes 2-3 times larger than the annual mean. Despite large scatter in data due to sampling, steady-state average values of  $Q_1 = 540 \text{ km}^3/\text{yr}$  and  $Q_2 = 115 \text{ km}^3/\text{yr}$  were computed, the latter value possibly being underestimated as a result of data loss near the bottom. Figure 2.8 depicts a summary of the data compiled by *Maderich and Konstantinov* (2002), including a comparison with their simple model. The data indicate that the upper or lower layer flow is blocked when the net flux exceeds  $Q = -580 \text{ km}^3/\text{yr}$  or  $Q = 800 \text{ km}^3/\text{yr}$  in respective directions, the latter estimate being consistent with the results of a two layer model (*Oğuz et al.*, 1990).

*Altıok* (2010) calculated the variability in the upper layer,  $Q_1 = 5\text{-}1051 \text{ km}^3/\text{yr}$  and in the lower layer,  $Q_2 = 0.6\text{-}866 \text{ km}^3/\text{yr}$  at the northern Bosphorus based on monthly ADCP transects for the period of 10 years between 1999 and 2009. For the same time period, they noted the upper layer flux,  $Q_1 = 0\text{-}1216 \text{ km}^3/\text{yr}$  and lower layer flux,  $Q_2 = 0\text{-}654 \text{ km}^3/\text{yr}$  at the mid-distance between the south exit and the contraction. These findings reveal that there is a significant amount of entrainment between the layers. The measurements are from the moorings containing ADCPs deployed at two ends of the strait for the period of September 2008 to February 2009 (*Jarosz et al.*, 2011b). The estimated upper and lower layer fluxes are  $410 \text{ km}^3/\text{yr}$  and  $293 \text{ km}^3/\text{yr}$ , respectively with the maximum values of  $1500 \text{ km}^3/\text{yr}$  and  $1100 \text{ km}^3/\text{yr}$ . These average values match with the findings of the *Altıok* (2010).

The sea level difference between the two ends of the Bosphorus Strait is generally greater during spring and early summer (28-56 cm with the mean of  $40 \pm 3 \text{ cm}$ ) and lower during autumn and winter (19-35 cm with the mean of  $23 \pm 3 \text{ cm}$ ) (*Alpar and Yüce*, 1998). This is correlated with the amount of net freshwater influx to the Black Sea. The tidal sea level oscillations are semi-diurnal and are small enough to be ignored compared to the mean sea level difference in the Bosphorus (2 cm, *Yüce and Alpar* (1994), 10 cm, *Büyükkay* (1989)). The meteorological conditions are responsible for the long period sea level variations in the Bosphorus Strait on the order of 3-14 day *Büyükkay* (1989). The low-frequency oscillations show 5-30 days periodicity. The mesoscale atmospheric variations leads to 5-day periodic oscillations (*Yüce and Alpar*, 1994). The meteorological conditions are dominated by continuous passages of

cyclonic low pressure systems (*De Filippi et al.*, 1989) with a peak value of 30m/s as gusts reported by *Ünlüata et al.* (1990) during the winter. Northerly winds are dominant during the summer. Northerly winds are dominant with a frequency of 60%, with southerlies occurring 20% on annual basis (*De Filippi et al.*, 1989). During the winter winds from either direction are equal both in strength and frequency. Winds have an effect on the flow in the TSS through a change of sea level in the exit regions of the Black and the Mediterranean Seas. Barometric pressure is an important parameter and related to the sea level changes and fluctuations (*Büyükkay*, 1989; *Yüce and Alpar*, 1994; *Book et al.*, 2014). *Yüce and Alpar* (1994) displayed the spectral analysis of the barometric pressure showing the long period of oscillations with periodicity from 4.7 to 21.3 days. He also reported that the power spectra of the sea level data has peaks at 28.4, 14.2, 6.2, 5.2 and 4.4 days. Consequently, the short frequency oscillation correlates with the pressure variation well. Furthermore, cross spectra analysis confirms this correlation (*Yüce and Alpar*, 1994).

### **The Marmara Sea**

Being part of the Turkish strait system, the Marmara Sea has a two-layer stratification, as well. The low-salinity surface water ( $\sim 23$  psu) is separated from the saltier ( $\sim 38$  psu) Mediterranean water by a strong pycnocline located at a depth of about 25m. The Sea of Marmara receives an inflow from the Bosphorus which is about 50 times the cumulative annual discharge of the small rivers entering it. The residence times for the upper and lower layers are estimated to be 4 to 5 months and 6 to 7 years, respectively (*Beşiktepe et al.*, 1994). The surface outflow from the Bosphorus into the Sea of Marmara and also from the Dardanelles into the Aegean Sea occurs in the form of a surface buoyant jet. The jet flow drives a current that meanders at basin scale (Figure 2.9) transporting materials towards the Dardanelles Strait. The intense initial jet structure at the exit of the Bosphorus at the same time creates turbulent horizontal and vertical mixing and entrainment that contributes to the basin primary productivity. Transects of temperature and salinity across the entire length of the Turkish Straits System show that the most rapid variations occur within and at the exit regions of the straits (Figure 2.10). The rate of increase in salinity in the upper layer and the slope of the interface are the largest in the southern Bosphorus area and

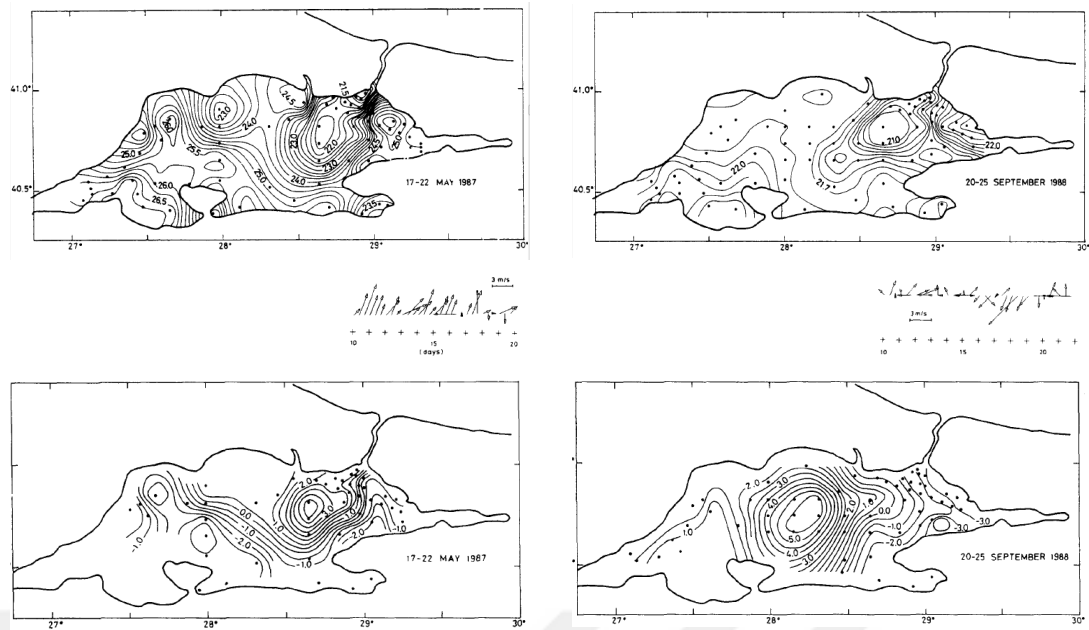


Figure 2.9: Examples of surface salinity distributions (top panel) and horizontal circulation patterns (bottom panel) in the Sea of Marmara (from *Beşiktepe et al. (1994)*).

its exit to the Marmara Sea, and also in the western part of the Dardanelles Strait. The Cold Intermediate Water, identified by its signature in the Black Sea (blue color in Figure 2.10, lower panel) enters the Bosphorus upper layer and gets mixed to reach the surface after its passage through a hydraulic transition in the southern part of the strait.

Significant mixing occurs inside the Straits (Figure 2.10), and further by surface buoyant jets (Figure 2.9) at the exits of the two straits to the wider sea regions. The surface plumes carrying relatively fresh water and chemical / biological signatures from their sources affect material cycling in the target basins not only through transport, but also as a result of efficient turbulent mixing and entrainment in the exit regions. Interfacial mixing at the straits and jet mixing near their exit regions yield the highest horizontal rates of change in properties within the TSS (Figures 2.9, 2.10, and 2.11) and largely determine the cycling of matter and biological productivity of the confined waters of the Marmara Sea; a fact emphasized earlier by *Ünlüata et al. (1990)* and *Beşiktepe et al. (1994)*.

The surface and deep features of the Marmara Sea hydrography are displayed via salinity surface and interior distributions in Figure 2.12. The dense water entering

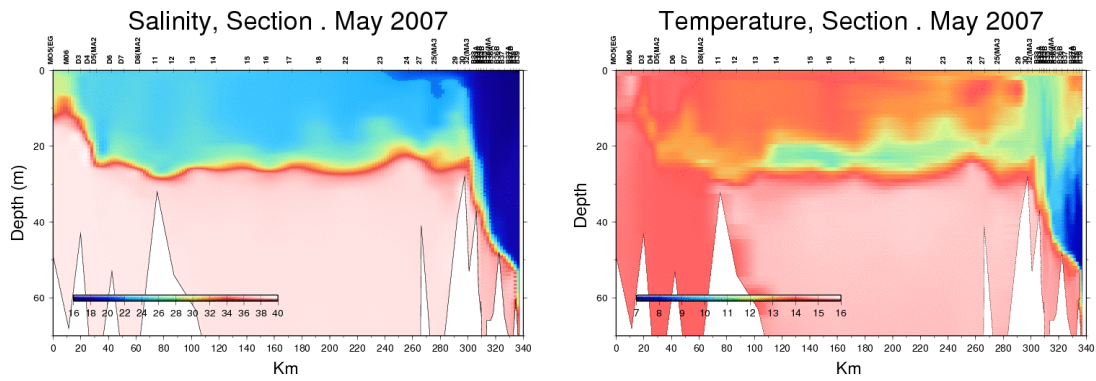
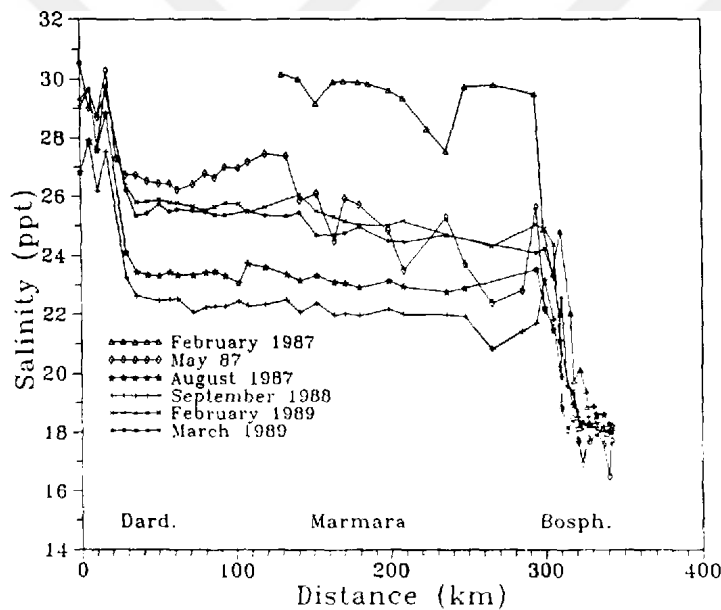


Figure 2.10: Transects of salinity (top panel) and temperature (bottom panel) across the TSS, along the main axis extending from the Aegean Sea to the Black Sea through the Dardanelles Strait (0-120 km), Marmara Sea (120-300 km) and Bosphorus Strait (300-340 km). The data was collected on board of R/V Bilim-2 during a field survey in May 2007.



Upper layer averaged salinity distribution along the main axis of the Turkish Straits System for different months.

Figure 2.11: Upper layer average salinity variations along the main axis of the Turkish Straits System in different months sampled by cruise data (taken from Ünlüata *et al.*, 1990).

through the Dardanelles sinks to a depth of neutral buoyancy. The depth to which the plume sinks is determined by the properties of the Dardanelles throughflow and the interior stratification (Beşiktepe *et al.*, 1993, 1994). In winter the densest water of the

Dardanelles inflow creates a plume which sinks to the bottom of the western Marmara Sea basin. This plume of water replenishes deep waters in the western basin, and is identified with its relatively higher salinity values.

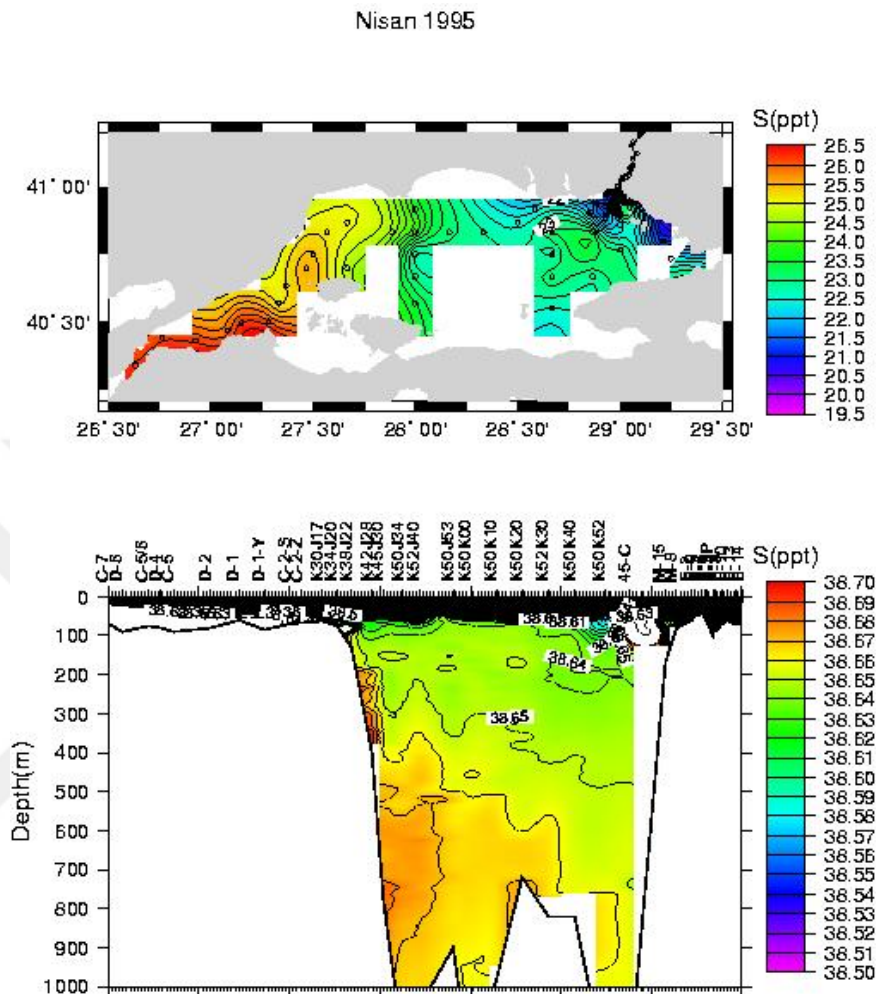


Figure 2.12: Marmara Sea salinity variations in April 1995: at 5 m depth (top panel), and west to east along the main axis (bottom panel).

The Sea of Marmara is too small to generate its own tides, but a tidal signal reaches it through the Dardanelles and the Bosphorus. In the southern part of Bosphorus the mean spring tidal range is less than 4 cm (*Alpar and Yüce, 1998*).

## Dardanelles

Dardanelles Strait constitutes a two-layer system similar to the remaining domain of the TSS. The relatively less saline water of the Marmara Sea ( $\sim 25\text{-}29$  psu) originating



from the Black Sea disperse into the North Aegean Sea as a negatively buoyant upper layer flow changing the water properties of the region (*Androulidakis et al.*, 2012). The Mediterranean Sea water with a salinity of  $\sim 38.9$  enters the Marmara Sea in the lower layer inflow through the Dardanelles Strait (*Beşiktepe et al.*, 1993). Based on results of a circulation model, *Androulidakis and Kourafalou* (2011) showed the strong influence of the buoyant outflow of the Dardanelles plume on the North Aegean Sea circulation. The impact of the Black Sea water outflow on the North Aegean Sea (*Poulos et al.*, 1997) and further on the Eastern Mediterranean Transient (EMT) has been investigated by (*Zervakis et al.*, 2000, 2004).

The United States Naval Research Laboratory (NRL) and the North Atlantic Treaty Organization (NATO) Undersea Research Center (NURC) in collaboration with the Turkish Navy Office of Navigation, Hydrography and Oceanography initiated a joint measurement and survey program in the TSS starting from 28-29 August 2008 until 11 October 2009. They deployed two moorings on each exit of the Dardanelles to measure temperature, salinity, full water column velocity and the bottom pressure. The results show that the volume transport through the Dardanelles does not change on monthly scale. On the other hand, there is significant variability in the fluxes on shorter time scale (2-10 days). In the upper layer, the wind stress and bottom pressure anomaly gradient controls the variability, whereas in the bottom layer, the fluctuations are related solely to the bottom pressure anomaly gradient (*Jarosz et al.*, 2012). The upper layer thickness is measured 32 m in the northern and 17 m in the southern reaches of the Dardanelles in winter. A thin upper layer can produce flow reversals under severe wind episodes from the southwest. Upper layer current velocity can reach more than 2 m/s in the vicinity of the abrupt expansion in the Aegean Sea (*Jarosz et al.*, 2012).

The sea level difference between the two ends of the Dardanelles Strait reaches a maximum in early spring and late summer and drops to a minimum in winter (*Alpar and Yüce*, 1998). The difference ranges between 12-18 cm in spite of the change in barometric pressure and hydrology of the TSS that is under the influence of the Black Sea freshwater inflow (*Alpar and Yüce*, 1998). Consequently, the mean sea level in the vicinity of the Black Sea-Bosphorus Junction is  $\sim 55$  cm higher than the level at the Aegean Sea-Dardanelles Junction. The general nature of the sea level variations



and the short, tidal and long period of oscillations in the Dardanelles are analyzed by *Yüce* (1994). By using two stations, one from the mid-strait and another one from northern end of the strait for the analysis, he found out that the water level fluctuation in the Dardanelles Strait is primarily dominated by the semi-diurnal frequency which is co-oscillating with the Aegean Sea. Low tidal amplitude is weak and is limited to 10 cm. The mean spring tidal ranges up to 19 cm in the mid-strait and up to 5.5 cm north of the strait indicating a decrease towards the Marmara Sea. Southerly winds have a major impact on the water level fluctuations on short term (10.9 h, 3.0 h, 90 min oscillations), whereas the barometric pressure is responsible for the long period of oscillations (several days).

Atmospheric pressure is an important to show the flux variability to extreme storms. *Book et al.* (2014) has investigated the response of the TSS to an extreme atmospheric pressure drop of more than 30 mb in less than 48 h. The Aegean exit of the Dardanelles shows a bottom pressure response consistent with the atmospheric pressure drop. Upper layer flow of the Dardanelles was reversed as a result of rapid increase in sea level (the bottom pressure, as well) before the storm affects the Marmara Sea. *Book et al.* (2014) developed a conceptual model without atmospheric forcing showing high correlations ( $r=0.89-0.96$ ) between bottom pressure and atmospheric pressure.

## **2.4 Review of earlier modeling efforts**

A series of previous ocean modeling efforts involving the TSS have been initiated at the IMS-METU (*Oğuz and Sur*, 1989; *Oğuz et al.*, 1990; *Beşiktepe et al.*, 1994; *Hüsrevoğlu*, 1999; *Oğuz*, 2005; *Ilıcak et al.*, 2009; *Sözer and Özsoy*, 2002). Presently, a 'Turkish Straits Model Hierarchy' is being developed at the IMS to establish a predictive capability specifically geared for the TSS. Along this route, the Regional Ocean Modeling System (ROMS; *Shchepetkin and McWilliams* (2005)) is used separately for the Bosphorus and Dardanelles Straits and for the Marmara Sea, at high spatial resolution. In addition, a two-dimensional (in the horizontal) finite element model, the TUGOm, has been used to predict barotropic fluxes through the TSS, forced by the adjacent basins. Furthermore, a two-dimensional (in the vertical) model solving

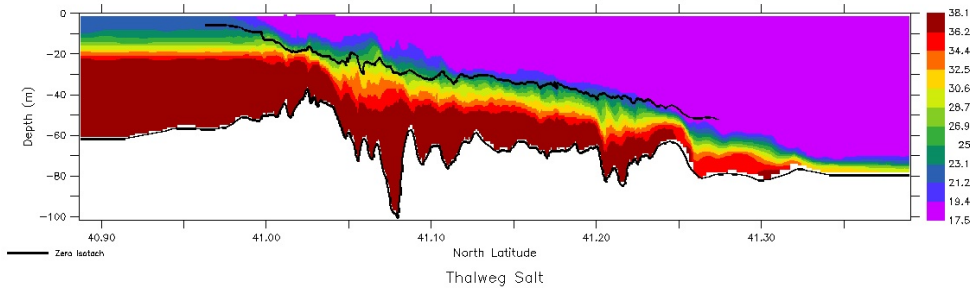


Figure 2.13: Salinity distribution and the line of zero velocity (black line) in the Bosphorus obtained from a three dimensional hydrodynamic model (ROMS) of the Bosphorus exchange flow (Sözer, 2013). The boundary conditions are defined by adjacent basin properties after Gregg and Özsoy (2002) with an imposed barotropic flux of  $5600 \text{ m}^3/\text{s}$ , GLS turbulence parameterization and a minimum horizontal resolution of 50 m.

vorticity, heat and salt conservation equations has been used to test turbulent mixing schemes (Ilıcak et al., 2009).

A two dimensional model solving equations integrated across the Dardanelles Strait has been developed by Staschuk and Hutter (2001). Three dimensional models have been tested for the Bosphorus by Sözer and Özsoy (2002); Oğuz (2005); Sözer (2013). Some observed features such as blocking and hydraulic transitions of the flow (Latif et al., 1991) and sharp changes of the free-surface at the contraction (Gregg et al., 1999; Gregg and Özsoy, 2002) have been demonstrated by some of the above models. Nevertheless, the results are far from being fully representative of the coupled dynamics of the TSS. A three dimensional model of the Dardanelles Strait has been developed by Kanarska and Maderich (2008). A number of efforts are continuing at present to make use of three dimensional models with advanced physics options to produce realistic predictions of the behavior of the TSS or its components. Figure 2.13 shows as an example the salinity features in the Bosphorus based on the three-dimensional model results of Sözer (2013). Reduced gravity or vertical plane two dimensional models have been developed for cascading flows resulting from the exit of dense water from the straits into adjacent basins (Hüsrevoğlu, 1999; Özsoy et al., 2001; Stanev et al., 2001; Staschuk and Hutter, 2001).

A one-dimensional model of the Bosphorus Strait with an entraining interface was

used by *Oğuz et al.* (1990). The model can explain the quasi-steady behavior of the Bosphorus flow. The presence of the hydraulic controls at the northern sill and the south-exit are also demonstrated. *Oğuz et al.* (1990) noted that the presence of the critical flow at the constriction depends on the strength of the upper-layer flows and the isolated subcritical between the supercritical regions in the north and south Bosphorus region is extended into the Bosphorus-Marmara Sea junction. *Johns and Oğuz* (1989) demonstrated the two-layer stratification and the penetration of high salinity bottom layer water into the fresher upper layer water in a simple uniform rectangular cross-sectional area using a two-dimensional multi-level channel model. They conclude that the Bosphorus flow has a strict three-dimensional character and can only be simulated using a three-dimensional numerical model. The three dimensional Princeton Ocean Model (POM) is employed to obtain the basic understanding of the relation between the hydraulic adjustment and Bosphorus geometry (*Oğuz, 2005*). Numerical solutions showed that the two-layer, quasi-steady exchange flow of the Bosphorus is altered by the hydraulic transitions and modulated by the morphological features. The approximate location of the hydraulic controls is assumed to be the regions of flow with Richardson number  $R_i \leq 0.25$ , where

$$R_i = \frac{g}{\rho} \frac{\partial \rho / \partial z}{|\partial \vec{u} / \partial z|^2}$$

*Sözer* (2013) used the three-dimensional free-surface primitive equation sigma-layer ROMS model in his extensive Bosphorus Strait study. He depicted the along-channel and cross-channel variability of hydrodynamic characteristics and the response of the system to various barotropic forcing. However, this is not the first three dimensional modeling study. *Öztürk et al.* (2012) has calibrated and validated the MIKE 3 hydrodynamic model with various data sets and extended it to simulate storm conditions to analyze the current maps of the case study.

Neural network models based on statistical tools have been used to estimate vertical current profiles in the Bosphorus from input data such as sea level, wind and barometric pressure measured at several stations (*Aydoğan et al., 2010*). High accuracy estimations of currents with an average root mean square error of 16 cm/s have been achieved after training of the system, allowing statistical forecasts for up to 12 h in

the future. Similarly, least squares estimates of water level from air pressure and wind stress give reasonable estimates with an average error of 5 cm (*Andersen et al.*, 1997). Additionally, *Jarosz et al.* (2011a) proposed an empiric relationship to calculate the Bosphorus fluxes as a function of wind stress and bottom pressure.

*Johns and Oğuz* (1989) showed the importance of the three dimensional modeling for the Bosphorus Strait and similar approach can be done for the Dardanelles, as well. Nevertheless, the numerical simulation of the water exchange and the thermohaline structure between the North Aegean Sea and the Marmara Sea through the Dardanelles is a challenge to solve in three dimensions without any simplification. A simplified two layer model was used by *Oğuz and Sur* (1989) to study the water exchange through the Dardanelles Strait. They considered a system of two homogeneous layers of different densities separated by an entraining interface. The exchange of mass and momentum between the layers is permitted and based on the turbulence analysis and mean flow energy interactions in the layers. The model consolidate mixing and friction at the surface, bottom and more importantly along the interface. They realized two hydraulic controls in the Dardanelles where there is the contraction at the Nara Passage and at the abrupt expansion of the width at its Aegean exit. They predicted 23% of the North Aegean originated water in volume is entrainment into the upper layer returned back. However, this model uses vertically integrated balances which cannot explain the details in the subsurface salinity and temperature distributions.

*Gündüz and Özsoy* (2015) incorporated a numerical ocean model of the TSS to predict transports of water at the Dardanelles Strait in order to assess the relationship between the blocking events and wind stress magnitude and direction in the North Aegean Sea. The results helped to understand the possible influence of the Dardanelles Strait blocking on fish migration.

Numerical experiments on the hydrodynamics of the Marmara Sea are limited. A simplified box model to interpret the vertical spread of the Mediterranean water in the Marmara Sea was presented by *Beşiktepe et al.* (1993). A significantly idealized three-dimensional nonlinear numerical ocean model with coarse horizontal resolution is used to simulate the temperature and salinity fields in the Marmara Sea and their influence on Bosphorus and Dardanelles Strait (*Demyshev and Dovgaya*, 2007). A

high resolution version of this model, excluding the atmospheric forcing, is used to quantify the influence of the seasonal temperature signal in the upper layer of the Bosphorus on the circulation of the Marmara Sea (*Demyshev et al., 2012*). After integrating it 18 years with 0.5min time step, the mean circulation field shows a well defined meandering S-shaped jet over the Marmara Sea with 60cm/s in magnitude reaching down to 40m depth level. Furthermore, an anti-cyclonic eddy is formed in the northeastern part which persisted until the end of the simulation. A cyclonic eddy (50km in diameter) appeared near the northern shelf between March and November. (*Demyshev et al., 2012*) analyzed the temperature and salinity fields to explain the formation of this eddy. They speculate that an increase in temperature of the Bosphorus outflow into the Marmara Sea reduces the cross-jet gradient in density field. Reducing advection and increase in diffusion widens the jet and cold, salty waters are pushed towards the north and high density water leading to the cyclonic motion.

*Chiggiato et al. (2012)* used the ROMS model to produce the general circulation and understand the key forcing dynamics associated to the currents in the Marmara Sea. They found that the wind stress curl and the straits flow changes the strength and the position of the mesoscale cyclonic and anticyclonic eddies formed in the Marmara Sea. Furthermore, they related the large displacement of the pycnocline to the upwelling and downwelling as a result result of northeasterly winds.



## CHAPTER 3

### FINITE ELEMENT OCEAN MODEL

In this chapter, I describe the ocean general circulation model this work is based on, by presenting the governing equations, their discretization, parameterization of sub-grid scale processes and the model setup such as initial and boundary conditions and atmospheric forcing.

The Finite Element Ocean Model has been developed in the last decade in the Climate Dynamics Group of the Alfred Wegener Institute. It is the first global ocean general circulation model based on the unstructured mesh approach and aimed to serve mainly for climate research (*Wang et al.*, 2014). FEOM is employed in a wide range of applications and tests with global configuration (*Danilov et al.*, 2004; *Sidorenko et al.*, 2011; *Wang et al.*, 2012; *Wekerle et al.*, 2013). Having a free surface representation, it solves the hydrostatic primitive equations in the Boussinesq approximation. It is coupled to a sea ice model, the so-called Finite-Element-Sea-Ice-Ocean-Model (FE-SOM, *Timmermann et al.* (2009)) and to an atmosphere model (ECHAM6, *Sidorenko et al.* (2015)).

Its multi-resolution property provides FEOM with flexibility to represent complex geometries and rugged topographies such as narrow straits, headlands and islands. With local mesh refinement, the model avoids coarse and step-wise representation of boundaries and bathymetry. This helps to overcome possible challenges related to numerical artifacts on ocean circulation (*Adcroft and Marshall*, 1998; *Dupont et al.*, 2003) and strengthens its performance. FEOM is also available in a regional version.

### 3.1 Governing Equations

FEOM solves the standard set of hydrostatic primitive equations under the Boussinesq approximation. The solution of the system of governing equations is step-wise and is split into the dynamical and the thermodynamical parts staggered with a half time-step. Time stepping is implicit. The *dynamical part* contains the momentum equations in 3 dimensions and the vertically integrated continuity equation. This part is solved for horizontal velocity, sea surface height and pressure. In the *thermodynamical part*, the advective-diffusive tracer equations are solved for potential temperature, salinity and density anomaly. Density is computed from the equation of state (*Jackett and McDougall, 1995*).

First, the equations solved in the dynamical part are presented. The momentum equation links the time dependency, advection and Coriolis terms, the left hand side, to the barotropic, baroclinic and diffusive terms, the right hand side. Here, the diffusive term is split into its horizontal and vertical components by virtue of dissimilar time and spatial scales:

$$\partial_t \mathbf{u} + \mathbf{v} \cdot \nabla_3 \mathbf{u} + f(\mathbf{k} \times \mathbf{u}) = -g \nabla \eta - \frac{1}{\rho_0} \nabla p + \nabla \cdot A_h \nabla \mathbf{u} + \partial_z A_v \partial_z \mathbf{u}, \quad (3.1)$$

where  $\mathbf{v} \equiv (\mathbf{u}, w) \equiv (u, v, w)$  is the velocity vector in spherical coordinates,  $f$  stands for the latitude-dependent Coriolis parameter ( $f(\theta)$ ),  $\mathbf{k}$  denotes the local vertical unit vector,  $g$  is the gravitational acceleration,  $\rho_0$  and  $\rho$  are the average sea water density and the deviation from it, respectively, and  $\eta$  denotes the sea surface height.  $A_h$  and  $A_v$  are the lateral and vertical momentum diffusion coefficients, respectively.

The vertically integrated continuity equation is coupled to the freshwater fluxes into the ocean, the sum of precipitation and river runoff, and out of the ocean in the form of evaporation:

$$\partial_t \eta + \nabla \cdot \int_{z=-H}^{z=\eta} \mathbf{u} dz = \mathbf{E} - \mathbf{P} - \mathbf{R}. \quad (3.2)$$

The upper limit in the integration is set to zero, which denotes a linear free-surface approximation. Although this approximation may not seem to be a good choice considering the thickness of the first layer of the model, for practical reasons it is kept as zero. If the term containing the time derivative together with  $E - P - R$  in equation



3.2 is omitted, then the rigid-lid approximation that surpasses fast gravity waves is obtained.  $\nabla$  and  $\nabla_3$  symbolize the 2-dimensional and 3-dimensional gradient and divergence operators, respectively.

The hydrostatic equation is used to diagnose the hydrostatic pressure:

$$\partial_z p = -g \rho, \quad (3.3)$$

where  $p$  is the hydrostatic pressure anomaly which is obtained by integrating in the vertical from the bottom to the surface and  $\rho$  is the deviation from the average sea water density.

The above equations are solved in the domain  $\Omega$ , which is limited by three different types of boundaries  $\partial\Omega = \bigcup_{i=1}^3 \Gamma_i$ .  $\Gamma_1 : \{z = 0\}$  denotes the ocean surface,  $\Gamma_2 : \{z = -H(\lambda, \theta)\}$  stands for the ocean bottom and  $\Gamma_3$  stands for the lateral vertical rigid walls. Unlike the surface boundary where the vertical momentum diffusion is linked to the tangential wind stress, i.e. momentum flux continuity, on the bottom momentum dissipation is balanced by the bottom drag condition:

$$\partial_z A_v \partial_z \mathbf{u} = \tau, \quad p = 0 \text{ on } \Gamma_1, \quad (3.4)$$

$$\partial_z A_v \partial_z \mathbf{u} + A_h \nabla H \cdot \nabla \mathbf{u} = C_d \mathbf{u} |\mathbf{u}| \text{ on } \Gamma_2, \quad (3.5)$$

where  $\tau$  is the wind stress and  $C_d$  is the bottom drag coefficient.

On the vertical rigid walls, no normal flow is allowed. No-slip boundary conditions are applied, meaning that the tangential velocity along the vertical wall is zero. Free-slip conditions requires the tangential component of the viscous stress to be zero. All through this study the choice is the no-slip condition:

$$\mathbf{u} \cdot \mathbf{n} = 0 \text{ and } \mathbf{u} = 0 \text{ on } \Gamma_3, \quad (3.6)$$

Here  $\mathbf{n}$  denotes the unit normal vector to the rigid wall.

The vertical velocity  $w$  is diagnosed from the continuity equation:

$$\partial_z w = -\nabla \cdot \mathbf{u}, \quad (3.7)$$

which has the following kinematic boundary conditions at the surface and at the bottom:

$$w = \partial_t \eta + \mathbf{u} \cdot \nabla \eta + (\mathbf{E} - \mathbf{P} - \mathbf{R}) \text{ on } \Gamma_1, \quad (3.8)$$

$$w = -\nabla H \cdot \mathbf{u} \text{ on } \Gamma_2. \quad (3.9)$$

In the thermodynamical part of the ocean model the following equation set is solved:

$$\partial_t C + \mathbf{v} \cdot \nabla_3 C = \nabla \cdot K_h \nabla C + \partial_z K_v \partial_z C, \quad (3.10)$$

with  $C$  standing for any tracer variable such as potential temperature,  $T$  or salinity,  $S$  and  $K_h$  and  $K_v$  represents the lateral and vertical diffusivity for the particular tracer, respectively. The following boundary conditions have to be fulfilled for the tracer equations:

$$K_v \partial_z C = -q, \text{ on } \Gamma_1, \quad (3.11)$$

$$(\nabla C, \partial_z C) \cdot \mathbf{n}_3 = 0 \text{ on } \Gamma_2 \cup \Gamma_3, \quad (3.12)$$

where  $q$  is the surface flux for  $T$  and  $S$ .

Density is a nonlinear function of pressure, potential temperature and salinity, and diagnosed via the equation of state according to *Jackett and McDougall* (1995):

$$\rho = \rho(T, S, p). \quad (3.13)$$

## 3.2 Mesh Generation

Unstructured-mesh models are generally more costly than similar finite difference models due to increased number of operations (*Danilov et al.*, 2008). Proper definition of the computation area is strictly recommended to reduce cost. In other words, the proportion between the zone of interest and the whole domain should be optimal to ensure the required efficiency.

The governing equations are defined in a continuous space. Numerical solution of the aforementioned set of equations however, requires discretization on a finite set of points in order to get an algebraic form so that the equation set is solved systematically in an efficient way. These points form the finite elements and elements are packed together to produce the 'mesh'. The mesh generation is not an automatic procedure and has to be performed by the model user. This stage is very important since it decides directly on the quality of the numerical solution. There exist several projects and associated codes about how to generate a mesh for finite elements, however here is no canonical code to be recommended for a general case. FEOM utilizes unstructured triangular surface meshes in two dimensions and tetrahedral elements in

the volume. It uses classical z-coordinates (geopotential levels) in the vertical. The three dimensional mesh is derived from the two dimensional surface mesh by adding and aligning the surface nodes in the vertical. Vertical placement of three dimensional nodal points is important to obtain correct pressure gradient field. Otherwise, spurious pressure modes may disrupt the stability of the numerical solution. Therefore, the design of surface meshes calls great attention. Once the surface mesh is ready the 3D mesh can be created as described in section 3.2.2.

### 3.2.1 2D Mesh (Surface Mesh)

The two dimensional triangular surface mesh can be generated via one of the freely available mesh generators. For a quick and simple mesh, MATLAB function '*delaunay*' is a recommended solution for the triangulation. An alternative method for the 2D mesh generation is a MATLAB package developed by *Persson and Strang* (2004). This package contains a user manual explaining the approach, the supplementary codes used and the steps that are necessary to follow for the surface triangulation. Increasing the number of surface nodes (elements) drops the performance of the code considerably. A faster choice is based on using mesh generator TRIANGLE, (*Shewchuk*, 1996). Yet, it requires the coast lines information. This mesh generator is developed by Jonathan Richard Shevchuk from the University of California at Berkeley (<http://www.cs.cmu.edu/quake/triangle.html>). In this work, the last code, TRIANGLE, is used.

Mesh generation with TRIANGLE has the following steps:

- First, describe the external boundaries of the model domain. For this, specifying a polygon based on the information either from a coastline or a user defined iso-lines. Specify the attributes of the nodes, say open boundary or closed boundary nodes. The attributes of the boundary nodes are conservative and will be carried to the next step. Additionally an arbitrary number of internal nodes might be prescribed then will become triangle vertices in the final mesh.
- Compute the initial triangulation. Determine and/or limit the size of the triangles specified by the minimum height in a triangle (*Wang et al.*, 2014) and do

quality control checks of them the based on the smallest angle.

- Refine initial triangulation considering the position, or topography and/or topography gradient. TRIANGLE checks the validity of the user-specified criteria for further refinement.
- Apply smoothing routines after the mesh generations to improve the mesh quality before model runs are performed. This includes some iterations of edge swapping, and relaxations o equalize angles and edges in neighboring triangles. Check the regions with sudden changes in resolution or the distorted triangles with small angles which are the source of ill-conditioned matrices.

### 3.2.2 3D Mesh

Once the surface mesh is generated, the 3D mesh has to be created. For this purpose, the vertical coordinate type has to be decided. FEOM supports different vertical coordinate types. Vertical levels can be arranged based on the geopotential levels ( $z$ -layer). In this case, the number of the layers in a water column is determined by the topography. If the vertical layer numbers are kept constant, then the thickness of the elements is variable and is adjusted compatible to the water column depth. This setup is called ' $\sigma$ ' coordinate. The vertical resolution can be enhanced in certain depths by the help of coefficients.  $z$ -layer or  $\sigma$  coordinate mesh types can generated automatically by the Fortran routines. Besides the full cell  $z$ -level and  $\sigma$  grids, FEOM supports the  $z + \sigma$  grids and  $z$ -level grids with shaved bottom elements. A  $z + \sigma$  grid combines  $z$ -levels and several  $\sigma$  levels close to the bottom. The number of  $\sigma$  layers and level thicknesses should be adjusted depending on the application. There are two types of shaved cell grids. If the surface mesh is generated without considering bottom topography, full cell elements might still be required in regions of steep slopes where the grid cell aspect ratio ( $\Delta z/\Delta x$ ) is less than the local bottom slope. This is called partly shaved cell grid. In shaved cell grid, the regions of steep slopes are represented by increasing the horizontal resolution locally and adjusting the locations of surface nodes in a piecewise linear manner. Designing such a grid for a realistic ocean topography may establish high resolution areas (for a fixed set of vertical levels), which may cause numerical difficulties. Therefore, in regions of gentle slopes both  $z + \sigma$  grids can

accurately resolve the bottom topography.

In this application, strait dynamics and the computational cost dictate us to use z-layer in vertical. In 3D the nodal points are connected to each other in the form of prisms that are further divided into tetrahedrons. This provides high flexibility for representation of complex topography and local mesh refinement.

### 3.3 Mathematical structure

In the Finite Element (FE) formulation, the variables are approximated as sums over a finite set of basis functions. Therefore, in addition to the spatial discretization a key step is the definition of the functional spaces. The functional spaces are decided based on two criteria. First, not every velocity-pressure functional spaces are suitable for the geostrophic balance which is the major dynamic feature in ocean. *Le Roux et al.* (1998) shown that piecewise linear functions should be used for both velocity and the pressure fields (P1-P1 discretization). Second, the piecewise linear basis functions provide effective matrix storage via nodal information. However, increasing nodal numbers introduce overhead to matrix operations.

Spatial discretization of the differential equations in FEOM requires a test function by which the equation is multiplied and integrated for the minimization of a residual problem and a basis function that approximates the unknown variables over the elements. If the test and the basis functions are the same, the method it is called *Galerkin* method. The standard Galerkin method cannot be applied to the ocean directly. There are two primary numerical problems. The first one is related to advection-dominated flows with high cell Reynolds or Peclet numbers. In such cases spurious oscillations on the grid scale could severely degrade solutions. This is also a common problem in finite differences and is solved using upwind advection schemes. In FE this can be solved either by using distinct test and basis functions (Petrov-Galerkin method) or adding stabilization terms into the formulation. The second problem is related to the basis functions for velocity and pressure and should obey the '*LBB*' criteria (*Ladyzhenskaya*, 1969; *Babuška*, 1973; *Brezzi*, 1974). Therefore, strong stabilization is needed to eliminate spurious pressure (surface elevation in hydrostatic case) modes.

In the early version of FEOM, *Galerkin least-squares (GLS, Codina and Soto (1997))* is employed by *Danilov et al. (2004)* to tackle this stabilization problem.

In the current version of FEOM (v1.4), the characteristic based split (CBS) scheme (*Zienkiewicz et al., 1999*) to the momentum and continuity equations provides a better and faster stabilization than GLS (*Wang et al., 2008*). In this projection method velocity and the pressure are decoupled to reduce the cost of solver in the the dynamical part. The LBB condition is circumvented and the advection is stabilized by using time discretization along the characteristics (the characteristic Galerkin, CG, method). Another alternative is the subgrid scale (SGS) formulation which produce similar stabilization compared to the CBS method (*Codina and Zienkiewicz, 2002*).

Tracer equations can be solved similar to momentum advection using the *characteristic Galerkin (CG)* method (*Zienkiewicz and Taylor, 2000*). This method states that before any spatial discretization, temporal discretization is done using Taylor series expansion. The resulting mass-matrix equations can be efficiently solved. Another implemented advection scheme in FEOM uses the explicit flux-corrected transport (FCT) method (*Löhner et al., 1987*), which takes the CG scheme for the high-order component to control sharp fronts in the model and to eliminate the possible overshooting for the sake of numerical stability. Sharp fronts in the model are controlled and possible overshooting is eliminated for the sake of numerical stability. The GLS scheme by *Danilov et al. (2004)* is modified to use Crank-Nicholson time stepping and remains as an alternative.

The finite set of basis functions used for discrete FE formulation in 2D (sea surface elevation) and 3D (velocity and tracers) are denoted by  $N_j$  and  $M_j$ , respectively.  $N_j$  and  $M_j$  are equal to 1 at node  $j$  and go linearly to 0 at neighboring nodes. They are set to zero outside the stencil.  $N$  and  $M$  are the total numbers of 3D and 2D mesh nodes, respectively.

$$\mathbf{u} \simeq \sum_{j=1}^N (u_j, v_j) N_j, \quad C \simeq \sum_{j=1}^N C_j N_j \quad (3.14)$$

$$\eta \simeq \sum_{j=1}^M \eta_j M_j \quad (3.15)$$

The nodal values are approximated to their discrete form via the following vectors:

$$\begin{aligned} \tilde{\mathbf{u}} &= [u_1, \dots, u_j, \dots, u_N, v_1, \dots, v_j, \dots, v_N]^T \\ \tilde{C} &= [C_1, \dots, C_j, \dots, C_N]^T \\ \tilde{\eta} &= [\eta_1, \dots, \eta_j, \dots, \eta_M]^T \end{aligned} \quad (3.16)$$

In above equation, the velocity vector  $\tilde{\mathbf{u}}$  includes both zonal,  $u$ , and meridional,  $v$ , components and has the length of  $2N$ . The tracer field,  $\tilde{C}$ , and sea surface elevation,  $\tilde{\eta}$  are vectors of length  $N$  and  $M$ , respectively. 3D nodes are produced from the surface 2D nodes and they have the following relation:

$$\sum_{j \in J} N_j = M_J, \quad \sum_{j \in J} \frac{\partial N_j}{\partial z} = 0, \quad (3.17)$$

where  $j \in J$  is the sum over basis functions associated with 3D nodes that are derived from the 2D node  $J$ . Equation 3.17 guarantees consistency between the continuity equation and the surface elevation equation (*Danilov et al., 2004; Wang et al., 2008*).

### 3.3.1 Characteristic Galerkin Method

The characteristic Galerkin method is based on an idea to discretize the equations in time first and then to apply the finite element discretization. *Zienkiewicz and Taylor (2000)* described the method starting from a simple advection equation.

$$\partial_t \phi + U \partial_x \phi - Q = 0 \quad (3.18)$$

where  $\phi$  is a tracer field or a velocity component,  $U$  is the one dimensional velocity and  $Q$  is the other terms. If the coordinate system moves with the characteristic velocity,  $U$  then the equation above takes the form

$$\frac{\partial \phi}{\partial t}(x'(t), t) - Q(x') = 0 \quad (3.19)$$

where  $x'$  is the moving coordinate. Advection term disappears and  $Q$  is the term along the characteristics. The time discretization has to be done first as follows:

$$\frac{1}{\Delta t}(Q^{n+1} - Q^n |_{x-\delta}) \approx \theta Q^{n+1} - (1 - \theta)Q^n |_{x-\delta} \quad (3.20)$$

where  $\theta$  is 1 and 0 for fully implicit and explicit forms, respectively. The values in between gives the semiimplicit form. If Taylor expansion is applied to the equation above

$$\phi^n |_{x-\delta} \approx \phi^n - \delta \frac{\partial \phi^n}{\partial x} + \frac{\delta^2}{2} \frac{\partial^2 \phi^n}{\partial x^2} + O(\delta^3) \quad (3.21)$$

$$Q |_{z-\delta} \approx Q^n - \delta \frac{\partial Q^n}{\partial x} + O(\delta^2) \quad (3.22)$$

$\delta = \bar{U} \Delta t$  is the distance traveled by the particle in  $x$  direction and  $\bar{U}$  is the average velocity along the characteristic.  $\bar{U}$  can be approximated in different ways. In the code it is

$$\bar{U} = \frac{U^{n+1} - U^n |_{x-\delta}}{2} \text{ where} \quad (3.23)$$

$$U^n |_{x-\delta} \approx U^n - \Delta t U^n \frac{\partial U^n}{\partial x} + O(\Delta t^2) \quad (3.24)$$

The equation 3.20 takes the form after the necessary fields are substituted

$$\begin{aligned} \frac{\phi^{n+1} - \phi^n}{\Delta t} &= -U^{n+1/2} \frac{\partial \phi^n}{\partial x} + \frac{\Delta t}{2} U^n \frac{\partial U^n}{\partial x} \frac{\partial \phi^n}{\partial x} + \frac{\Delta t}{2} U^{n+1/2} U^{n+1/2} \frac{\partial^2 \phi^n}{\partial x^2} \\ &+ Q^{n+1/2} - \frac{\Delta t}{2} U^{n+1/2} \frac{\partial Q^n}{\partial x} \end{aligned} \quad (3.25)$$



where

$$U^{n+1/2} = \frac{U^{n+1} + U^n}{2} \text{ and } Q^{n+1/2} = \frac{Q^{n+1} + Q^n}{2} \quad (3.26)$$

Further approximation can be done for the explicit form of the  $U$  and  $U^{n+1/2} = U^n + O(\Delta t)$  can be substituted in the second order terms to get

$$\frac{\phi^{n+1} - \phi^n}{\Delta t} = -U^n \frac{\partial \phi^n}{\partial x} + Q^{n+\theta} + \frac{\Delta t}{2} U^n \frac{\partial}{\partial x} [U^n \frac{\partial}{\partial x} \phi^n - Q^{n+\theta}] \quad (3.27)$$

According to the value of the  $\theta$ , different terms, i.e. components of  $Q$ , get different temporal forms.

### 3.3.2 Momentum and vertically integrated continuity

After applying the CG method to the horizontal momentum equation 3.1, the discretized equation takes the form of:

$$\delta(\mathbf{u}^{n+1} - \mathbf{u}^n) + (\mathbf{v} \cdot \nabla_3 \mathbf{u})^n = Q^{n+\gamma} + \frac{\Delta t}{2} \mathbf{v}^n \cdot \nabla_3 [(\mathbf{v} \cdot \nabla_3 \mathbf{u})^n - Q^{n+\gamma}] \quad (3.28)$$

where  $t$  is the time step and  $\delta = 1/\Delta t$ .  $Q$  represents all the terms except for the time derivative and advection components.  $\gamma$  changes the form of the equation as implicit ( $\gamma=1$ ), semi-implicit ( $\gamma=0.5$ ) or explicit ( $\gamma=0$ ). The second order Adams-Bashforth method is used for the Coriolis term at time level  $n+1/2$ . The part of pressure is taken at time level  $n+1/2$  because the density and the viscosity are updated at time  $t$ . The momentum advection is coded using characteristic split method which adds some extra term (upwinding) making the momentum advection part second order in time. The contribution from the sea surface height is treated implicitly and together with barotropic divergence it suppress fast inertia-gravity waves. Fully implicit surface elevation form reduces the equation to first-order accurate in time. One can easily make it second-order with Crank-Nicholson by taking ssh semi-implicit if required without extra overhead.

Substituting all the terms in  $Q^{n+\gamma}$  explicitly yields:

$$\begin{aligned}
\delta(\mathbf{u}^{n+1} - \mathbf{u}^n) + (\mathbf{v} \cdot \nabla_3 \mathbf{u})^n = & \\
& - g \nabla \eta^{n+1} - f \mathbf{k} \times \mathbf{u}^{n+1/2} - \frac{1}{\rho_0} \nabla p^{n+1/2} \\
& + \nabla \cdot A_h \nabla \mathbf{u}^n + \partial_z A_v \partial_z \mathbf{u}^n \\
& + \frac{\Delta t}{2} \mathbf{v}^n \cdot \nabla_3 \cdot [(\mathbf{v} \cdot \nabla_3 \mathbf{u})^n + f \mathbf{k} \times \mathbf{u}^{n+1/2} + \frac{1}{\rho_0} \nabla p^{n+1/2} + g \nabla \eta^n]
\end{aligned} \tag{3.29}$$

The third and higher order derivatives are neglected. The Coriolis, pressure and viscous terms are computed as

$$\mathbf{u}^{n+1/2} = (3/2 + \epsilon) \mathbf{u}^n - (1/2 + \epsilon) \mathbf{u}^{n-1} \tag{3.30}$$

$\epsilon$  is a small constant used for stability in Adams-Bashforth method.

The idea of solving the pair 3.1 and 3.2 is standard projection method and is similar other models working with implicit free surface. First, the prediction step is employed for an auxiliary velocity,  $\mathbf{u}^*$

$$\delta(\mathbf{u}^* - \mathbf{u}^n) + g \theta \nabla \eta^n = \mathbf{R} \tag{3.31}$$

where  $\theta$  is a tunable parameter in a range of 0 and 1.  $\mathbf{R}$  includes all the terms on the rhs of the momentum equation (3.29) except for time derivative and surface pressure. Here, the surface elevation at time level n enters into the equation 3.31. The predicted velocity is corrected by solving

$$\delta(\mathbf{u}^{n+1} - \mathbf{u}^*) + g \nabla (\eta^{n+1} - \theta \eta^n) = 0 \tag{3.32}$$

Subtracting 3.31 from 3.29 results in 3.32. Nevertheless,  $\eta^{n+1}$  is still unknown and surface elevation should be calculated before the correction step since it requires the surface elevation information at time level n+1. The surface elevation is fully implicit

and requires stabilization. The stabilization parameter  $\theta$  determines the strength of stabilization. If  $\theta$  is close to zero, then the stabilization is the strongest and  $\theta = 0$  removes the stabilization terms. The surface elevation equation takes the form

$$\delta(\eta^{n+1} - \eta^n) - \Delta t g \nabla \int \nabla(\eta^{n+1} - \theta \eta^n) dz + \nabla \int \mathbf{u}^* dz = R + P - E \quad (3.33)$$

The procedure is as follows: first, compute auxiliary velocity,  $\mathbf{u}^*$  in equation 3.31 and then get the sea surface elevation  $\eta^{n+1}$  using the equation 3.33. The final step is obtaining the correct velocity,  $\mathbf{u}^{n+1}$  by solving 3.30. The code has free surface representation and  $R + P - E$  is added on the rhs of the vertically integrated continuity equation. If  $R + P - E$  is zero, virtual salt fluxes should be added and the volume has to be conserved.

The vector representing the auxiliary velocity have the form:

$$\begin{aligned} \mathbf{u}^* &\simeq \sum_{j=1}^N (u_j^*, v_j^*) N_j \\ \tilde{\mathbf{u}}^* &= [u_1^*, \dots, u_j^*, \dots, u_N^*, v_1^*, \dots, v_j^*, \dots, v_N^*]^T \end{aligned} \quad (3.34)$$

where the length of the auxiliary velocity vector  $\tilde{\mathbf{u}}$  is  $2N$ . The following part includes solely the discrete representation therefore, overlines in the notation are omitted.

### 3.3.2.1 Matrix form

The standard Galerkin FE procedure is used to solve discretized equations above. The basis functions are substituted in the equations 3.29, 3.31 and 3.30, successively and multiplied by the test functions that are the same of the basis functions in standard Galerkin method and integrated over the surface  $\Gamma_1$ .

The matrix form of the first substitutions is

$$\begin{aligned}
\mathbf{M}_u \Delta \mathbf{u}^* &= -\Delta t (\mathbf{N}(\mathbf{v}^n) \mathbf{u}^n + \mathbf{L} \mathbf{u}^{n+1/2} + \mathbf{C} p^{n+1/2} + \theta g \mathbf{G} \eta^n) \\
&\quad - \Delta t \mathbf{K} \mathbf{u}^n + \Delta t (\mathbf{S} \tau^{n+1} - \mathbf{B}(\mathbf{u}^n) \mathbf{u}^n) \\
&\quad - \frac{\Delta t^2}{2} (\mathbf{N}_s(\mathbf{v}^n) \mathbf{u}^n + \mathbf{L}_s(\mathbf{v}^n) \mathbf{u}^{n+1/2}) \\
&\quad + \mathbf{C}_s(\mathbf{v}^n) p^{n+1/2} + g \mathbf{G}_s(\mathbf{u}^n) \eta^n
\end{aligned} \tag{3.35}$$

where  $\Delta \mathbf{u}^* = \mathbf{u}^* - \mathbf{u}^n$ , and the viscous and stabilization terms have been integrated by parts. The lhs of the equation 3.35 is the time derivative and on the row on the rhs represents the advection, Coriolis force, hydrostatic pressure and surface pressure terms successively. The second row gives the viscous term and boundary integration arising from integrating by parts the viscous contribution. The last two rows are the stabilization contribution after integration by parts. *Wang et al.* (2008) states that the boundary contributions from stabilization terms can be neglected, so as the residual on the boundaries. The resulting matrices will take the shape as follows.

The mass matrix term,  $\mathbf{M}_u$

$$\mathbf{M}_u \equiv \begin{pmatrix} M' & 0 \\ 0 & M' \end{pmatrix} \text{ where } M'_{ij} = \int_{\Omega} N_i N_j d\Omega, \text{ for } 1 \leq i, j \leq N \tag{3.36}$$

The advection term

$$\mathbf{N}(\tilde{\mathbf{v}}) \equiv \begin{pmatrix} N'(\tilde{\mathbf{v}}) & 0 \\ 0 & N'(\tilde{\mathbf{v}}) \end{pmatrix} \text{ where } N'_{ij}(\tilde{\mathbf{v}}) = \int_{\Omega} N_i \tilde{\mathbf{v}} \cdot \nabla_3 N_j d\Omega, \text{ for } 1 \leq i, j \leq N \tag{3.37}$$

The Coriolis term

$$\mathbf{L} \equiv f \begin{pmatrix} 0 & -L' \\ -L' & 0 \end{pmatrix} \text{ where } L' = M' \tag{3.38}$$

The viscous term

$$\mathbf{K} \equiv f \begin{pmatrix} -K' & 0 \\ 0 & -K' \end{pmatrix} \text{ where } K'_{ij} = \int_{\Omega} (A_h \nabla N_i \cdot \nabla N_j + A_v \partial_z N_i \partial_z N_j) d\Omega$$

for  $1 \leq i, j \leq N$  (3.39)

The boundary integral on rigid walls is zero, and on the surface and at the bottom gives terms with matrices  $\mathbf{S}$  and  $\mathbf{B}$  respectively:

$$\mathbf{S} \equiv \begin{pmatrix} S' & 0 \\ 0 & S' \end{pmatrix}, \mathbf{B}(\tilde{\mathbf{u}}) \equiv \begin{pmatrix} B'(\tilde{\mathbf{u}}) & 0 \\ 0 & B'(\tilde{\mathbf{u}}) \end{pmatrix}$$

$$S'_{ij} = \int_{\Gamma_1} N_i M_j d\Gamma_1, B'_{ij}(\tilde{\mathbf{u}}) = \int_{\Gamma_2} C_d |\tilde{\mathbf{u}}| N_i N_j d\Gamma_2, \quad (3.40)$$

where the surface integration is taken on proper boundary surfaces, so only associated matrix entries are non-zero. Note that each component of the surface wind stress has been approximated in a same manner as the surface elevation (equation 3.15) so totally  $\tau$  is of length  $2M$ . The contribution from the surface elevation is  $\gamma g \mathbf{G} \eta^n$ , where

$$\mathbf{G} \equiv f \begin{pmatrix} G^1 \\ G^2 \end{pmatrix} \text{ where } G^q_{ij} = \int_{\Omega} N_i \frac{\partial M_j}{\partial x_q} d\Omega,$$

$$\text{for } 1 \leq i \leq N; 1 \leq j \leq M; q = 1, 2. \quad (3.41)$$

The matrices with subscript  $s$  in the last two rows of 3.35 correspond to terms stabilizing the momentum advection. Their matrix structures are similar to their counterparts in the first row of the rhs, so only their matrix entries are shown here:

$$N'_{s,ij}(\tilde{\mathbf{v}}) = \int_{\Omega} \tilde{\mathbf{v}} \cdot \nabla_3 N_i \tilde{\mathbf{v}} \cdot \nabla_3 N_j d\Omega$$

$$L'_{s,ij}(\tilde{\mathbf{v}}) = \int_{\Omega} \tilde{\mathbf{v}} \cdot \nabla_3 N_i N_j d\Omega \text{ for } 1 \leq i, j \leq N;$$

$$G^q_{s,ij}(\tilde{\mathbf{u}}) = \int_{\Omega} \tilde{\mathbf{u}} \cdot \nabla N_i \frac{\partial M_j}{\partial x_q} d\Omega,$$

$$\text{for } 1 \leq i \leq N; 1 \leq j \leq M; q = 1, 2. \quad (3.42)$$

The discrete form of the second step 3.33 is

$$(\mathbf{M}_\eta + \Delta t^2 \mathbf{H}) \Delta \eta = \Delta t (\mathbf{G}^T \mathbf{u}^* - \Delta t (1 - \theta) \mathbf{H} \eta^n + \mathbf{P} - \mathbf{O}_\eta \mathbf{U}_{OB}^\perp), \quad (3.43)$$

where  $\Delta\eta = \eta^{n+1} - \eta^n$ , and  $P$  denotes the vector of mass sources (river runoff plus precipitation minus evaporation). The last term on the rhs of above equation contains the open boundary contribution, which appears after integrating by parts the divergence terms in 3.33.  $U_{OB}^\perp$  is a vector of length  $M$ , with entries on open boundaries filled with specified vertically integrated normal velocity (positive is out of the domain) and elsewhere zero. The integrals over lateral rigid walls are set to zero thus weakly imposing impermeability. The matrix for the time stepping term is

$$\mathbf{M}_\eta \equiv (M'_\eta), \quad M'_{\eta,ij} = \int_{\Gamma_1} M_i M_j d\Gamma_1, \quad \text{for } 1 \leq i, j \leq M \quad (3.44)$$

The matrix  $\mathbf{H}$  is

$$\mathbf{H} \equiv (H'_{ij}), \quad H'_{ij} = g \int_{\Omega} \nabla M_i \cdot \nabla M_j d\Omega, \quad \text{for } 1 \leq i, j \leq M \quad (3.45)$$

The matrix in the open boundary terms contains the line integral:

$$\mathbf{O}_\eta \equiv (O'_\eta), \quad O'_{\eta,ij} = \int_{S_0} M_i M_j dS_0, \quad \text{for } i, j \text{ on } S_0 \quad (3.46)$$

where matrix entries that are not on open boundaries are filled with zero.

The final matrix form of the correction step 3.31 is

$$\mathbf{M}_u \Delta \mathbf{u} = \mathbf{M}_u \Delta \mathbf{u}^* - \Delta t g \mathbf{G} (\eta^{n+1} - \theta \eta^n), \quad (3.47)$$

where  $\Delta \mathbf{u} = \mathbf{u}^{n+1} - \mathbf{u}^n$ .

### 3.3.3 Vertical velocity

The vertical velocity should be updated after the computation of the horizontal velocity and surface elevation. The vertical velocity  $w$  is diagnosed by known horizontal

velocity and elevation via 3.7 which includes the first order derivative. The first order derivative is difficult for the iterative solvers. Therefore, to facilitate the solvers, a potential term  $\Phi$  is introduced for  $w$  to compute vertical velocity a potential,  $\Phi$  such that  $w = \partial_z \Phi$  should be searched. This procedure is described by *Danilov et al.* (2004).

$$\partial_z \partial_z \Phi = -\nabla \cdot \mathbf{u}_c^{n+1} + (R + P - E)\delta(z), \text{ where } \partial_z \Phi = w \quad (3.48)$$

Now the problem with  $\Phi$  becomes second order and the discrete equation involves symmetric and positive definite matrix which is much better suited to iterative solvers. However, to make the problem well posed, the vertically integrated continuity equation and the continuity equation should be projected on consistent set of test functions. For this reason  $\mathbf{u}_c^{n+1}$  is chosen to compute the divergence in 3.7. Substituting  $\mathbf{u}_c^{n+1}$  into 3.48 leads to

$$\partial_z \partial_z \Phi = \nabla \cdot \mathbf{u}^* + g\Delta t \nabla \cdot \nabla (\eta^{n+1} - \theta\eta^n) + (R + P - E)\delta(z) \quad (3.49)$$

The potential  $\Phi$  is approximated as

$$\Phi \simeq \sum_{j=1}^N \Phi_j N_j \quad (3.50)$$

$$\tilde{\Phi} = [\Phi_1, \dots, \Phi_j, \dots, \Phi_N]^T \quad (3.51)$$

Weighting 3.48 by  $N_j$  and integrating it by parts result in

$$\begin{aligned} \int_{\Omega} \partial_z N_i \partial_z \Phi^{n+1} d\Omega - \int_{\Omega} \nabla N_i \cdot (\mathbf{u}^* - g\Delta t \nabla (\eta^{n+1} - \theta\eta^n)) d\Omega \\ + \frac{1}{\Delta t} \int_{\Gamma_1} N_i (\eta^{n+1} - \eta^n - (R + P - E)\Delta t) d\Gamma_1 \\ + \int_{\Gamma_4} N_i \mathbf{u}_{OB}^\perp d\Gamma_4 \end{aligned} \quad (3.52)$$

The open boundary velocity  $\mathbf{u}_{OB}^\perp$  is simply taken as velocity  $\mathbf{u}^{n+1}$  at open boundary nodes. It carries approximately the same transport through the open boundary as that imposed when solving for elevation.

$$\begin{aligned} \mathbf{M}_\Phi \Phi^{n+1} &= -\mathbf{D}_\Phi \mathbf{u}^* + \mathbf{E}_\Phi (\eta^{n+1} - \theta \eta^n) \\ &+ \mathbf{S}_\Phi (\eta^{n+1} - \eta^n - (R + P - E)\Delta t) + \mathbf{O}_\Phi \mathbf{u}_{OB}^\perp \end{aligned} \quad (3.53)$$

where

$$\mathbf{M}_\Phi \equiv (M'_\Phi), \quad (3.54)$$

$$\begin{aligned} M'_{\Phi,ij} &= \int_{\Omega} \partial_z N_i \partial_z N_j d\Omega, \text{ for } 1 \leq i, j \leq N, \\ \mathbf{D}_\Phi &\equiv (D_{\Phi}^1, D_{\Phi}^2), \end{aligned} \quad (3.55)$$

$$\begin{aligned} D_{\Phi,ij}^q &= \int_{\Omega} \frac{\partial N_i}{\partial x_q} N_j d\Omega, \text{ for } 1 \leq i, j \leq N; q = 1, 2, \\ \mathbf{E}_\Phi &\equiv (E'_\Phi), \end{aligned} \quad (3.56)$$

$$\begin{aligned} E'_{\Phi,ij} &= \int_{\Omega} g \Delta t \nabla N_i \cdot \nabla M_j d\Omega, \text{ for } 1 \leq i \leq N, 1 \leq j \leq M, \\ \mathbf{S}_\Phi &\equiv (S'_\Phi), \end{aligned} \quad (3.57)$$

$$\begin{aligned} E'_{\Phi,ij} &= \frac{1}{\Delta t} \int_{\Gamma_1} N_i M_j d\Gamma_1, \text{ for } i, j \text{ on } \Gamma_1, \\ \mathbf{O}_\Phi &\equiv (O'_\Phi), \end{aligned} \quad (3.58)$$

$$O'_{\Phi,ij} = \int_{\Gamma_4} N_i N_j d\Gamma_4, \text{ for } i, j \text{ on } \Gamma_4. \quad (3.59)$$

The vertical velocity is now perfectly consistent with the sea surface elevation. For the same reason the solvability condition for 3.53, which requires that the sums of its



rhs over nodes aligned vertically be zero, is also satisfied. However, small errors are present up to solver precision. In the absence of open boundaries this procedure is not needed in the limit of high solver tolerance.

### 3.3.4 Biharmonic Viscosity

Both, Laplacian and bi-harmonic momentum friction operators are available in FEOM. There exists no rule of thumb of choice for either formulation. If the model is run at the eddy resolving resolution the Laplacian viscosity is generally too damping and strongly reduces the eddy variances of all fields compared to observations. Although only Laplacian viscosity can directly be modeled with linear basis functions the implementation of biharmonic viscosity is also possible via introducing additional variables. One writes

$$\mathbf{a} = \delta \mathbf{u} \quad (3.60)$$

$$\mathbf{b} = -\nabla A_{hb} \nabla \mathbf{a} \quad (3.61)$$

where  $b$  is the biharmonic viscosity contribution to the rhs of the momentum equation and  $A_{hb}$  is the biharmonic viscosity coefficient. Projecting 3.60 on linear functions, integrating by parts, and setting surface integrals to zero lead to  $M\mathbf{a} = L\mathbf{u}$ , where  $M$  and  $L$  denote mass matrix and the matrix of the Laplacian operator. Lumping is used to solve this equation in an efficient way:  $\mathbf{a} = ML^{-1}L\mathbf{u}$ . With nodal values of  $\mathbf{a}$  known, the rest of computations proceed in the same way as computing Laplacian viscosity. *Griffies and Hallberg (2000)* emphasizes the scale-selectivity of the bi-harmonic operator for its less dissipation on the resolved scale. Horizontal viscosity values can be provided as a constant. However, this leads to numerical problems not only for the models with unstructured grid but also for regular grid based models that have changed grid size in the meridional direction. It is now a common practice in ocean modeling to scale the horizontal viscosity value based on the grid size. In FEOM, a prescribed bi-harmonic viscosity value is scaled based on the grid size cubed. Another alternative is to use a flow dependent Smagorinsky scheme that is

based on the horizontal deformation rate and the grid spacing squared. The simulation with Smagorinsky viscosity produces smooth constant density surfaces along the thalweg of the Bosphorus (not shown here).

### 3.3.5 Boundary Conditions on Rigid Walls

When no-slip boundary conditions are employed, the two components of the horizontal velocity on rigid walls are set to zero and no extra efforts are required. For free-slip boundary conditions, only the velocity component normal to the boundaries and the tangential component of the viscous stress should be set to zero. If boundaries are not aligned with the coordinate system (which is commonly the case on unstructured meshes) applying free-slip boundary conditions requires to transform the  $x$  and  $y$  (zonal and meridional) momentum equations as well as velocities to the local tangential and normal directions.

Let  $\mathbf{M}\mathbf{u} = \mathbf{R}$  be the fully discrete momentum equation to be solved. To transform this equation to the tangential and normal equation on rigid walls, pre-multiplying simply the mass matrix and the rhs vector with a rotation matrix  $\mathbf{R}$  and then post-multiply the mass matrix by its transpose  $\mathbf{R}^T$ :

$$(\mathbf{R}\mathbf{M}\mathbf{R}^T)\tilde{\mathbf{u}} = \mathbf{R}\mathbf{R} \quad (3.62)$$

where  $\tilde{\mathbf{u}} \equiv (\mathbf{u}_t, \mathbf{u}_n)^T$  coincide with the tangential and normal directions,  $\mathbf{R}$  has a size of  $2N \times 2N$ . After taking this transformation the no-normal-flow boundary condition can easily be applied. Once  $\tilde{\mathbf{u}}$  is solved, it can be converted to velocity along  $x$  and  $y$  directions for each boundary node  $i$  by

$$\begin{pmatrix} u_x^i \\ u_y^i \end{pmatrix} = \begin{pmatrix} -n_y^i & n_x^i \\ n_x^i & n_y^i \end{pmatrix} \begin{pmatrix} u_t^i \\ u_n^i \end{pmatrix} \quad (3.63)$$

where  $\mathbf{n}^i \equiv (n_x^i, n_y^i)$  is the outward pointing unit normal vector at node  $i$ . The  $2 \times 2$  orthogonal nodal rotation matrix for node  $i$  enters the whole rotation matrix  $\mathbf{R}$  and

$R^T$  in the following way:

$$R_{ii} = -n_y^i, \quad R_{i,i+N} = n_x^i, \quad R_{i+N,i} = n_x^i, \quad R_{i+N,i+N} = n_y^i \quad (3.64)$$

Except for rows associated with boundary nodes there is only a unity on the diagonal of matrix  $R$ . In practice matrix  $R$  is not assembled, instead rotations are directly applied when assembling stiffness matrices and the rhs.

The mass consistent normal vector can be calculated by

$$\mathbf{n}^i = \frac{1}{n^i} \int_{\Gamma_1} \Delta M_i d\Gamma_1, \quad \text{where } n^i = \left| \int_{\Gamma_1} \Delta M_i d\Gamma_1 \right| \quad (3.65)$$

The integration is performed on the surface mesh because only 'vertical' boundaries are treated as rigid walls.

### 3.3.6 Temperature and salinity

FEOM is a free-surface model with the total volume in its domain conserved (*Danilov et al.*, 2004). Similarly, the tracer budget has also to be conserved. Where there is a freshwater flux through the surface boundary ( $E - P - R$ ), there is a need for correction using a virtual salt flux. This salinity flux can be prescribed as a reference mean salinity. In this case total salinity in the domain is conserved implicitly through the conservation of the total volume. The effect would then only be on the local salinity values. If the difference between the reference value and the local salinity is too big, then the model can either produce incorrect results or blow up. Another way is to use the local salinity values as reference. In this case the salinity is not conserved automatically and a correction over the whole domain is necessary. This has an effect on longer time scales (*Wang et al.*, 2014).

One option is to solve tracer evolution equation 3.10 fully explicitly with the CG method. According to this method, the advective term is estimated by an upwinding term on the rhs of tracer equation. The contribution from diffusion is computed with the first order. The semi-discrete equation is

$$\frac{\Delta C}{\Delta t} = -(\mathbf{v} \cdot \nabla_3 C)^n + \nabla \cdot K_h \nabla C^n + \partial_z K_v \partial_z C^n + \frac{\Delta t}{2} \mathbf{v}^n \cdot \nabla_3 (\mathbf{v} \cdot \nabla_3 C)^n \quad (3.66)$$

where  $\Delta C = C^{n+1} - C^n$ . Using the approximation 3.14 the matrix form of 3.66 is given by

$$\mathbf{M}' \Delta C = -\Delta t (\mathbf{N}' C^n + \mathbf{K}' C^n) - \frac{\Delta t^2}{2} \mathbf{N}'_s C^n + \Delta t \mathbf{S}' q \quad (3.67)$$

where  $q$  is flux of tracers on the surface via boundary condition 3.12. The flux is approximated here as  $\sum q_j M_j$ . In oceanographic applications the flux  $q_j$  is usually a combination of climatological flux and a term that restores surface temperature and salinity to climatological values. The entries to the matrices on the rhs of 3.67 are the same as defined before for the momentum equation, except that the viscosity should be replaced with diffusivity in the diffusion term.

In practice it turns out that the CG method is very sensitive to the quality of the mesh and is very demanding in terms of stability. As an alternative to it one can use Crank–Nicolson method with GLS Stabilization *Danilov et al. (2004)* which makes the code much slower. The flux corrected transport (FCT) scheme based on explicit time stepping is desirable by preserving monotonicity to eliminate overshoots in the computation. The classical FCT scheme following *Löhner et al. (1987)* is adopted in the current model which works well for transient problems. It uses the CG method as the high-order component. It has one tunable parameter which defines level of dissipation of the low-order scheme (gamma). It should be between 0 and 1, and is not expected to influence the solution too much provided it is sufficient for monotonicity. Tests are generally advised because the performance is problem dependent. The tests of the three advection schemes of FEOM are given in the work of *Wang et al. (2008)*.

The FCT and GLS schemes use similar CPU time, about 2 to 3 times that required by the CG scheme. The GLS scheme is semiimplicit. It allows larger time steps and is less demanding on strongly variable meshes. A choice should be made considering accuracy and efficiency. When implicit vertical diffusivity or large time steps are required, the GLS scheme is a good choice otherwise FCT provide better monotonicity

conditions (*Wang et al.*, 2008).

The implementation of the FCT scheme is given below.

- Solve high order scheme, equation 3.67
- Perform mass lumping to transform high order scheme into a low order non oscillatory scheme
- Compute anti-diffusive flux
- Limit anti-diffusive flux
- Add limited anti-diffusive flux into the low order solution for the updated solution

The FCT procedure starts with the equation 3.67. If the rhs of the equation is denoted by 3.67 as  $\mathbf{R}$  then

$$\mathbf{M}\Delta C = \mathbf{R}, \quad (3.68)$$

The high order solution is obtain by solving 3.68 as

$$\mathbf{M}_C\Delta C^H = \mathbf{R}, \quad (3.69)$$

where  $\Delta C^H$  is the increment of tracer. The low order solution is

$$\mathbf{M}_L\Delta C^L = \mathbf{R} + \epsilon(\mathbf{M}_C - \mathbf{M}_L)C^n, \quad (3.70)$$

where  $\mathbf{M}_L$  is the lumped matrix and  $\epsilon$  is a tuning parameter controlling the amount of added diffusion on the right hand side of the equation 3.67. Rewriting the equation 3.69 produces

$$\mathbf{M}_L\Delta C^H = \mathbf{R} + (\mathbf{M}_L - \mathbf{M}_C)\Delta C^H, \quad (3.71)$$

Subtracting 3.70 from 3.71 will end up the difference between the two solutions.

$$\Delta C^H - \Delta C^L = \mathbf{M}_L^{-1}(\mathbf{M}_L - \mathbf{M}_C)(\Delta C^H + \epsilon C^m). \quad (3.72)$$

Anti-diffusive flux from element,  $e$  to its node  $i$  is

$$F_{e,i} = (\mathbf{M}_L^{-1})_i \sum_j (\mathbf{M}_L - \mathbf{M}_C)_{e,ij} (\Delta C^H + \epsilon C^m)_j, \quad (3.73)$$

where  $i$  and  $j$  are the local indices of nodes of element  $e$ .

The calculation of the limiting factors,  $\alpha_e$  is explained by *Löhner et al.* (1987) in detail. The final solution at time level  $n+1$  is

$$C_i^{m+1} = C_i^m + \sum_e \alpha_e F_{e,i}, \quad (3.74)$$

where  $i$  is the node and  $\alpha_e$  is the limiting factor.

## CHAPTER 4

### MODEL SIMULATIONS

The TSS model domain extends from 22.5 °E to 33 °E in zonal direction and 38.7 °N to 43 °N in meridional direction. The maximum horizontal mesh resolution in the Bosphorus and Dardanelles Straits is  $\sim 65$  m and  $\sim 150$  m, respectively and the minimum resolution in the Marmara Sea is set to  $\sim 1.6$  km. This choice of resolution ensures 8 elements across the contraction in the Bosphorus and 7 elements across the Nara Passage in the Dardanelles. In the Aegean and Black Seas, a resolution of  $\sim 5$  km is used except for the exit and shelf areas which are better resolved (Figure 4.1, top). The model uses 110 z-levels. Strong stratification and steep continental shelf in this implementation demands high vertical resolution in order to resolve the nonlinear hydraulic transitions, the stratified turbulent exchange flows between the upper and lower layers in the straits as well as to prevent excessive pycnocline erosion in the Marmara Sea. The minimum vertical grid spacing is set to 1 m within the first 50 m. The maximum layer thickness is not greater than 65 m in the deeper part (Figure 4.1, bottom). The time step has to be adjusted according to the minimum horizontal mesh resolution and is set to 10 s.

#### 4.1 Parameterization of subgrid-scale processes

The biharmonic operator is preferred for the momentum friction due to its the scale-selectivity that results in lesser dissipation on the resolved spatial scale (*Griffies and Hallberg, 2000*). Horizontal viscosity coefficients are scaled based on the grid size cubed. Laplacian operator is the only available selection for the tracers. Flow depen-

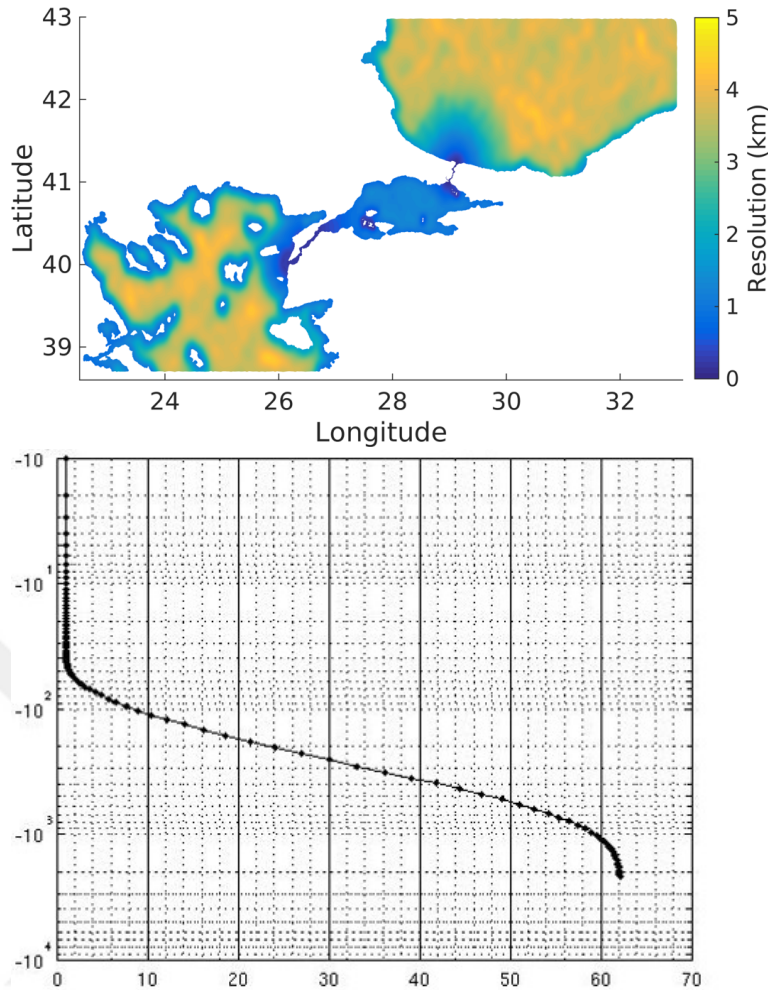


Figure 4.1: Top: Horizontal resolution of the surface mesh (in km). Bottom: Vertical resolution and depth relation of the FEOM mesh. The horizontal axis depicts the vertical layer thickness and the vertical axis shows the depth in m in logarithmic scale.

dent Smagorinsky scheme (which is based on the horizontal deformation rate and the grid spacing squared) is another available option in FEOM. Nevertheless, it is not used since the simulated constant density surfaces along the thalweg of the Bosphorus are unrealistically smooth (not shown here). Horizontal eddy viscosity is parameterized by a biharmonic operator with a coefficient of  $2.7 \cdot 10^{13} \text{ m}^4/\text{s}$  scaled with the element size cubed while horizontal eddy diffusivity is parameterized by a Laplacian operator with a coefficient of  $2000 \text{ m}^2/\text{s}$  scaled with the element size according to *Griffies and Hallberg (2000)*. These values are selected based on the convergence study for second order finite difference Laplacian diffusion by *Wallcraft et al. (2005)*. Biharmonic



operator is preferred since it involves scale selective filtering suppressing finer scales. Laplacian is the only available scheme in FEOM for the eddy diffusion. Boxes are selected for different parts of the TSS and the typical value for harmonic diffusivity of the Bosphorus, Dardanelles and Marmara Sea are calculated to be on the order of 40, 150 and 600 cm<sup>2</sup>/s, respectively (not shown here).

Thermohaline stratification in the TSS depends on vertical diffusion and convection. Convection is treated in a traditional manner as convective adjustment. However, the mixing scheme and the related constants should be selected carefully. In the TSS, the thickness of the upper layer is around 25 m due to the strong halocline in the system. Moreover, the TSS exhibits a wide range of temperature and salinity values that result in strong stratification in the vertical. In an ocean model, the degradation of the stratification from above and below the interface can be very fast if the vertical mixing is constant. Moreover, recent observations show that there is evidence that waters belonging to the Cold Intermediate Layer (CIL) are advected from the Black Sea into the Marmara Sea through the Bosphorus strait (see Figure 2.10). The property of the CIL is protected by seasonal surface heat and water fluxes from above and the salinity gradient from below. This highlights the importance of the decision of the vertical mixing scheme which is a function of the stability of the water column.

Vertical mixing is parameterized with the *Pacanowski and Philander* (1981) scheme, with a background vertical diffusion of 10<sup>-6</sup> m<sup>2</sup>/s for momentum and 10<sup>-5</sup> m<sup>2</sup>/s for tracers and the maximum value set to 0.005 m<sup>2</sup>/s. The vertical diffusion and viscosity are computed as elementwise constant values. The Richardson number dependent factor is first computed and stored, and then used for both diffusion and viscosity. The neutral physics is treated with the neutral diffusion based on the small slope approximation (*Griffies et al.*, 1998) as commonly used in z coordinate models. The diffusivity tensor is used in conjunction with tapering functions, and different tapering schemes discussed by *Griffies* (2004) are supported in the model.

The vertical momentum diffusion coefficient,  $A_v$ , and the vertical tracer diffusion

coefficient,  $K_v$ , are expressed as:

$$A_v = \frac{v_0}{(1 + \alpha \cdot R_i)^n} + A_{v0}, \quad (4.1)$$

$$K_v = \frac{A_v}{1 + \alpha \cdot R_i} + K_{v0}, \quad (4.2)$$

where  $v_0$ ,  $\alpha$  and  $n$  are adjustable parameters set to  $5 \cdot 10^{-3} \text{ m}^2\text{s}^{-1}$ , 10 and 2, respectively.  $A_{v0}$  and  $K_{v0}$  stand for the background vertical diffusion for momentum and tracers, respectively, and are set to  $10^{-5} \text{ m}^2\text{s}^{-1}$  and  $10^{-6} \text{ m}^2\text{s}^{-1}$ . The above formulas depend on the Richardson number  $R_i$ , which expresses the ratio of potential to kinetic energy:

$$R_i = \frac{N^2}{(\partial_z u)^2 + (\partial_z v)^2}, \quad (4.3)$$

with  $N$  being the buoyancy frequency. The constants in the formulation are adapted such that vertical exchange of heat and salt through the interface is limited and the stratification along the TSS is maintained without large dissipation during the time span of the simulation.

## 4.2 Initial and Boundary Conditions

The model is initialized with temperature and salinity data collected during the SESAME Project<sup>1</sup> in October 2008 (Table 4.1). A deep CTD cast is selected from each basin, namely, from the Mediterranean, the Marmara and the Black Seas (Figure 4.2). The vertical profiles of temperature and salinity from those stations are assigned the respective reservoirs (Figure 4.3). These profiles are separated from each other by a sharp vertical barrier close to the mid-straits, the so-called *Lock-exchange experiment (LE)*. In the Marmara Sea, a temperature minimum is evident located between the warm layers of the surface and the Aegean Sea originated deep water. In the Black Sea, the vertical temperature structure is qualitatively similar. The temperature minimum is located near 40 m depth in the Black Sea whereas it is close to 25 m in the Marmara Sea. The Aegean Sea on the other hand shows a steady increase in temperature. The salinity profiles in Figure 4.2 depict that the surface mixed layer in the Aegean Sea is confined to the first 5-6 m. In the Marmara Sea, the halocline is sharper and the position is closer to the surface due to freshwater intrusion from

---

<sup>1</sup> Southern European Seas: Assessing and Modeling Ecosystem changes

the Bosphorus. Note that it can be easily deduced from the salinity and the potential density profiles in Figure 4.2 that potential density is controlled by salinity.

Table 4.1: Summary of the CTD stations selected for the lock-exchange experiment (see Figure 4.1). AS, MS and BS stand for Aegean Sea, Marmara Sea and Black Sea, respectively.

Name	Latitude	Longitude	Maximum Sampling Depth (m)	Total Station Depth (m)
AS	40°02.996'	26°04.831'	67	72
MS	40°46.919'	28°59.971'	1191	1219
BS	41°36.033'	29°31.519'	1203	1271

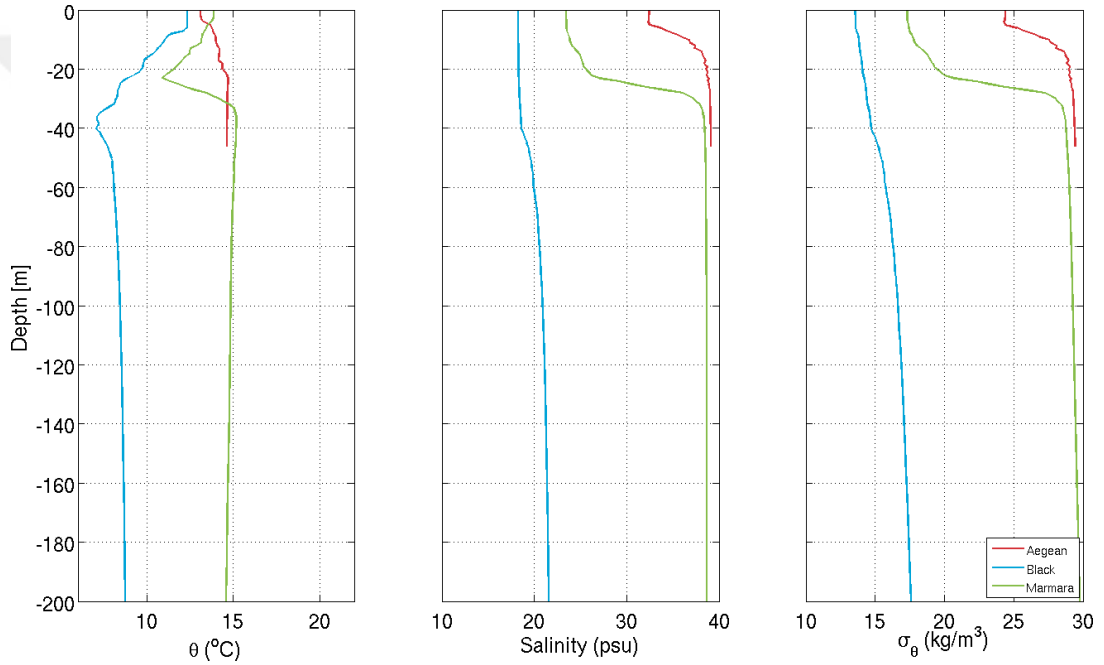


Figure 4.2: Vertical profiles of potential temperature (left), salinity (middle) and potential density (right) representative for the Aegean Sea (red), Black Sea (blue) and Marmara Sea (green) used for lock exchange initial conditions.

The results from the lock-exchange experiment (Gurses et al. submitted., 2015) provide the initial condition for the hindcast experiments. The hindcast simulations are initialized with temperature and salinity fields of the last day (93<sup>th</sup>) of the lock-exchange simulation. Therefore, the geostrophically adjusted initial density distribution in the TSS is obtained without any initial shock. The initial velocity is set to zero. The ocean boundaries are closed, i.e. velocities set to zero at the boundary.

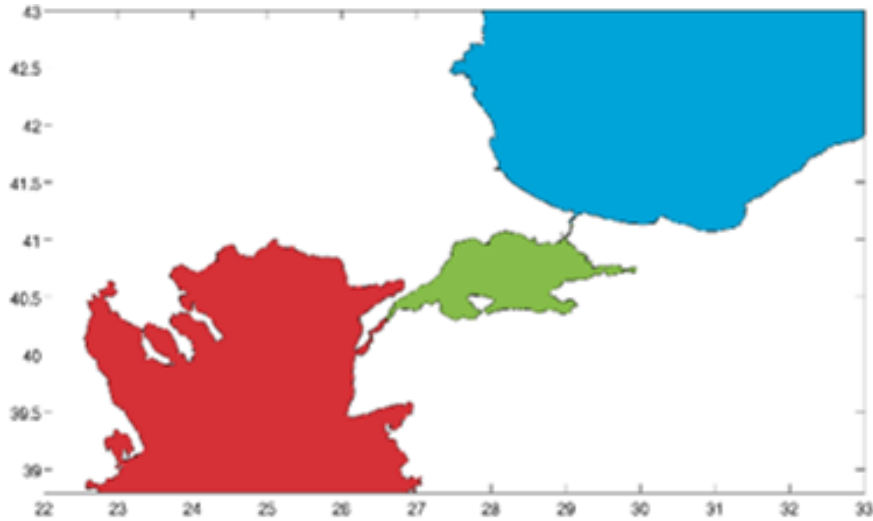


Figure 4.3: Assignment of the profiles depicted in Figure 4.2 to the respective basins, i.e. the Aegean Sea (red), Black Sea (blue) and Marmara Sea (green).

No-slip boundary conditions is applied along the coast implying viscous friction.

The analysis of the simulations and comparison with observations is handled in steps. First, the results of an idealized simulation is presented, the lock-exchange experiment described in the following sections (namely configuration 'BASIC'). The model is run without any atmospheric forcing (wind speed, water and heat fluxes on the surface are set to zero). In this first case, net fluxes originating from the Black Sea as a result of its water budget are also excluded in the simulation.

The model sensitivity to horizontal and vertical mesh resolution is investigated in this work. Tests on sensitivity to mixing coefficients and turbulent schemes were also carried out and an optimum of the various choices was used resulting in model behavior that best mimicked some observed flows. Other crucially important dynamical tests on strait dynamics such as sensitivity to geometric features, initial conditions and other parameterizations were extensively performed by *Sözer* (2013) in a stand-alone model of the Bosphorus dynamics.

In later sections, the model setting was generalized to include atmospheric forcing and the Black Sea net flux cases, and analyzed for the changes. Therefore two additional experiments are conducted, the first one (BBExc) including the atmospheric forcing but ignoring net mass fluxes on top of the BASIC case, and the second one (BBInc)

including Black Sea net water fluxes together with the atmospheric effects.

#### 4.2.1 Model setup with Atmospheric forcing

The surface atmospheric data which drives the system are taken from ECMWF at 6 hourly temporal and  $0.125^\circ$  spatial resolution from the year 2008.

#### 4.2.2 Wind Field

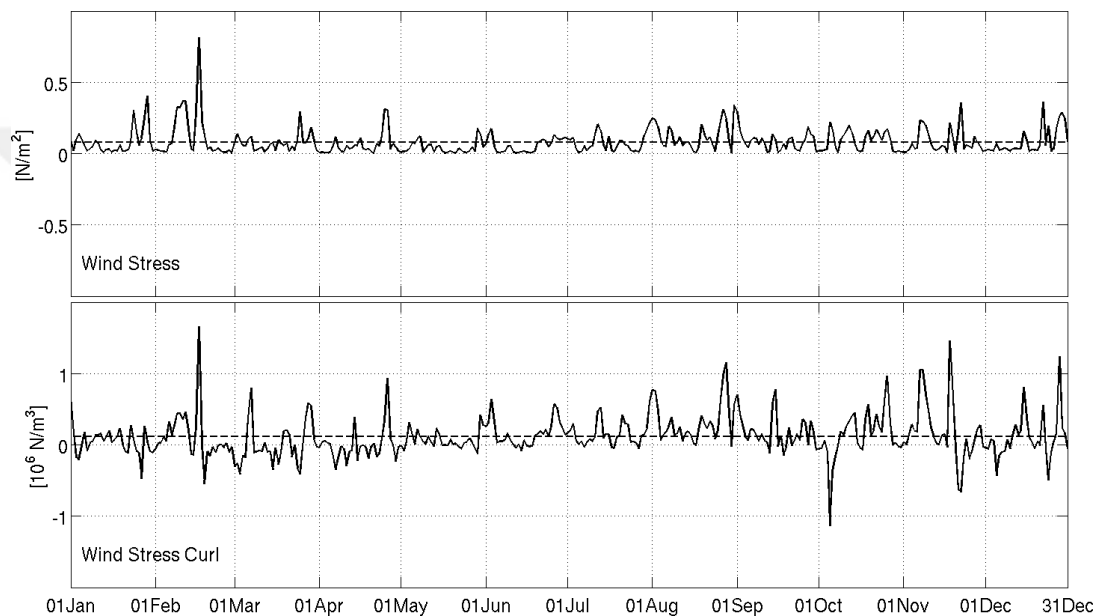


Figure 4.4: Time series of the wind stress (top panel) and wind stress curl (bottom panel) averaged over the TSS region.

The time series of wind stress and wind stress curl shows that there are 3-5 days lasting storm events passing over the TSS region (Figure 4.4). The storms tend to be more intense in the spring and in the autumn months. The strongest event is observed at the end of February 2008 and the weakest period is in May. Although the wind stress is not energetic in November, the curl is very big with its sign changed. The curl is mostly positive throughout the year revealing that the wind forcing function favors a mean anticyclonic flow pathway.

The surface distribution of the wind stress in April and October 2008 displays that the zonal component is stronger than the meridional one (Figure 4.5). The region of the

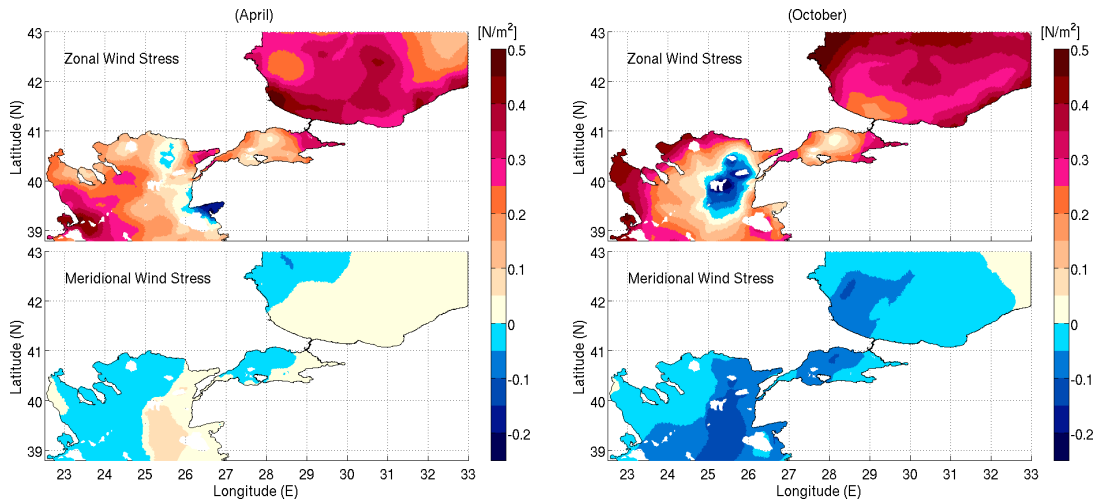


Figure 4.5: Spatial distribution of the wind stress of the ECMWF atmospheric data averaged over April 2008 (left) and over October 2008 (right) in the TSS domain. Wind stress is split into its zonal and meridional components.

negative zonal wind stress is distinctive and confined along the coastal bays (April 2008) and in the vicinity of the islands in the Aegean Sea. The values are lower in the mid-Marmara Sea than in the coastal zones. The regional meridional wind stress split the domain diagonally into positive (northern) and negative (southern) parts in April 2008. It is negative almost all over the basin in October 2008.

### 4.2.3 Surface Heat Flux

Surface heat fluxes, surface salinity fluxes and the wind stresses enter into general ocean circulation models as surface boundary conditions. Accurate formulation and estimation of these fluxes is important for ocean and atmosphere studies. Direct measurement of heat fluxes is not feasible because of lacking accuracy and high costs. Hence, fluxes are calculated based on theoretical and empirical formulas using the parameters that are easy to measure. Particularly, the surface heat budget is estimated from available atmospheric and oceanic data. An error in heat flux calculation leads to biases in SST (*Rosati and Miyakoda, 1988*). Hence, a complete and accurate treatment of heat flux is a necessity. Surface fluxes are computed internally in the model by bulk formulae. The following parts describe the surface heat flux parametrization used in this FEOM implementation. The method is based on the work of *Pettenuzzo*

*et al.* (2010) and extensively tested and utilized by the Mediterranean Forecasting System.

The dominant surface heat fluxes are the shortwave radiation flux  $Q_s$ , the longwave radiation flux  $Q_l$ , the sensible heat flux  $Q_{sens}$  and the latent heat flux of evaporation  $Q_{lat}$ .  $Q_s$  and  $Q_l$  fluxes comprise the radiative part,  $Q_{sens}$  and  $Q_{lat}$  fluxes contribute the turbulent part. Fluxes are positive (upward) if the ocean gains energy. The net surface heat flux is the sum of the radiative and turbulent fluxes:

$$Q_{Net} = Q_s + Q_l + Q_{sens} + Q_{lat} \quad (4.4)$$

In the following paragraphs, each term will be explained.

### **Solar Radiation**

Direct solar radiation and diffusion from the atmosphere reaching the ocean surface is variable and a dominating component of the net heat flux (*Pettenuzzo et al.* (2010), Figures 8a and 8e). Direct solar radiation (insolation) under a clear sky is calculated using the formula by *Rosati and Miyakoda* (1988), which was modified by *Reed* (1977) to account for a cloud cover. Albedo is taken from *Payne* (1972). It depends on sky conditions (namely reflectivity and transmittance).

The radiation at the top of the atmosphere ( $Q_o$ ) is computed as follows:

$$Q_o = \frac{J_o}{a^2} \cdot \cos z \cdot D_f(\phi, \lambda), \quad (4.5)$$

where  $J_o$  is the solar constant,  $a$  is the radius of earth,  $z$  is the zenith angle,  $D_f$  is set as fraction of daylight which is longitude and latitude dependent.  $\cos z$  is a function of the sun declination angle ( $\delta$ ) and the sun's hour angle ( $h$ ).  $\cos z$  is calculated as

$$\cos z = \sin(\phi) \cdot \sin(\delta) + \cos(\phi) \cdot \cos(\delta) \cdot \cos(h). \quad (4.6)$$

The attenuated direct solar radiation on the ocean surface,  $Q_{dir}$ , is calculated as

$$Q_{dir} = Q_o \cdot \tau^{secz} \quad (4.7)$$

where  $\tau$  is the atmospheric transmission coefficient.  $Q_{diff}$  stands for the diffused sky radiation where half of it is scattered back to space:

$$Q_{diff} = \frac{(1 - A_o)Q_o - Q_{dir}}{2}, \quad (4.8)$$

where  $A_o$  is the water vapor and ozone absorption.  $Q_{tot}$  is the total radiation from the top of the atmosphere, a combination of the attenuated direct solar radiation on the ocean surface and the diffused sky radiation:

$$Q_{tot} = Q_{dir} + Q_{diff}. \quad (4.9)$$

Following *Reed* (1977), net insolation reaching the ocean surface is modified as:

$$Q_{sd} = Q_{tot}(1 - 0.62 \cdot C + 0.0019 \cdot \beta) \text{ if } C \geq 0.3 \quad (4.10)$$

where  $C$  is the cloud cover.  $\beta$ , a function of time, is the noon solar altitude in degrees (*Rosati and Miyakoda*, 1988):

$$\beta = \sin(\phi) \cdot \sin[23.45 \sin(t - 81)] + \cos(\phi) \cdot \cos[23.45 \sin(t - 81)] \quad (4.11)$$

where  $t$  is the Julian day. The shortwave radiation flux can then be calculated as

$$Q_s = Q_{sd}(1 - \alpha) \quad (4.12)$$

where  $\alpha$  is the space dependent albedo (*Payne*, 1972).

### Net Longwave Radiation

Acting as an approximate blackbody radiator, the sea surface emits radiation back to the atmosphere under clear skies. It is assumed to occur at the surface within a layer of water of negligible thickness. Following *Bignami et al.* (1995) the following formulation is used for net and downward longwave radiation  $Q_l$  and  $Q_{ld}$ , respectively:

$$Q_l = -\epsilon \cdot \sigma \cdot T_s^4 + Q_{ld} \quad (4.13)$$

$$Q_{ld} = \epsilon \cdot \sigma \cdot T_a^4 + (0.653 + 0.00535 \cdot ea)(1 + 0.1762 \cdot C^2) \quad (4.14)$$

where  $\epsilon$  is the emissivity of the ocean,  $\sigma$  is the Stefan-Boltzmann constant,  $C$  is the cloud fraction,  $ea$  is the atmospheric vapor pressure and  $T_a$  and  $T_s$  are the air and sea surface temperature in Kelvin, respectively. A way to calculate the saturated vapor pressure,  $ea$ , is to use a polynomial of 6<sup>th</sup> order introduced by *Lowe* (1977).



## Sensible and Latent Heat Fluxes

The turbulent part of the air-sea exchange for heat fluxes is based on coefficients from *Kondo (1975)*.

$$Q_{sens} = -\rho_a \cdot C_p \cdot C_h \cdot |V| \cdot (T_s - T_a) \quad (4.15)$$

$$Q_{lat} = -\rho_a \cdot L_e \cdot C_e \cdot |V| \cdot (q_s - q_a) \quad (4.16)$$

where  $\rho_a$  is the air density. are , respectively. In the formula above,  $C_e$ ,  $C_h$ ,  $C_p$ ,  $q_a$ ,  $q_s$ ,  $L_e$ ,  $V$  denote turbulent exchange coefficient for latent heat flux, transfer coefficient for the sensible heat flux, the specific heat capacity of water, saturated specific humidity, artificial saturated specific humidity for sea surface temperature, latent heat of vaporization and wind speed, respectively.

## Surface heat flux over the Marmara Sea

Longwave radiation, which depends on the sea surface and air temperature.

Time series of the components of the surface heat flux computed according to the above described formulation by *Petenuzzo et al. (2010)* averaged over the Marmara Sea is shown in Figure 4.6. The red curve depicts the shortwave radiation entering the Marmara Sea. The values are, as expected, low in the winter months and high in the summer months. The maximum value is reached in June. Note the 33% reduction in insolation earlier in the month, due to the cloud cover over the region. Longwave radiation (blue) depends on the sea surface and air temperature. The difference between them are lower than the ones in summer months. The latent heat flux (brown curve) is negative during the entire period, and particularly low during the summer months. The sensible heat flux (green curve) is the smallest component in the total heat flux. However it can reach up to  $-150 \text{ W/m}^2$  when the sea surface temperature is much warmer than the surrounding air temperature, particularly in the winter months. Turbulent terms of the heat budget reach their peak values during passage of strong storms. The net surface heat flux into the Marmara Sea is positive between the mid-February and mid-September when the shortwave radiation exceeds the other terms and the Marmara Sea warms up from the surface. It is modulated directly by the cloud cover.

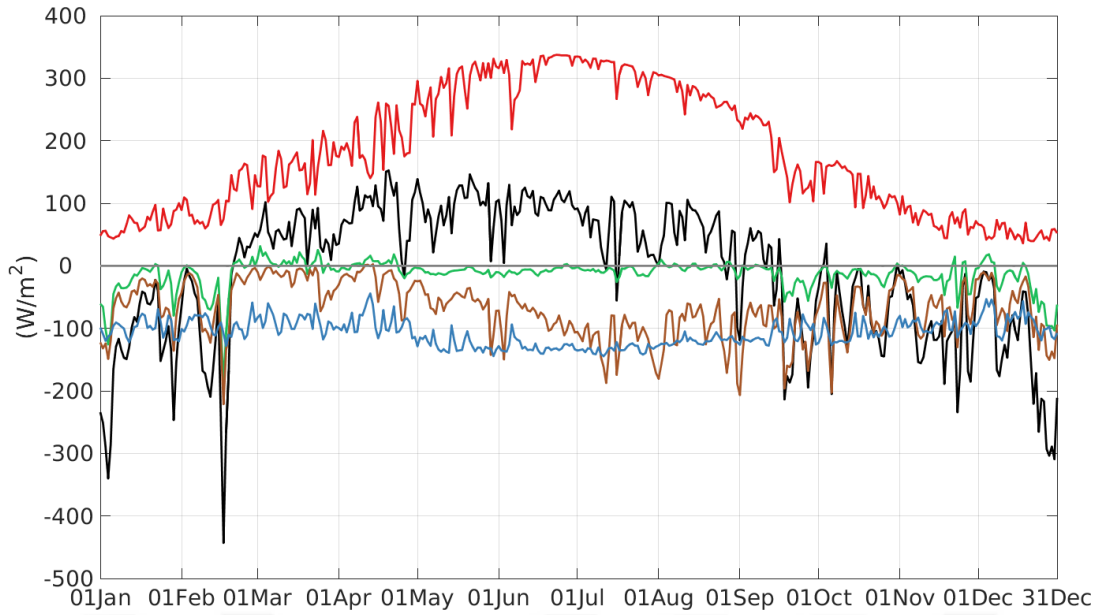


Figure 4.6: Time series of the net surface heat flux and its components computed according to the formulation by *Pettenuzzo et al.* (2010) averaged over the Marmara Sea.  $Q_{net}$ ,  $Q_s$ ,  $Q_b$ ,  $Q_e$  and  $Q_h$  represent net heat flux (black), shortwave (red), longwave (blue), latent heat (brown) and sensible heat (green) fluxes, respectively.

#### 4.2.4 Correction of atmospheric forcing fields against land contamination

High resolution forcing data is often not readily available for small inland seas. Applications with rugged coastlines like ours are prone to information from the land points during the spatial interpolation onto the nodal points. This contamination problem can be overcome by preferentially selecting sea points over the land points (so called sea over land algorithm) in the interpolation. The procedure described by *Kara et al.* (2007). The performance of this 'creeping algorithm' has been tested for selected instantaneous data sets with pronounced gradients between the warmer land and colder sea air masses. The performance of algorithm is evaluated using ECMWF  $0.5^\circ$  resolution temperature fields at 2 m above the surface for an arbitrary day first in the Mediterranean Sea and then in the TSS.

The original ECMWF 2 m air temperature field over the Marmara Sea is shown in Figure 4.7 (top left panel). This snapshot depicts a strong gradient between the colder land and warmer sea air masses. As a first step, land points are set to *NaN* via land-sea mask multiplication. Thereafter, eight translated temperature fields are produced

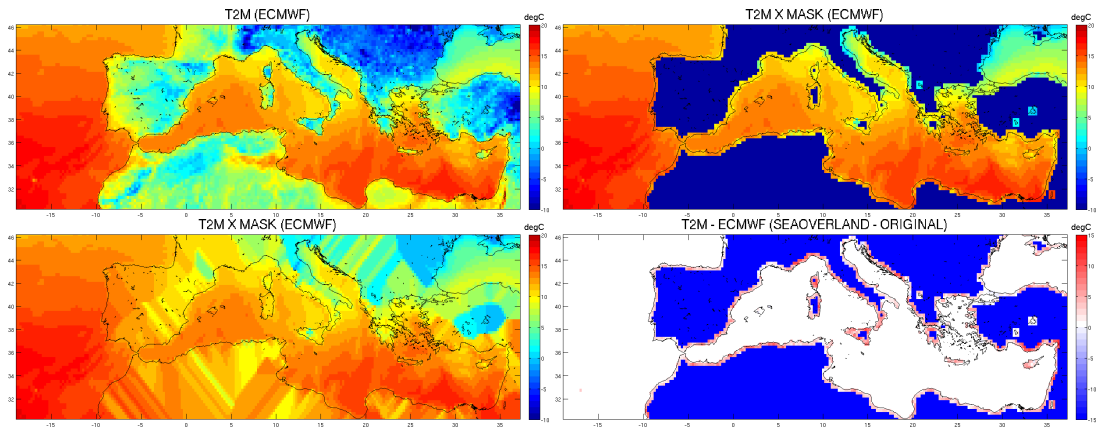


Figure 4.7: ECMWF 2 m air temperature field over the Mediterranean Sea before the creeping algorithm (top left), after the first iteration (top right), after 30 iterations (bottom left) and the difference prior and post creeping algorithm (bottom right).

by translating the original field in adjacent nodal directions (Figure 4.8), e.g. east, north etc. Consequently, each node has a value from its adjacent node as a result of translation. These fields are then summed and normalized. In this operation sea points are excluded. Therefore, the first set of extrapolated sea points along the coastline over the land are calculated (Figure 4.7, top right panel).

Using an iterative procedure to fill the land points, it is found that 30 iterations are sufficient for smooth coastal data, effectively removing cold biases up to 1 °C and warm biases of up to 3 °C as shown in Figure 4.9. These land contamination effects associated with the relatively coarse ECMWF grid are minimized and accuracy of meteorological forcing in the vicinity of the coastal regions is improved.

#### 4.2.5 Model Setup With Black Sea Net Flux

The Black Sea freshwater water balance is the key element which determines the barotropic transport through the system and hence the response of the TSS. In particular, the total precipitation,  $P$ , and evaporation,  $E$ , for the Black Sea balance each other, while the total freshwater input from rivers,  $R$ , determines the net flux of water, and is balanced by the rate of change of the mean sea level ( $\frac{\partial \bar{\eta}}{\partial t}$ ), plus the net outflow from the Black Sea through the Bosphorus ( $Q_b$ ). Previous studies have shown that the upper and lower layer flows,  $Q_u$  and  $Q_l$  respectively, are correlated with a the

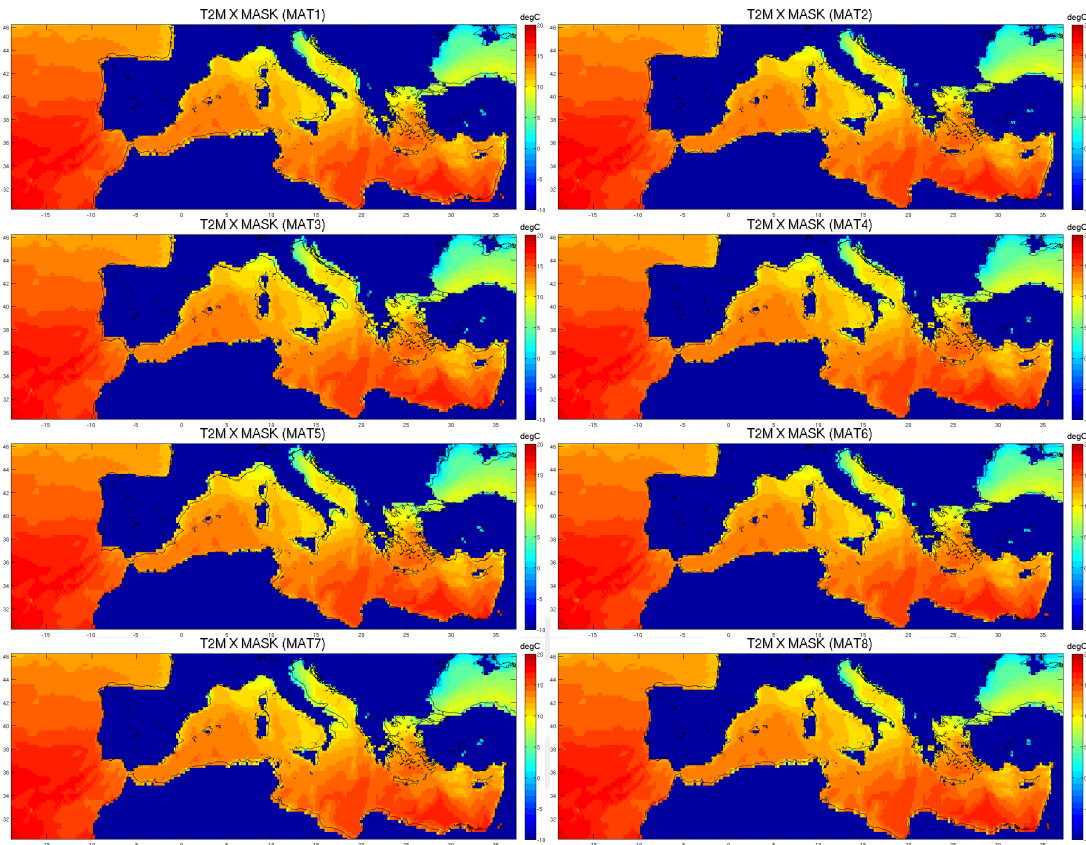


Figure 4.8: Eight matrices created using the land-sea masked 2 m air temperature field.

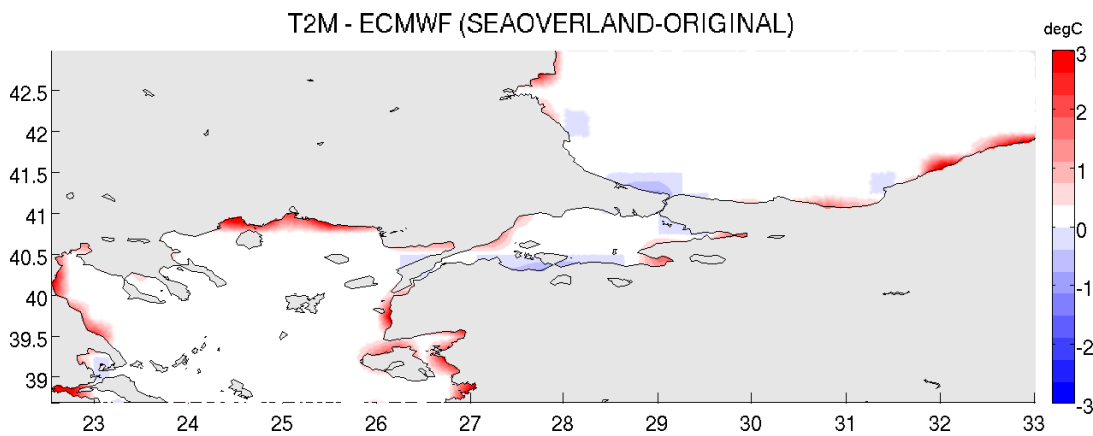


Figure 4.9: Difference in 2 m air temperature before and after the 30th sea over land iteration.

net outflow  $Q_b$  (Möller, 1928; Özsoy *et al.*, 1986, 1988; Maderich and Konstantinov, 2002). To assess the role of Black Sea originated flux on the TSS, the mean freshwater input ( $E - P - R$ ) to the Black Sea in the vicinity of the open ocean boundary of

the Black Sea is prescribed, using monthly mean climatological values of the Black Sea freshwater input compiled by *Kara et al.* (2008), shown in Figure 4.10. Doing so, it is inherently set the rate of change of Black Sea average sea level to zero, as this is required in an annual average sense and the same assumption is extended to the instantaneous state. The freshwater input is maximum in the late spring (551 km<sup>3</sup>/y) and is minimum in autumn (-95 km<sup>3</sup>/y). In order to conserve the total volume of the model domain, the same amount of water is added or removed along a coastal strip of the open ocean boundary in the Aegean Sea. A more detailed description of the water budget formulation applied in this model configuration is presented in Appendix A

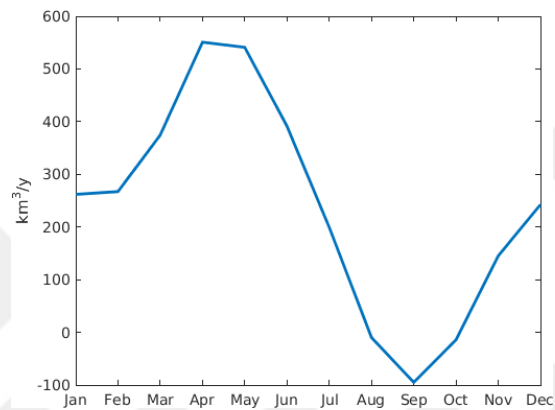


Figure 4.10: Monthly mean climatological freshwater input ( $-E + P + R$ ) of the Black Sea from *Kara et al.* (2008) used in experiment BBInc.



## CHAPTER 5

### TSS LOCK-EXCHANGE MODEL WITH IDEALIZED INITIAL CONDITIONS

The analysis of the simulations and comparison with observations is handled in steps. First, the results of an idealized simulation are presented, the lock-exchange experiment, described in the following sections so-called the 'BASIC'. The model is run without any atmospheric forcing, namely wind speed, water and heat fluxes on the surface are set to zero. The net fluxes originating from the Black Sea as a result of its water budget are excluded in these first set of simulations. The currents in the Marmara Sea and upper/lower layer volume fluxes in the straits are simulated. Furthermore, the model sensitivity to horizontal and vertical mesh resolution, viscosity and diffusivity coefficients and constant wind forcing are investigated. An optimum of the various choices was used resulting in model behavior that best mimicked some observed flows. Other crucially important dynamical tests on strait dynamics such as sensitivity to geometric features, initial conditions and parameterizations related to the open boundaries were extensively studied by *Sözer* (2013) in a stand-alone model of the Bosphorus dynamics. Therefore, such tests are not covered in this study.

The subject of the next section includes the model setting which is generalized to include variability in atmospheric forcing and seasonality of the Black Sea freshwater budget. This results in two additional simulations: the first one (BBExc) including solely the atmospheric forcing but ignoring net mass fluxes from the Black Sea and the second one (BBInc) including net freshwater water flux from the Black Sea and the realistic atmospheric effects. The analyses concentrate on the upper 50 m of the Marmara Sea where the spatial and temporal variations are most pronounced. In the

last part, the simulated fluxes through the straits are compared to the independent data set from *Jarosz et al.* (2011a).

## 5.1 The BASIC Experiment

### 5.1.1 Marmara Sea circulation

The simulated surface circulation of the Marmara Sea averaged over the third month of integration, shown in Figure 5.1, is characterized by a well-defined strong jet leaving the Bosphorus with core velocities of  $\sim 1.0$  m/s. In addition to that, there is a basin-scale anti-cyclonic gyre with an average speed of 0.2 m/s and a series of small eddies ( $\sim 20$  km in diameter) scattered around the pathway of the main flow and the coastal embayments with different signs of vorticity. The simulated main flow continues to the southern coast moving parallel to the Bozburun peninsula turning towards the northwest over the shelf region and meanders before funneling into the Dardanelles Strait. The eddies are separated from the main flow due to natural obstacles like islands, coastlines or rapid changes in depth. Some of the resolved eddies are identified and reported in previous studies. These are for example the ones reported in the vicinity of the Bosphorus-Marmara Junction (*Ünlüata et al.*, 1990), a cyclonic eddy located in the southeast coast (*Chiggiato et al.*, 2012) and a coastal cyclonic eddy in the north (*Demyshev and Dovgaya*, 2007). These findings are consistent with earlier observations (*Beşiktepe et al.*, 1994; *Gerin et al.*, 2013) and concurrent findings of *Sannino et al.* (2015). The BASIC simulation reveals that the eddy activities are concentrated around the region of inflow into the Marmara Sea.

The current plot at 20 m depth shows that the interfacial waters are transported with the Aegean inflow following the main channel and enters into the Marmara Sea (Figure 5.1). In the entrance region, the flow meanders and forms two quasi-persistent eddies: a reversing sense of rotation ( $\sim 15$  km in diameter). At 50 m depth, the circulation pattern changes notably. The Dardanelles effluent entering the Marmara Sea follows the deep channel on the southern side of the widening section and continues straight until it hits the Marmara Island. The current at this stage bifurcates leaving the northward branch to recirculate back into the Dardanelles along the north-



ern half of the widening section of the Dardanelles Strait while the weaker southern branch flows around the Marmara Island before sinking deeper in the westernmost depression. There is a series of eddies moving slowly with different signs of vorticity extending down to 100 m depth (not shown here).

The simulated mid-basin pycnocline is set about 20 m and does not oscillate much due to lack of atmospheric or barotropic forcing in the BASIC experiment. Nevertheless, the 10 m circulation map shows that Mediterranean flow enters into the Bosphorus above the 10 m level. This indicates that the pycnocline is tilted upwards towards the Bosphorus and the jet leaving it is confined to the upper 10 m.

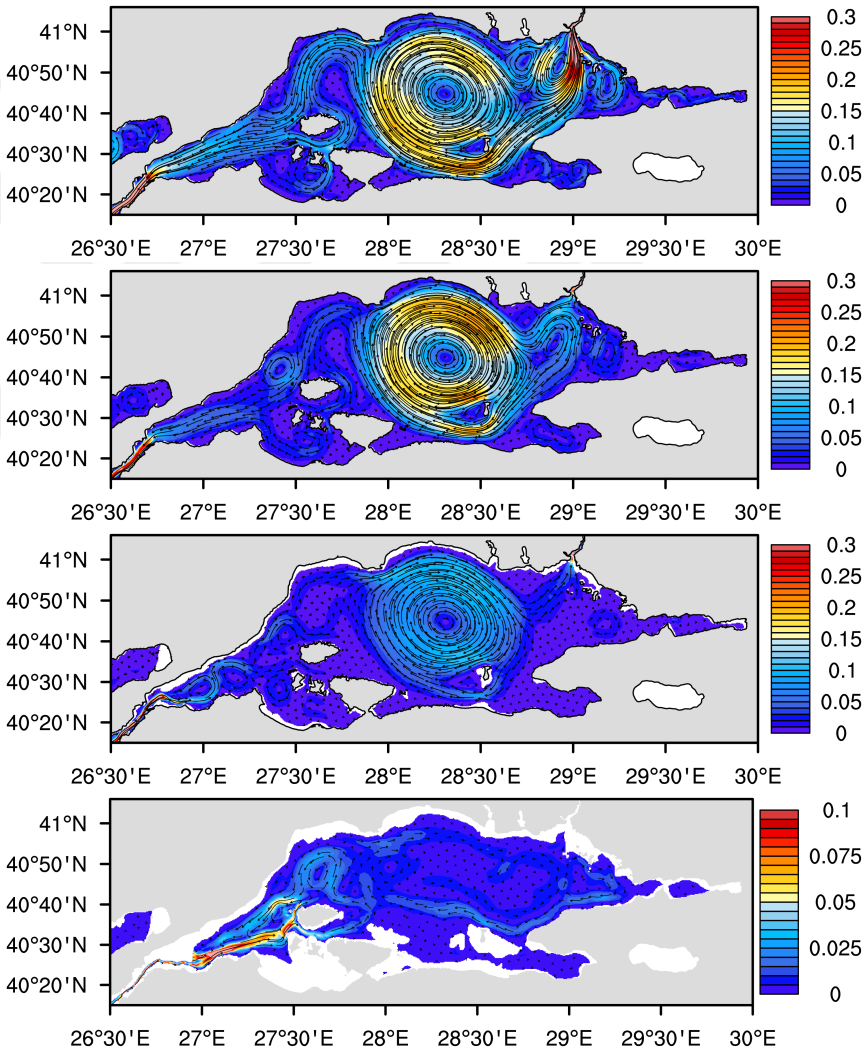


Figure 5.1: Surface, 10 m, 20 m, 50 m level circulation in m/s in the Marmara Sea averaged over the last month of simulation BASIC (from top to bottom). Note that different color scales are used for different depths.

## 5.2 Temporal evolution of the flow in the straits

The temporal evolution of the gravity-driven flow through the Bosphorus and the Dardanelles are analyzed in Figure 5.2 . Figure 5.3 depicts a time series of daily averaged kinetic energy in the Marmara Sea and volume transports passing through Section B1 and D1, shown in at the southern ends of the Bosphorus and Dardanelles straits (shown in Figures 1b and 1c). The time series of volume transport shows that net volume transport initially responds very rapidly, shooting up in a few days and finally reaching a stable state after two weeks indicating a fast adjustment period in the Bosphorus Strait and slower settling of the Marmara Sea, largely due to the adjustment of the larger basin. The kinetic energy diagram quantifies an adjustment period of approximately 30 days in the Marmara Sea, before the kinetic energy becomes relatively constant.

These results clearly show the roles of straits primarily determining the exchange flows through the entire TSS, by adjusting to forcing in a very short time as compared to the response of the system as a whole. The flow in the Straits adjust within less than a day or two, thanks to the suggested main hydraulic controls at the contraction and sill of the Bosphorus (roughly at 24 and 48 km on the lhs, Figure 5.2) and the narrows at Nara Pass of the Dardanelles Strait (at about 30 km, rhs, Figure 5.2). Once these hydraulic controls are established, the system evolves further by density adjustments in the larger domain including the basin of the Marmara Sea. When the barriers between the water masses located at the mid-strait position are released, the density difference creates horizontal pressure gradients. As a result, initially stagnant heavier waters start moving in the direction of the low density basin. In the Bosphorus strait the along-strait bottom layer flow evolves and passes over the northern sill within the first day of integration before the Black Sea waters enter the contraction zone (Figure 5.2, left panel). Mass conservation in the straits dictates water motion on the surface layers in the opposite direction. The velocity and density fields adjust themselves to the topography. After 15 days of integration, the upper and lower layer flows are fully established in a quasi-steady state in the Bosphorus. This period is even quicker in the much wider Dardanelles Strait as a result of the lower initial density gradient between the Aegean and the Marmara Sea (Figure 5.2, right panel). *Özsoy et al. (1986)*

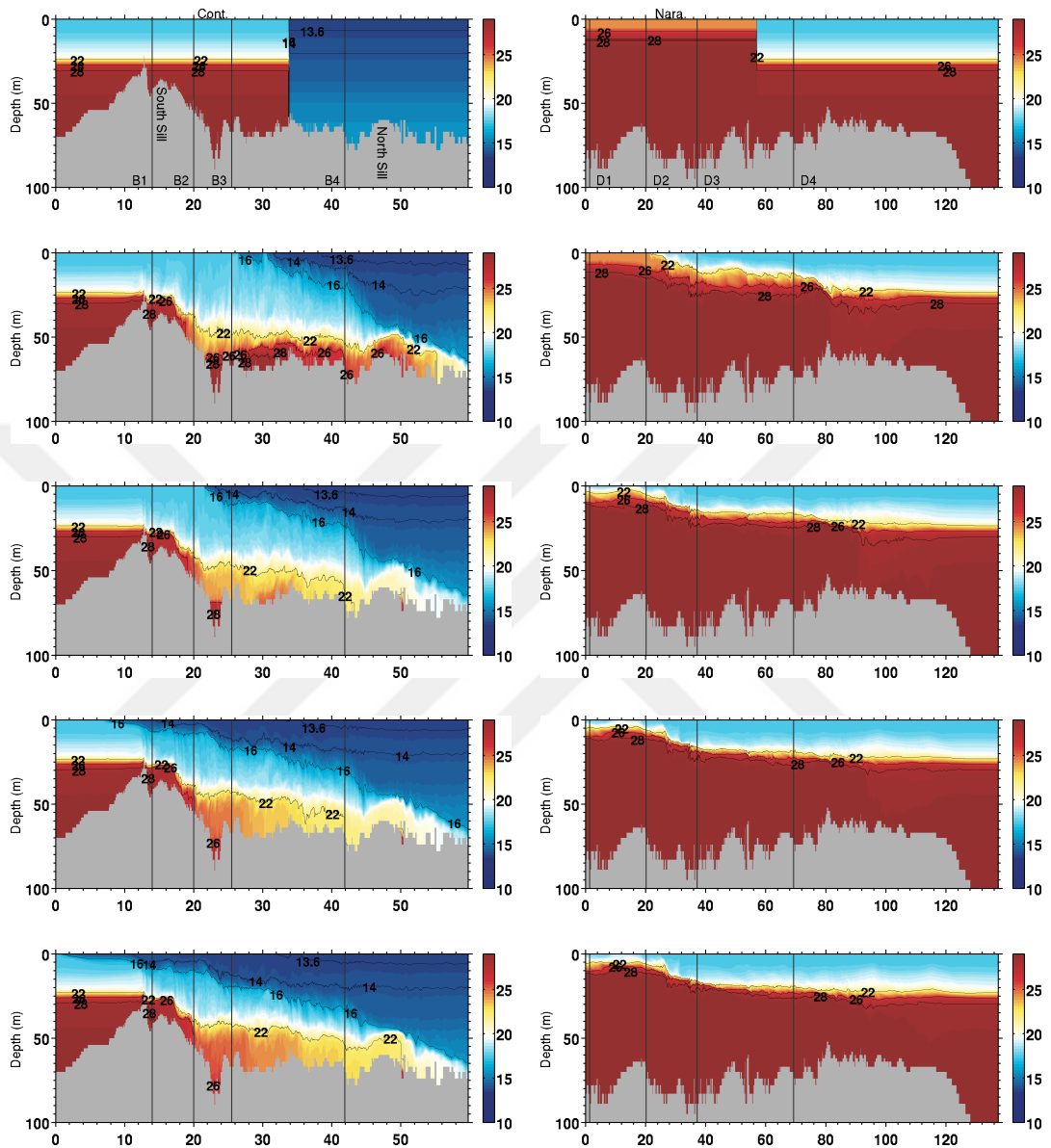


Figure 5.2: Snapshots of potential density along the Thalweg of the Bosphorus (from south to north, left panel) and Dardanelles (from south to north, right panel) at the initial state and after 1, 3, 5 and 7 days (from top to bottom). The x-axis denotes the distance in km.

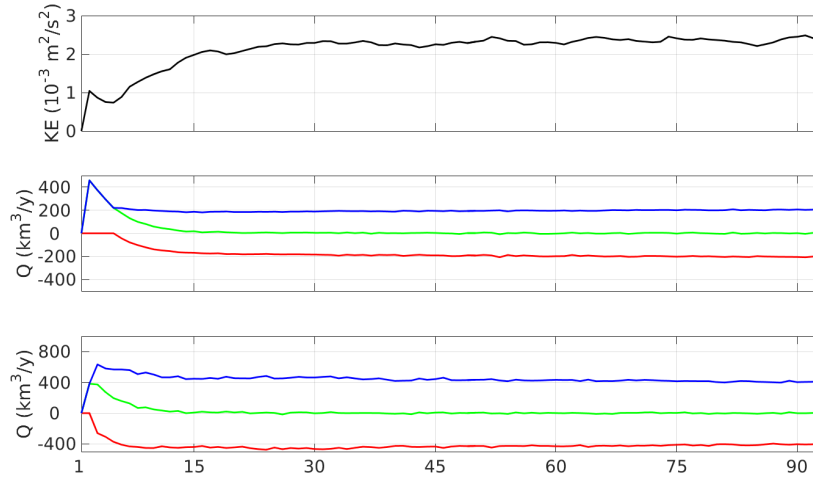


Figure 5.3: Time series of total kinetic energy averaged over the Marmara Sea (top panel) and upper layer (red), lower layer (blue) and net (green) volume transport through section B1 (see Figure 1.1 for the location of the section, bottom panel).

and *Sözer* (2013) showed that the Bosphorus is a unique example of the maximal exchange regime. The Dardanelles, however, possesses the sub-maximal exchange regime (*Oğuz and Sur*, 1989). The link between the regime changes in the flow field and the mixing in the Bosphorus can be tracked using Richardson number discussed by *Oğuz* (2005). The critical values of Richardson number which gives the ratio between the restoring density gradient and shear, with values  $< 0.25$  indicate shear instabilities especially along the zero velocity surface in the vicinity of the contraction and the northern sill in Bosphorus (Figure 5.4).

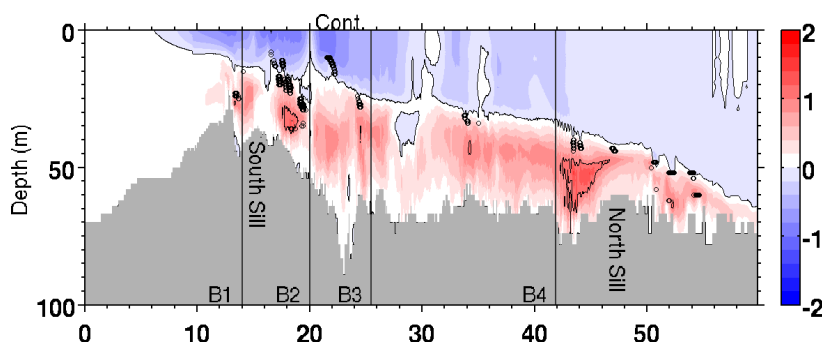


Figure 5.4: Horizontal velocity (in m/s) along the thalweg of the Bosphorus (from south to north) averaged over the last month of simulation BASIC. Contour lines are plotted at an interval of 1 m/s. Circles denote the points where flow has shear instabilities defined by the Richardson number less than 0.25.

### 5.3 Sensitivity tests

The basic experiment shown in the previous section captures the main features of the circulation and stratification in the TSS. However, the new model implementation should be tested in many aspects, as it will later form the foundation of a realistic TSS application. In the following part, unless it is stated, the model setup is kept the same as in the basic experiment in order to isolate effects of parameter changes.

#### 5.3.1 Impact of horizontal and vertical mesh resolution

In order to test the effects of unstructured grid resolution some tests are made with changes in grid. Because the changes are more effective in fast-responding and dynamically important straits, the horizontal mesh is refined in the straits and leave the coarse resolution in the rest of the domain. The effects of mesh resolution are tested in a series of sensitivity experiments performed in Table 5.1 applied to geometric component of the TSS model. The parameters corresponding to the BASIC experiment are also presented in Table 5.1, and later varied in other sensitivity tests listed.

In VERT\_0.5, the number of vertical elements is reduced to half of the BASIC configuration resulting in the thickness of the tetrahedral elements to be tripled within the first 50 m. Furthermore, resolution in the straits is re-scaled by factors of 1.25 and 1.5 in simulations LOW\_HORIZ\_1.25 and LOW\_HORIZ\_1.5, respectively.

Table 5.1: Horizontal and vertical mesh resolution in experiments BASIC, LOW\_VERT, LOW\_HORIZ\_1.25 and LOW\_HORIZ\_1.5. Abbreviations: Bosp-Bosphorus Strait, Dar-Dardanelles Strait, MS-Marmara Sea, AS-Aegean Sea and BS-Black Sea.

Simulation (m)	Horizontal resolution (m)				Number of vertical levels
	Bosp	Dar	MS	AS/BS	
BASIC	65	150	1600	5000	110
VERT_0.5	65	150	1600	5000	55
LOW_HORIZ_1.25	85	200	1600	5000	110
LOW_HORIZ_1.5	100	225	1600	5000	110

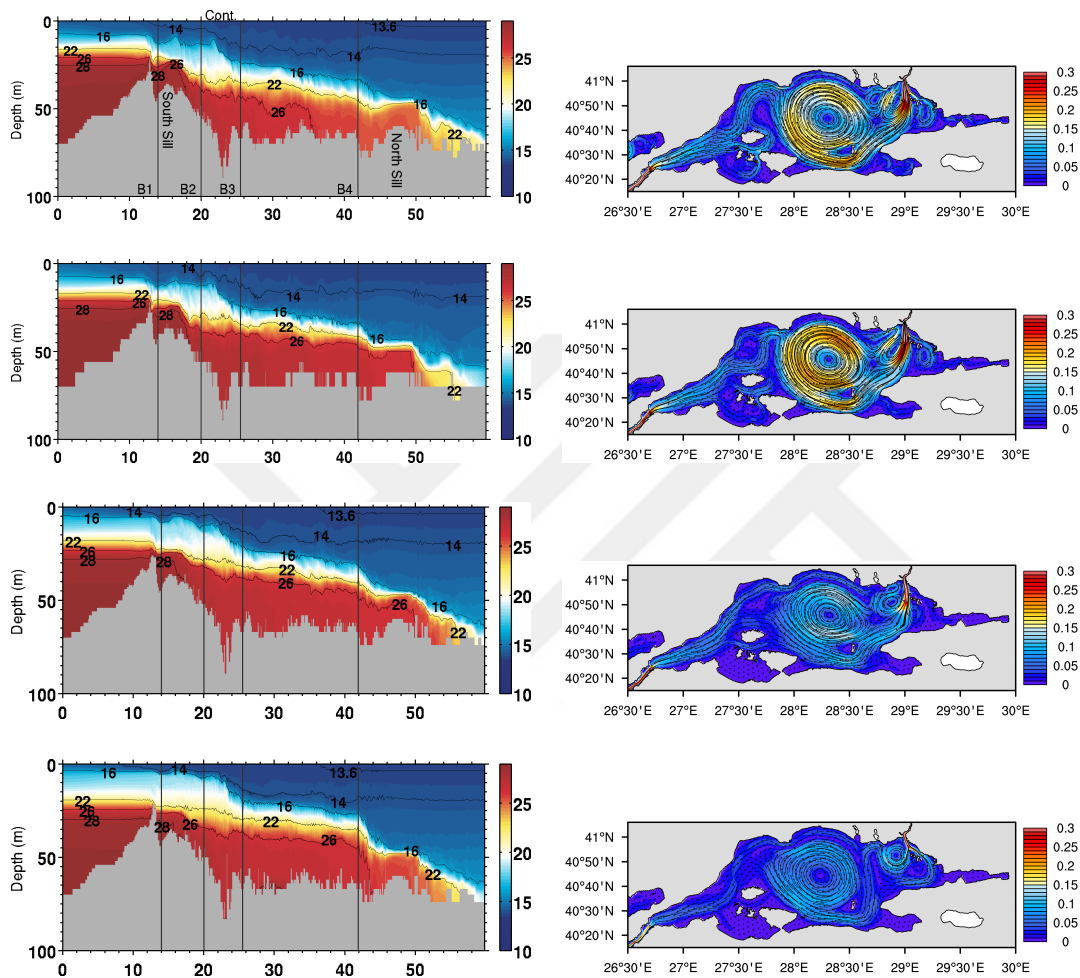


Figure 5.5: Simulated density along the Thalweg of the Bosphorus (left) and surface circulation in m/s (right) in the Marmara Sea averaged over the last month of the simulation for experiments BASIC, LOW\_VERT, LOW\_HORIZ\_1.25 and LOW\_HORIZ\_1.5 (top to bottom).

Because the interface thickness, defined as depth between the  $\sigma_{16}$  and  $\sigma_{26}$  isopycnals in the Bosphorus, is reduced in VERT\_0.5 while the horizontal velocities are on the same order as the BASIC run, turbulent mixing in vertical is reduced in the VERT\_0.5 experiment. Kinetic energy averaged over the Marmara Sea (not shown here) is decreased by 57% in experiment VERT\_0.5 compared to BASIC. This is mostly associated with the weaker coastal currents and eddies especially in the bays located on the southern shelf.

Decreasing the horizontal resolution in the straits results in a considerable drop in the upper and lower layer volume transport in the Bosphorus and the total kinetic energy in the Marmara Sea. The reduction is more than the reduction in resolution itself. For example, reduction in resolution by 50% (LOW\_HORIZ\_1.5) leads to drop in the kinetic energy over the Marmara Sea and the upper layer volume transport through the Bosphorus by 83% and 75% compared to the BASIC experiment, respectively. In LOW\_HORIZ\_1.25 case, the kinetic energy and the upper layer volume transport drop by 66% and 42% compared to BASIC, respectively. The surface circulation in the Marmara Sea is sensitive to the resolution changes in the straits. In LOW\_HORIZ\_1.25, the lower transport through the Bosphorus leads to a weakening of the jet leaving it, and a weakening of the overall Marmara Sea circulation (Figure 5.5). In LOW\_HORIZ\_1.5, the Marmara Sea circulation is even weaker than in LOW\_HORIZ\_1.25 (Figure 5.5).

The above results show that giving away from the seemingly optimal BASIC resolution seems to deteriorate the results. In addition to the effects on circulation through the accurate representation of the Bosphorus jet, the horizontal and vertical fine resolution are required for accurate representation of controlled flow in straits. The compromise in resolution impacts the areas where rapid changes occur in the interfacial slope, such as at around 42 km in the Bosphorus in Figure 5.5, where a false transition seems to occur before reaching the sill at 48 km. These could possibly influence the nature of hydraulic controls, for instance at the sill, thereby changing the overall behavior of the TSS exchange.

For model validation (later in this section) the BASIC mesh configuration appears to have sufficient configuration to maintain realistic results throughout the domain

allowing the sensitive and accurate responses of the two straits.

### 5.3.2 Impact of horizontal viscosity and diffusivity coefficients

Now, the effect of variations in horizontal viscosity and diffusion coefficients is evaluated. In order to isolate effects of horizontal viscosity and diffusion, all other parameters are kept the same as in experiment BASIC. The coefficients of horizontal viscosity  $A_h$  and horizontal diffusion  $K_h$  used in the sensitivity experiments are displayed in Table 5.2. They are centered around the reference values which are chosen for reasons of numerical stability and solution convergence based on the work of *Wallcraft et al.* (2005). The response of the model is evaluated using the mean density taken along the thalweg of the Bosphorus and the mean surface flow of the Marmara Sea.

Table 5.2: Sensitivity experiments testing the impact of horizontal viscosity and diffusivity coefficients.

Simulation	Horiz. viscosity $A_h$ ( $\text{m}^4/\text{s}$ )	Horiz. diffusivity $K_h$ ( $\text{m}^2/\text{s}$ )
BASIC	$2.7 \cdot 10^{13}$	2000
LOW_VISC	$8.61 \cdot 10^{12}$	2000
HIGH_VISC	$1.17 \cdot 10^{14}$	2000
HIGH_DIFF	$2.7 \cdot 10^{13}$	30000
LOW_DIFF	$2.7 \cdot 10^{13}$	100

In the Bosphorus Strait, the influence of the contraction and the sills on the hydraulically controlled flows and associated mixing zones are clearly visible in all experiments (Figure 5.6). The pycnocline is very sharp, separating the low density Black Sea waters (density of  $\sim 14 \text{ kg/m}^3$ ) from the dense Mediterranean waters (density of  $\sim 28 \text{ kg/m}^3$ ). The region between these layers are assumed to be the interface. As seen from the Figure 5.6, the inclination of the isopycnals along the thalweg of the straits is reproduced successfully, compared to the observations described by *Gregg et al.* (1999). Experiments HIGH\_DIF, LOW\_DIFF and LOW\_VISC do not vary much from each other, however they depart significantly from the BASIC close to the bottom layer. Figure 5.6 reveals that waters entering from the southern Bosphorus are lighter in LOW\_VISC than in BASIC. In experiments HIGH\_DIF and LOW\_DIFF,



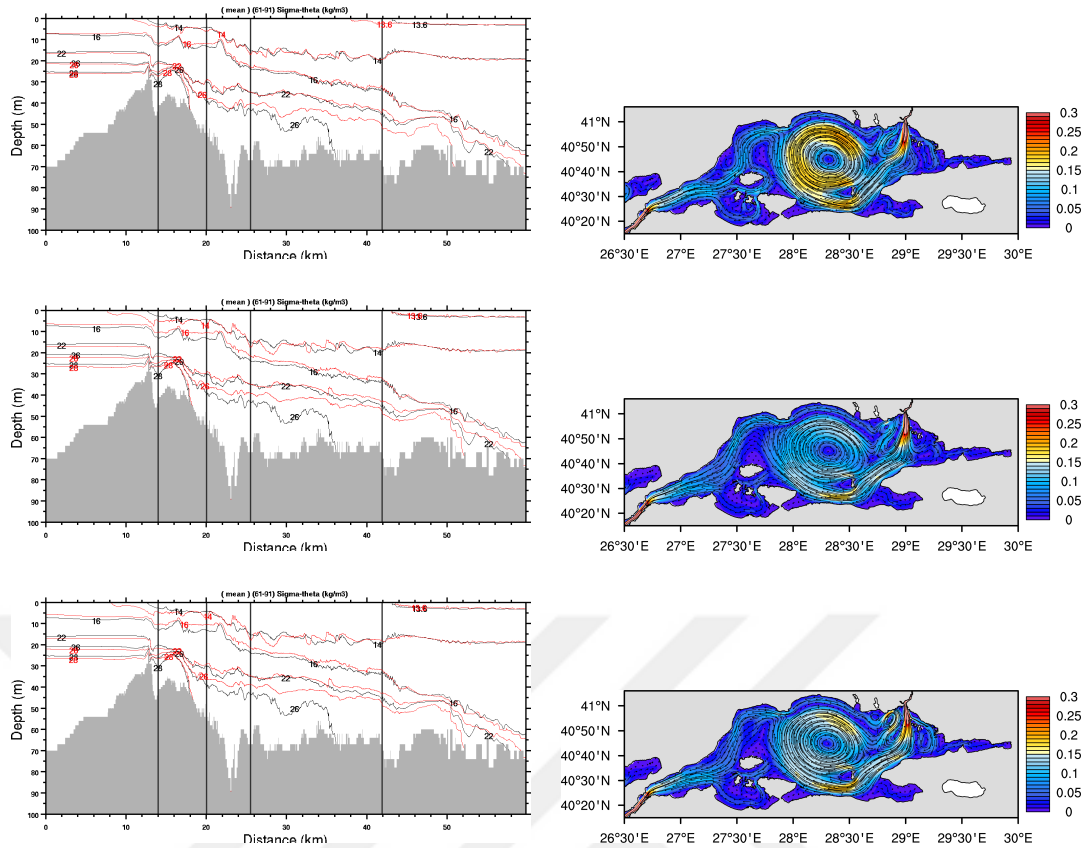


Figure 5.6: Simulated isopycnals (13.6, 14, 16, 22, 26 and 28 kg/m<sup>3</sup>) along the Thalweg of the Bosphorus for BASIC (black line) and sensitivity experiments (a) LOW\_VISC, (b) HIGH\_DIFF and (c) LOW\_DIFF (red lines) averaged over the last month of simulation.

the isopycnals in the interface find their balance close to the surface. They have homogeneous bottom layer with high density flowing over the northern sill and even spreading onto the Black Sea continental shelf of the Black Sea.

The simulated Marmara Sea mean surface circulation pattern of HIGH\_DIF, LOW\_DIFF and LOW\_VISC cases do not vary much from the BASIC experiment. The differences are enhanced around the Bosphorus-Marmara Sea junction. Increasing the horizontal diffusivity may cause surface currents to be slower in the Marmara Sea and mitigate the Bosphorus jet branching between the Princess islands and the Asian coast. In the LOW\_DIFF experiment, the eddies near the Bosphorus jet extends zonally. The experiment HIGH\_VISC becomes unstable after 50 days of integration and results in model blow-up. If the diffusivity is increased to value of 30000 m<sup>2</sup>/s than

the experiment converges to a steady-state solution. However, the solution is very diffusive and far from being realistic. It can be summarized that  $A_h$  and  $K_h$  modifies the flow field in the vicinity of Bosphorus-Marmara Sea Junction.

### 5.3.3 Persistent wind field

In the previous experiments, the circulation maps show that there are not pronounced changes in surface flow field of the Marmara Sea. Nevertheless, the observations obtained from the drifter experiments by *Gerin et al. (2013)* indicate that the surface circulation in the Marmara Sea is complex and highly variable mostly because of the instantaneous wind forcing. Different from the BASIC experiment, the wind stress at the sea surface is set to the mean values over the entire domain to analyze the wind-driven circulation in the Marmara Sea in its lock-exchange configuration. Two persistent wind directions are used to study summer and winter circulation and stratification in the TSS. The persistent wind speed is set to 4 m/s for both the northeasterly (WIND\_NE) and southwesterly wind (WIND\_SW) experiments.

The kinetic energy averaged over the Marmara Sea shows an increase of 20% in the WIND\_NE case compared with BASIC, whereas it is reduced by 36% in the experiment WIND\_SW. Consistently, the upper layer transport through southern Bosphorus is stronger in WIND\_NE than in BASIC (219 km<sup>3</sup>/y compared with 200 km<sup>3</sup>/y, averaged over the last month of simulation). In the WIND\_SW case, upper layer transport is reduced to 152 km<sup>3</sup>/y.

In experiment WIND\_NE, the distance between the isopycnals in the upper layer diminishes. Moreover, the position of the 14 kg/m<sup>3</sup> isopycnal in the vicinity of the northern sill sinks ~10 m favoring the increase in the volume transport assuming that the hydraulic control keeps the along strait velocity close to the BASIC case. The location of the 26 kg/m<sup>3</sup> isopycnal confirms this, as well. In WIND\_SW, however, the hydraulic control may be lost in the upper layer (Figure 5.8).

In BASIC, the mean Marmara Sea surface circulation map shows a well defined Bosphorus jet and basin wide anti-cyclonic eddy with basin mean speed of about 0.2 m/s (Figure 5.1). Under the constant predominant northeasterly wind speed, the

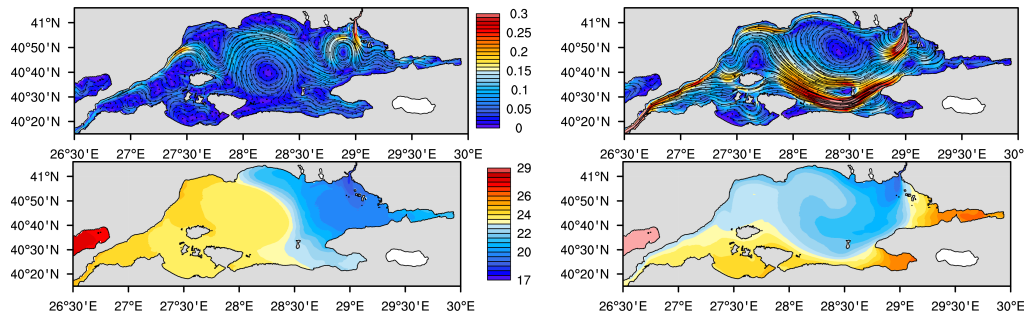


Figure 5.7: Simulated surface circulation in m/s (upper panel) and salinity in psu (lower panel) in the Marmara Sea averaged over April 2008 for experiment WIND\_SW(left panel) and experiment WIND\_NE (right panel)

Bosphorus jet heads towards the west as soon as it enters into the Marmara Sea. The model result reveals strong coastal currents. Flow on the southern shelf starts in front of the Bozburun Peninsula, encircles the Imrali island and turns to the northwest. The mid-basin anticyclonic eddy is weaker and deflected to the northeast compared to the BASIC experiment. Moreover, the current passing between the islands on the west is stronger (Figure 5.1). In WIND\_SW, the Bosphorus jet still exists, no flow reversal in upper layers of the Bosphorus occurs. Nevertheless, it is weaker, narrower and deflected to the east. There are numerous small eddies formed around the mid-basin meandering reversed surface flow. The ones located on the northern side of the mean flow pathway are cyclonic whereas the ones on the south are anti-cyclonic (Figure 5.7).

The surface salinity plots in Figure 5.1 show that southwesterly average winds are effective to replenish the water in the bays, especially in Izmit and Gemlik. In BASIC experiment the surface salinity is uniform and mostly below 23 psu. In WIND\_NE case, the surface salinity field exhibits zonal front and the interface thickness decreases in the direction of the Dardanelles unlike the WIND\_SW experiment in which the front is meridional and the interface thickness is larger. Upwelling in the bays results in high salinity values in the WIND\_NE case.

To sum up, persistent winds impact the volume transport through the Bosphorus/Dardanelles. Moreover, the surface circulation differs from the BASIC case in magnitude and pattern in the Marmara Sea (especially in the case WIND\_SW). One point to be stressed is that the wind field prescribed in WIND\_SW is not strong enough to trigger

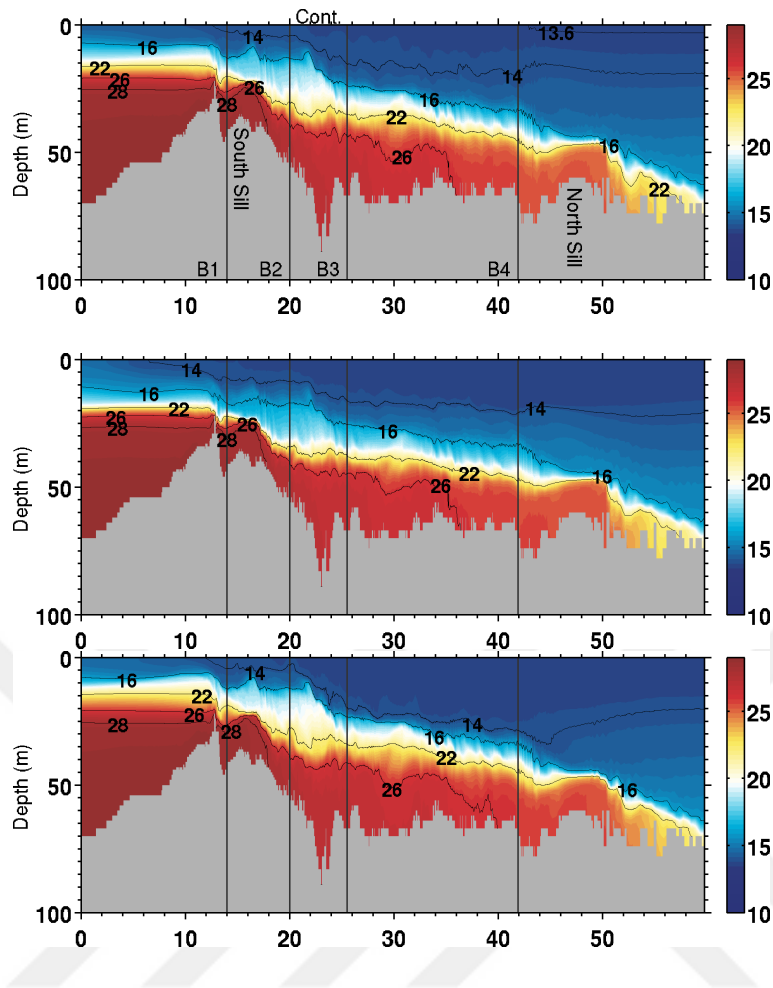


Figure 5.8: Density field ( $\text{kg/m}^3$ ) along the Bosphorus Strait averaged over the last month of the simulation for experiments BASIC (top), WIND\_SW (middle) and WIND\_NE (bottom).

blocking events (upper layer flow reversals) as described by *Latif et al.* (1991).

## CHAPTER 6

### THE RESPONSE OF THE TSS UNDER EXTERNAL FORCING

The key driving forces in the Turkish Strait System are the atmospheric forcing and the Black Sea freshwater input (*Özsoy et al.*, 1988; *Gregg and Özsoy*, 2002). The response of the Marmara Sea to both of these factors has been previously taken up by *Chiggiato et al.* (2012) and *Demyshev and Dovgaya* (2007) although the straits have been completely ignored and only represented as inflow / outflow ports in their work. In recognition of the importance of these external factors are taken into consideration in this section. Although the model open boundaries are fictitious (closed) in the Aegean and the Black Seas, it is acknowledged that the effects of neighboring basins by attempting to include their seasonal water budgets.

In this chapter, the model performance in the Marmara Sea and in the Bosphorus will be assessed. There are two a-year long hindcast simulations to be presented: one without (BBExc) and another one with the Black Sea freshwater budget included (BBInc). Two simulations have been performed using realistic atmospheric forcing for the year 2008. Both were initialized with the same temperature and salinity fields from the model results of the lock-exchange experiment that was integrated for three months as described in the previous chapter. First, the capabilities and deficiencies of both simulations, BBExc and BBInc, in simulating the Marmara Sea stratification will be analyzed. Second, more realistic simulation, BBInc, will be further investigated with the focus on the Bosphorus throughflow. The strategy used for the Black Sea freshwater inflow in BBInc is explained in the appendixB in detail. The coding of aforementioned part is done by Ali Aydoğdu.

## 6.1 Model assessment with focus on the Marmara Sea

The surface circulation and salinity fields simulated by BBExc and BBInc averaged for April and October 2008 are shown in Figures 6.1 and 6.2, respectively. In April the circulation differs significantly between the Black Sea unforced and forced cases, as the influence of the net barotropic flow is at its maximum during spring. In October, both simulations exhibit very similar surface circulation, as the system is mainly wind driven during this time when the fresh water effects are at a minimum.

The circulation in April, simulated by BBExc, is characterized by eastward flow in the northern part of the Marmara Sea, and a westward flow in the southern part of the basin, and very little eddy activity. In BBInc in contrast, a strong anticyclonic gyre dominates the eastern part of the Marmara Sea. The difference in the circulation pattern in April between the two simulations is a conspicuous result of the presence of the Black Sea freshwater forcing in BBInc, which reaches a peak in April ( $551 \text{ km}^3/\text{yr}$ , Figure 6.1). In October, freshwater input is very low ( $-14 \text{ km}^3/\text{yr}$ , Figure 6.1). This clearly demonstrates that the barotropic forcing, a result of the freshwater budget in the Black Sea, may cause substantial changes in the surface flow field of the Marmara Sea by fueling the Bosphorus jet and associated anticyclonic eddy which cuts the link between the eastern and the western parts. In other words, the Bosphorus throughflow determines the circulation pattern in the Marmara Sea. Taking the attention to the surface salinity fields, both simulations show differences both in April and October. In simulation BBInc, freshwater from the Black Sea occupies almost the entire Marmara basin in April as well as in October, though waters are significantly fresher in April. In BBExc in contrast, saline waters of Mediterranean origin occupy almost the entire basin.

Next the model results are compared with observations collected during the SESAME Marmara Sea cruise separated into two parts of 4 days duration each. The first part was carried out from 11 to 14 April 2008, and the second part was conducted between 1 and 4 October 2008. Figures 6.3 and 6.4 show the positions of the CTD stations for April and October 2008, respectively. The measured profiles of temperature, salinity and density are depicted as well. The data reveals that salinity determines the density in the basin and temperature modifies it locally. In spring, the surface warming causes

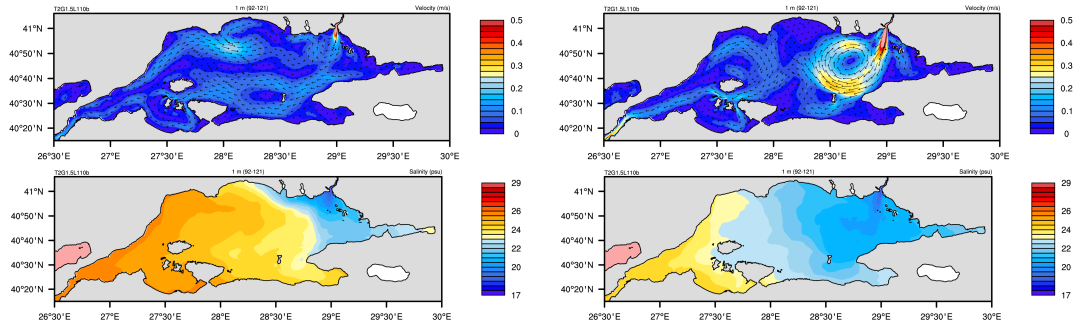


Figure 6.1: Simulated surface circulation in m/s (upper panel) and salinity in psu (lower panel) in the Marmara Sea averaged over April 2008 for experiment BBExc (left panel) and experiment BBInc (right panel).

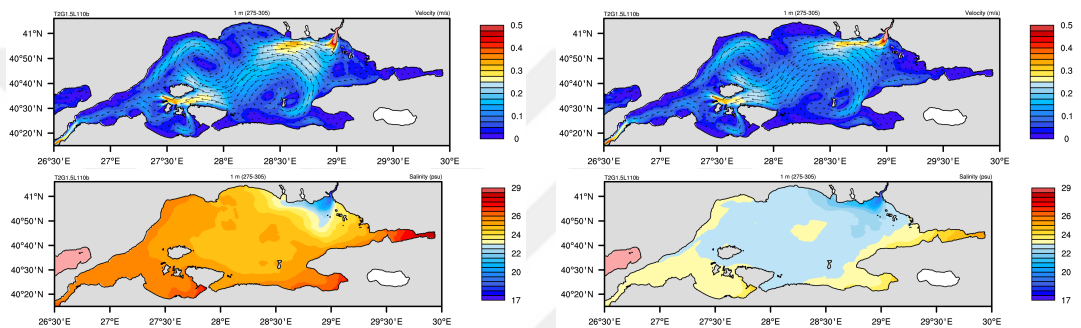


Figure 6.2: The same as Figure 6.1, but for October 2008.

a temperature minimum at  $\sim 20$  m depth (Figure 6.3).

Just below the thermocline, there is a temperature maximum advected from the Aegean Sea. The salinity profiles show that the surface layer in the western part of the basin is well mixed, in contrast in the eastern part it is mostly eroded due to the Black Sea influence. In autumn, decreased Bosphorus volume flux and surface heating lead to higher gradients in temperature and salinity in the vertical. As a result, the pycnocline is sharper in the Marmara Sea (Figure 6.4).

A T-S diagram of water masses in the Marmara Sea is presented in Figure 6.5. Examining the observed profiles is it obvious that there are basically two types of water masses in the Marmara Sea. Near-surface salinity values indicate the influence of the Black Sea. On the other hand, the basin interior below the pycnocline is filled with the saltier ambient water of Mediterranean origin. The temperature measurement shows a straightforward spring and autumn seasonality with quasi-constant values in

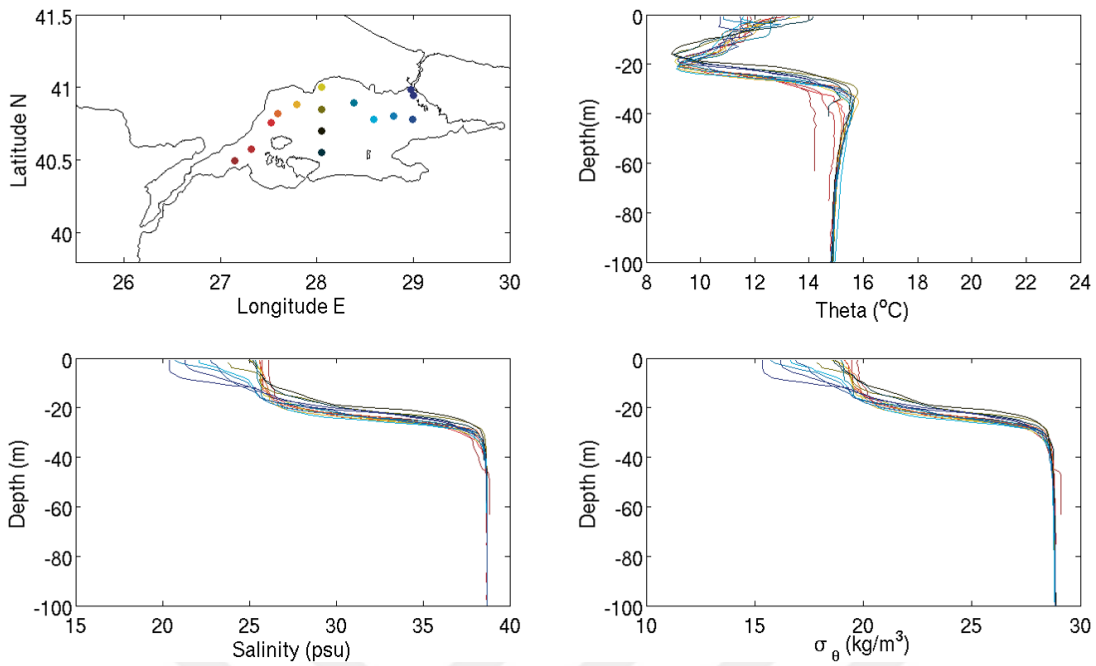


Figure 6.3: Positions of CTD stations collected during the SESAME cruise in April 2008 (top left). Potential temperature (top right), salinity (bottom left) and potential density (bottom right) measured at the corresponding stations.

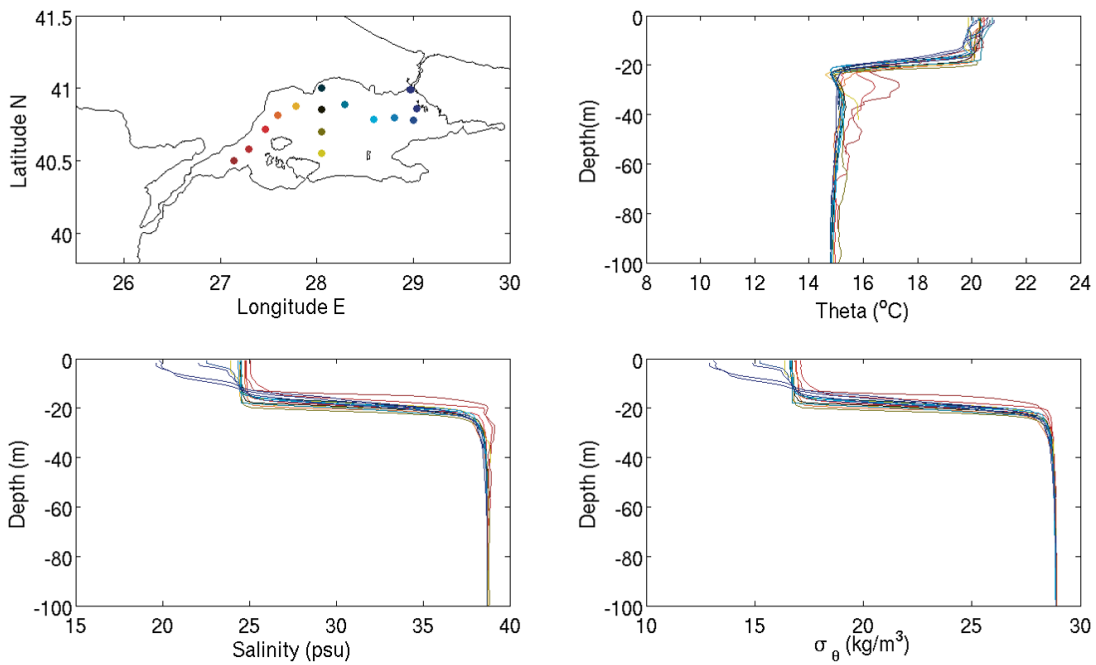


Figure 6.4: Same as Figure 6.3, but for October 2008.



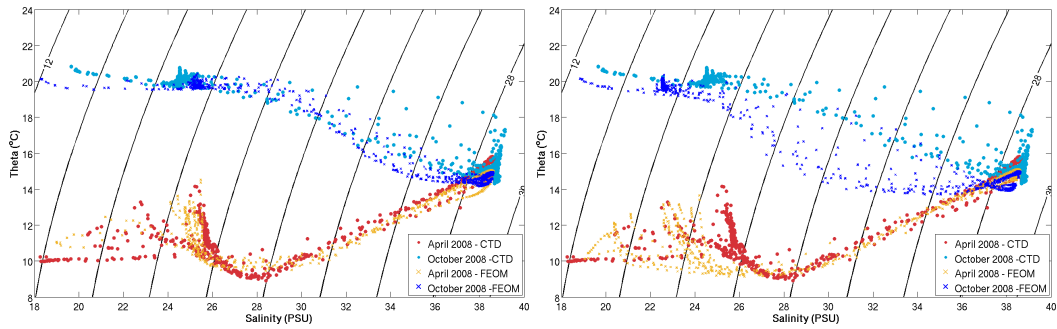


Figure 6.5: T-S diagram of profiles in the Marmara Sea for the time periods of April (red) and October 2008 (blue) from SESAME observations and FEOM hindcast simulations BBExc (left) and BBInc (right). Measurements and values from the model simulations are denoted by circles and crosses, respectively.

the surface layers. The FEOM simulated temperature profiles in the Marmara Sea agrees well with the CTD measurements in BBExc. On the other hand, BBInc simulation shows a conspicuous colder temperature spread in autumn in the T-S diagram. Simulated temperature drops to a minimum of  $\sim 9^{\circ}\text{C}$  in spring that is probably the result of entrainment of the warm and saline bottom water into the Cold Intermediate Layer, CIL, advected from the Black Sea. CIL can be defined a layer of cold water body that is formed in the northwestern shelf as a result of winter convection and sandwiched between the warm surface and deep layers in the Black Sea. Its upper limit is assumed as being  $8^{\circ}\text{C}$ . In autumn temperature reaches a maximum value of  $\sim 21^{\circ}\text{C}$ . Both hindcast simulations show better agreement with the observation excluding the BBInc April 2008 values where the model sea surface salinity is fresher than the observations. This can also be deduced from Figure 6.6.

This is expected as the initial tracer fields are idealized and the lateral boundaries are closed. The water type distribution in the T-S diagram resembles a straight line indicating the proportionality in vertical mixing between the surface and the deep layers through the stratified interface. Water types crossing the isopycnal lines are the indication for diapycnal mixing in the basin. The T-S distribution in the model results indicates that FEOM reproduces mixing with sufficient accuracy.

Vertical salinity and temperature profiles averaged over the CTD stations in the Marmara Sea are presented in Figure 6.6, both observations and model results for BBExc

and BBInc. The comparison is done for the first 50 m of the water column from the sea surface, as water properties below this depth require longer simulation time scales (6-7 years, *Ünlüata et al. (1990)*). The observations (black lines) show that the halocline and thermocline positioned deeper in spring than the autumn. This is evidently due to the high freshwater input into the Black Sea. The solution curves of the thermocline and halocline from the both simulations are in harmony with the observed properties in the Marmara Sea. The position of the interface is realistically represented in BBInc, whereas in BBExc it is too close to the surface and increases to rise with time. Figure 6.6 reveals that including the Black Sea water budget (experiment BBInc) is essential to ensure a higher skill in representing the position of the halocline. However, there is a bias in surface salinity in experiment BBInc. Very low surface salinity in BBInc is linked to the salinity value relaxed to the surface in the Black Sea. Surface temperature discrepancy between simulations and observation does not exceed 0.5 °C. The temperature minimum right above the thermocline in April 2008 is captured in both simulations. Below the thermocline the model experiences a column of colder water ( $\sim 0.5$  °C). This is due to the initial temperature profile selected from the Aegean Sea in the lock exchange experiment. *Beşiktepe et al. (1993)* and *Beşiktepe (2003)* note that lower layer density is controlled by the temperature of the Dardanelles inflow as boundary currents or intrusions.

The model performance is further assessed by means of root-mean-square error (RMSE) comparison. Figures 6.7 and 6.8 show that BBInc results are in better agreement with the observation compared to BBExc for both measurement periods. Despite the initialization with simple profiles, including the Black Sea freshwater input improves the model skill considerably in the Marmara Sea. In experiment BBExc, the source of the high error in tracers is the misplacement of the halocline and thermocline which are too close to the surface. In BBInc, the error field is more dependent on the hydrological properties of the Black Sea that are carried into the surface layers of the Marmara Sea and the tracer values relaxed on the surface along the ocean boundaries. Temperature errors for both hindcast experiments do not depart from each other.

The comparison of the position of the simulated  $\sigma_{25}$  layer averaged over the Marmara Sea (Figure 6.9) reveals the role of the wind and the Black Sea freshwater input on the interface depth. The correlation between the two simulations is high, revealing that

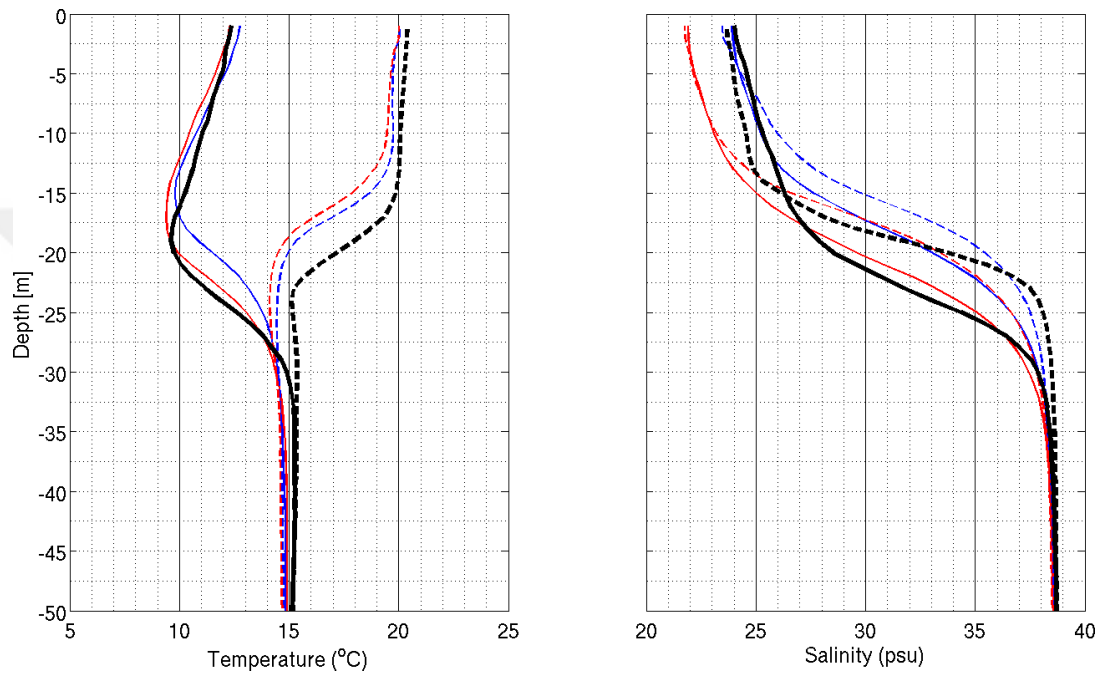


Figure 6.6: Vertical profiles of temperature and salinity in the surface layers of the Marmara Sea averaged over all stations. Model results are interpolated onto the position of the CTD stations for simulations BBExc (blue) and BBInc (red). Black lines represent the observations. Solid and dashed lines indicate profiles for April and October 2008, respectively.

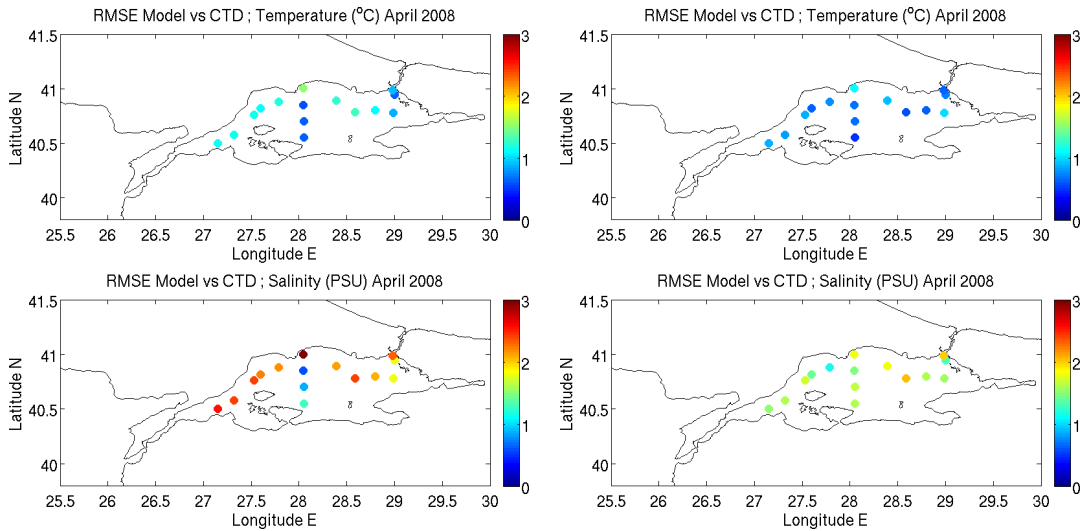


Figure 6.7: Accumulated root-mean-square errors between simulated and observed temperature (upper panel) and salinity profiles (lower panel) in the Marmara Sea for April 2008. The left panel shows root-mean-square errors for experiment BBExc, the right panel for experiment BBInc.

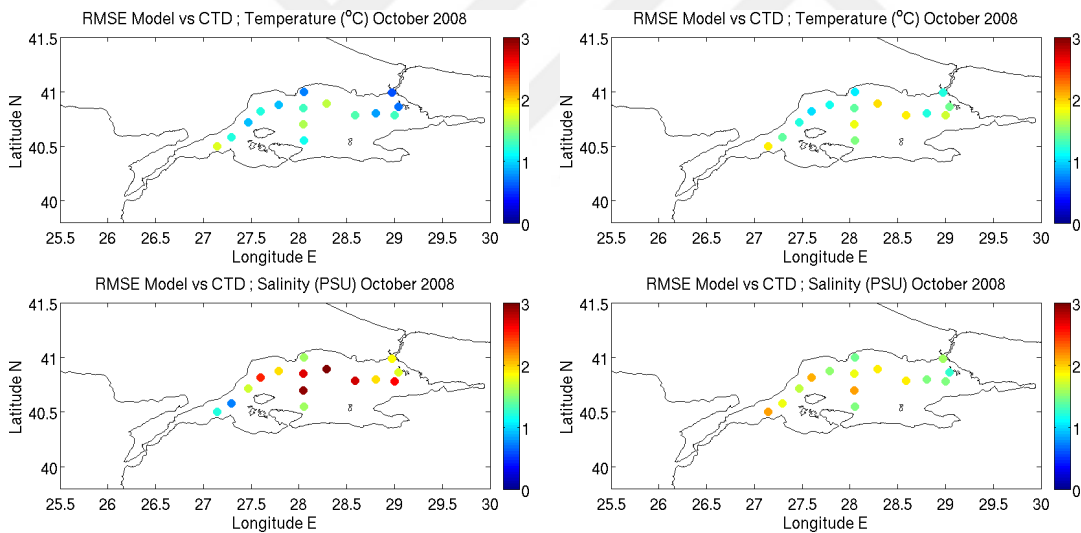


Figure 6.8: The same as Figure 6.7, but for October 2008.

atmospheric forcing is responsible for high frequency variability in both simulations. In particular, the interface depth is sensitive to strong storms leading to up to 2 m change in depth within a few days. In experiment BBExc, the missing barotropic forcing of the Black Sea results in a lower interface position compared with BBInc, which is in average 2 m shallower. Additionally, the seasonality of the  $\sigma_{25}$  layer is clearly visible in the case of the BBInc, showing that the position of the interface is

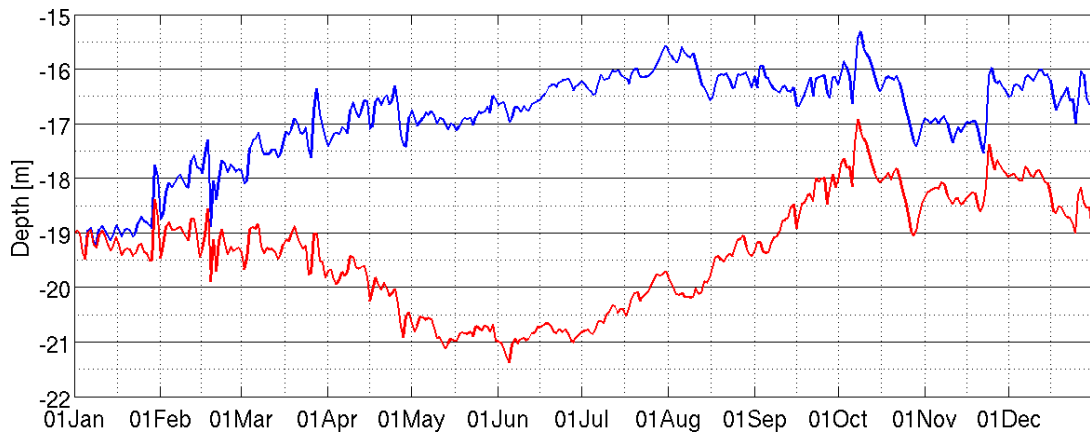


Figure 6.9: Simulated depth of the sigma-25 layer averaged over the Marmara Sea for the experiments BBExc (blue) and BBInc (red).

controlled by the freshwater balance in the Black Sea.

## 6.2 Model assessment with focus on Bosphorus Strait

In the following the concentration is on the most realistic simulation, BBInc, and further investigate the ability of the model to simulate the Bosphorus strait. The model results are now compared with the observed time series of velocity profiles at the southern Bosphorus from *Jarosz et al.* (2011a) (Figures 6.10 and 6.11). Observations indicate that the along-strait velocity component of the southern Bosphorus (at the middle of Section B1) varies considerably throughout the year 2008. The isotach, the zero velocity line, separates the upper and lower layers. In the simulation, the mean depth of the isotach is 8.75 m, shallower than the observed depth of 13.5 m reported by *Jarosz et al.* (2011a). The maximum simulated along-strait speed in the upper layer (1.31 m/s) is considerably less than the observed value of 2.3 m/s (*Jarosz et al.*, 2011a).

Figure 6.12 shows a cross section passing through the thalweg of the Bosphorus Strait, observed in September 1994 and model results for September 2008. Note that the stratification in the simulation is kept stable over the total simulation period and disturbed only by the synoptic weather systems passing over the region. Figure 6.12 reveals that model results are in good agreement with observations. The inspection of the constant density lines show us there is a control imposed by the Bosphorus geom-

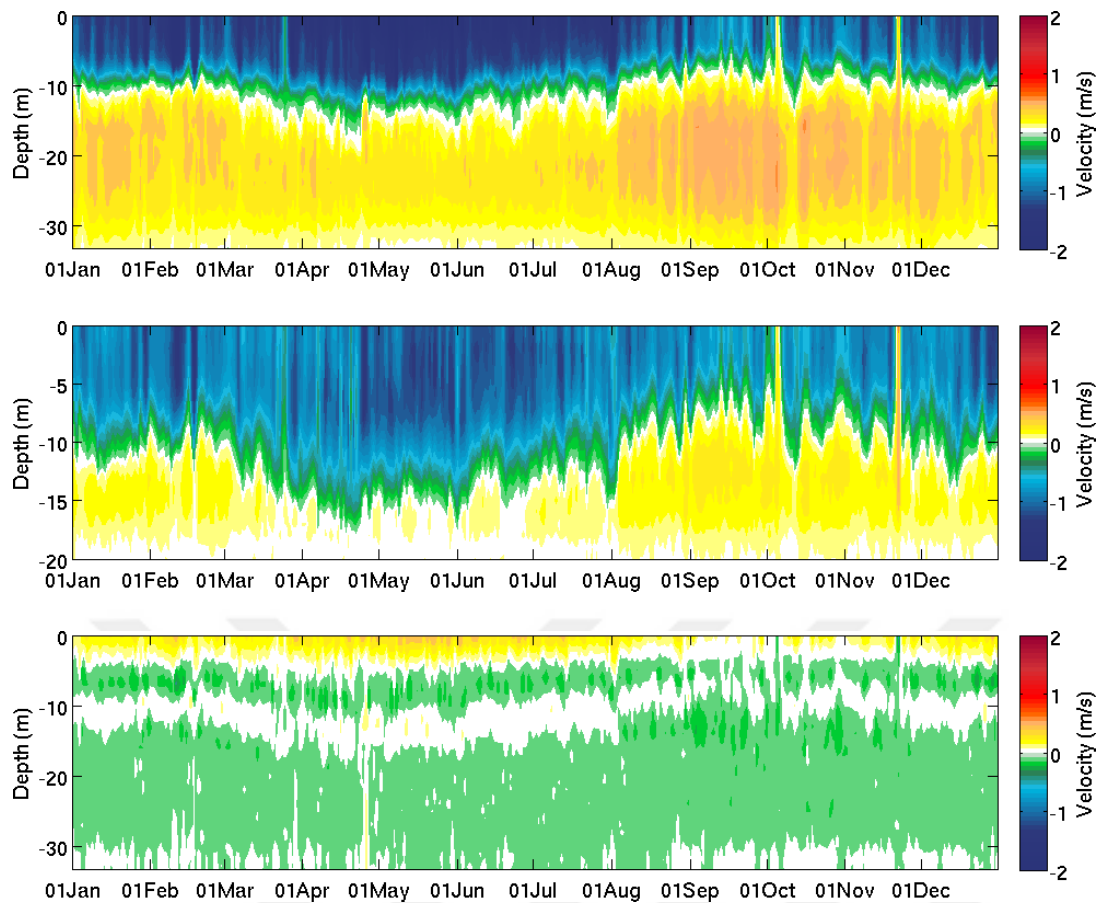


Figure 6.10: Time series of the simulated along-strait velocity profiles (m/s) in the middle of the Section B1 (top) and close to the Asian coast on Section B1 (middle) and cross-strait velocity profiles in the middle of the Section B1 (bottom) for the year 2008.

etry. Linear change in depth of interface and the nonlinear change in the proximity of the constriction and southern exit is an evidence for strong mixing/ hydraulic jump inside the Bosphorus. Moreover, thinning of the bottom layer in the direction of the northern flank of the Bosphorus and the shape of isopycnal lines downstream of the northern sill reveals the impinged lower layer flow.

Measurements of volume transports through the Bosphorus and Dardanelles straits were conducted from September 2008 to February 2009 (*Jarosz et al., 2011a*). A comparison of these observations with the simulated transport time series is presented in Figure 6.13 and mean values are given in Table 6.1. The correlation coefficients between model and observations for the upper and lower layer and net volume transports

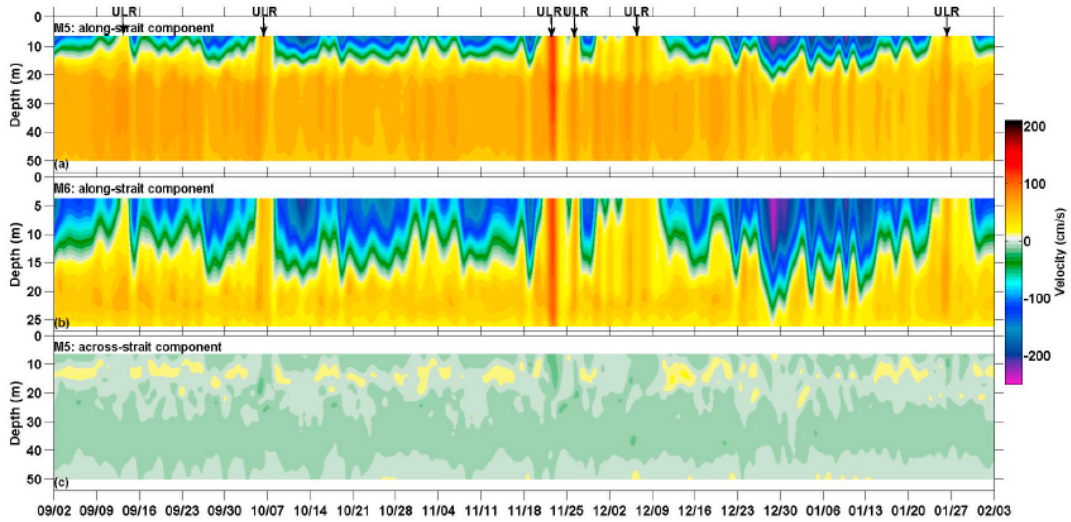


Figure 6.11: Observed along-strait velocity profiles (top and middle) and across-strait velocity profiles (bottom) in the same locations as described in Figure 6.10 for September to December 2008, taken from *Jarosz et al. (2011a)*.

through the northern Bosphorus are  $r_{upper}=0.84$ ,  $r_{lower}=0.78$  and  $r_{net}=0.81$ , respectively. These results reveal that the model is consistent with the measurements and able to capture the variability of the transport. Correlation coefficients for transports through the southern and northern exits of the Dardanelles and the northern end of the Bosphorus are presented in Table . The lowest correlation coefficient is obtained for the lower layer volume transport of the southern extremities of the Dardanelles ( $r=0.32$ ). The simulated net mean transport ( $97.7 \text{ km}^3/\text{yr}$ ) into the Marmara Sea compares relatively well with the observed net flux by *Jarosz et al. (2011a)* ( $86.3 \text{ km}^3/\text{yr}$ ). However, simulated upper layer and lower layer transports ( $254.1 \text{ km}^3/\text{yr}$  and  $147.4 \text{ km}^3/\text{yr}$ , respectively) are much lower than the observed transports ( $359.9 \text{ km}^3/\text{yr}$  and  $273.6 \text{ km}^3/\text{yr}$ , respectively) for the period Sep-Dec 2008. The simulated annual mean net transport is  $267.1 \text{ km}^3/\text{yr}$ , which is on the order of the value reported by *Ünlüata et al. (1990)* ( $300 \text{ km}^3/\text{yr}$ ). The amplitude of the model results is lower compared to measurements. The simulated net transport exhibits a standard deviation of  $166.4 \text{ km}^3/\text{yr}$ , whereas observations by *Jarosz et al. (2011a)* have a standard deviation of  $370.8 \text{ km}^3/\text{yr}$  for Sep-Dec 2008. This is probably due to the relatively coarse resolution of the atmospheric forcing and limited model domain in the Black and Aegean Seas.



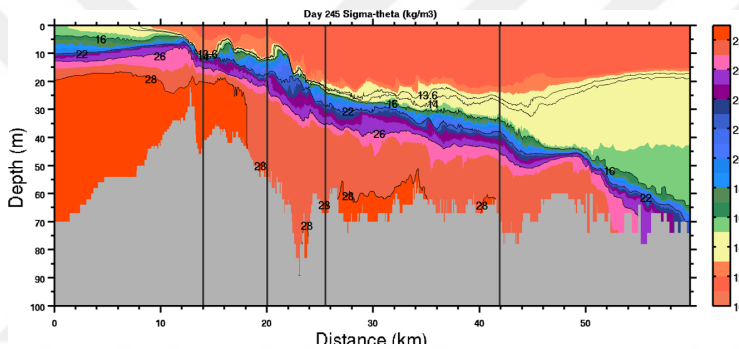
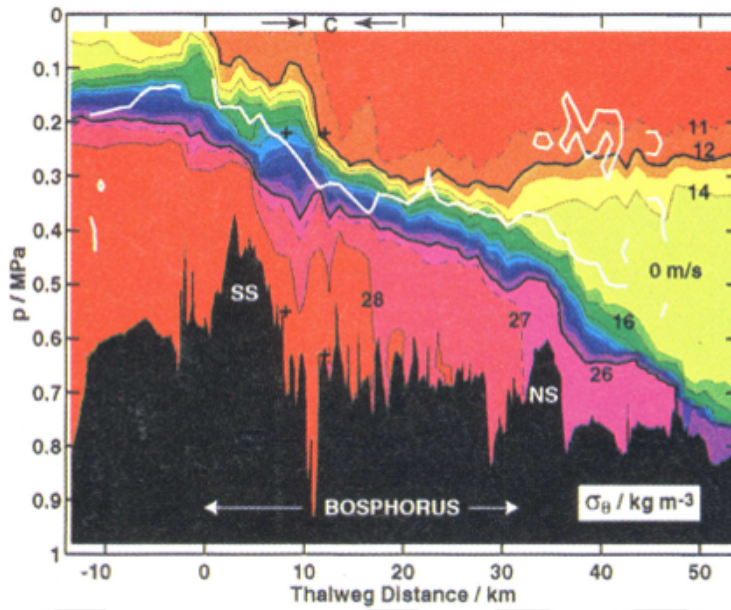


Figure 6.12: Thalweg section of potential density along the Bosphorus from observations in September 1994 (top panel) and from simulation BBInc in September 2008 (bottom panel).

### Blocking events

Under normal atmospheric conditions, there is a progressive decrease in the thickness of the upper layer starting from the northern end of the Bosphorus (45-50 m over the northern sill) until the Dardanelles-Aegean Sea Junction ( $\sim 10$  m). The upper layer thickness in the Marmara Sea is approximately 25 m. Strong northerly winds combined with higher sea-level difference between the Aegean and the Black Sea may deepen the interface position in the northern exit. This causes a blocking of the lower layer flow which can last a few days (termed "lower layer flow reversals", LLR). Conversely, strong southerly wind in combination with a decrease in sea level



Table 6.1: Average and standard deviation of simulated and observed (*Jarosz et al.*, 2011a) volume transports through the northern and southern cross strait sections of the Bosphorus and the Dardanelles for the period of September-December 2008.

	FEOM BBInc		<i>Jarosz et al.</i> (2011a)	
	UL mean/std	LL mean/std	UL mean/std	LLmean/std
Northern Bosp.	-352.0±131.5	84.9± 70.8	-359.7± 227.4	273.6± 144.7
Southern Bosp.	-401.6±158.4	128.2± 50.0	-420.4± 324.0	342.4± 115.9
Northern Dard.	-478.7±201.0	208.2± 130.0	-783.1± 501.2	573.0± 369.0
Southern Dard.	-648.5±221.9	361.6± 144.4	-1042.1± 528.7	1114.1± 457.7

Table 6.2: Correlation between simulated (experiment BBInc) and observed (*Jarosz et al.*, 2011a) volume transports through the northern and southern cross strait sections of the Bosphorus and the Dardanelles.

	Upper Layer	Lower Layer	Net
Northern Bosphorus	0.84	0.78	0.81
Southern Bosphorus	0.79	0.66	0.75
Northern Dardanelles	0.75	0.48	0.80
Southern Dardanelles	0.76	0.32	0.72

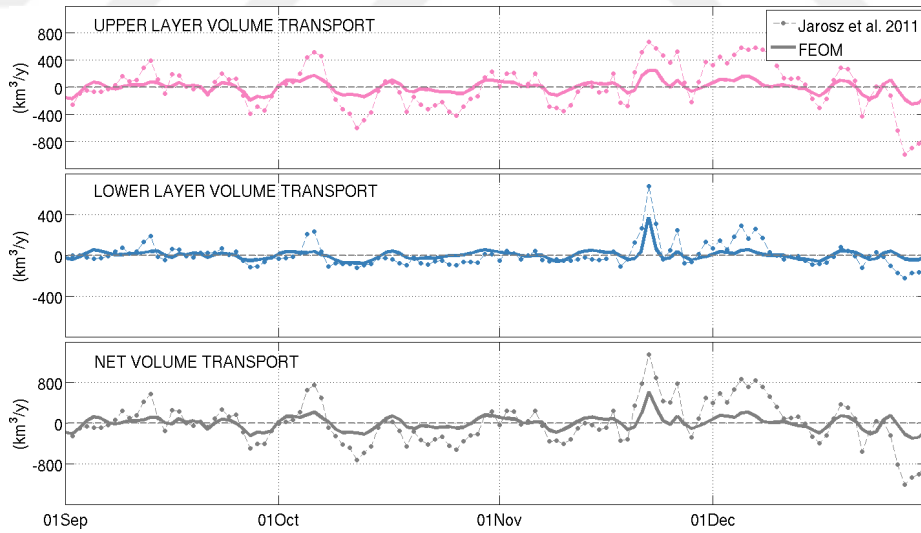


Figure 6.13: Timeseries of detrended simulated (solid line) and observed (dotted line) volume transport through the section B4 (Northern Bosphorus). Observations are from *Jarosz et al.* (2011a)

difference can arrest the surface layers and even reverse it for several days (termed "upper layer flow reversals", ULR, *Latif et al. (1991)* and *Jarosz et al. (2011a)*).

Such an upper layer blocking event occurred between November 21 and 22, 2008, and is well represented in the model (Figure 6.14, visible from latent and sensible heat fluxes), leading to a net northward flow through the Dardanelles and Bosphorus. For comparison, the simulated mean circulation averaged over November 2008 is shown as well. The currents on November 22, 2008 correspond to an atmospheric state characterized by strong southwesterly winds. There is a complete change in the flow direction as the upper layer is blocked and pushed backwards. In the Bosphorus, the currents suddenly exceed 1 m/s starting from the southern sill until the north of the contraction. The flow reversal even reaches to the Bosphorus-Black Sea Junction. A similar flow reversal is observed in the Dardanelles (lower panel). However there is a one-day time lag in between. The circulation in the Dardanelles even displays a channel-wide cyclonic recirculation cell in its southern exit.

During the year 2008, ECMWF data reveals that there are several strong storms (lasting 3-5 days) passing over the TSS region (Figure 4.4). Observations indicate several upper layer blocking events from September to December 2008 (Figure 6.11, *Jarosz et al. (2011a)*). The upper layer flow reversals observed during the periods 1-7 October 2008 and 20-22 November 2008 are clearly represented in the simulation (Figure 6.10). It should be noted that the lower layer is never reversed during the time period September to December 2008, neither in observations nor in the simulations.

### **6.2.1 The role of sea level**

Now, the relationship between sea level and volume transport through the Bosphorus is analyzed. The sea level difference between the Black Sea and the Aegean Sea is computed by evaluating the sea level in the red dots denoted by BS and AS shown in Figure 1.1 (Figure 6.15). The simulated mean sea level difference between these two points amounts to 29.6 cm, while *Alpar and Yüce (1998)* observed a sea level difference of 55 cm. A significant correlation is found between the sea level difference and transport through the southern Bosphorus ( $r = -0.87$ , Figure 6.15). Sea surface height can be split into a steric component and a bottom pressure component. The

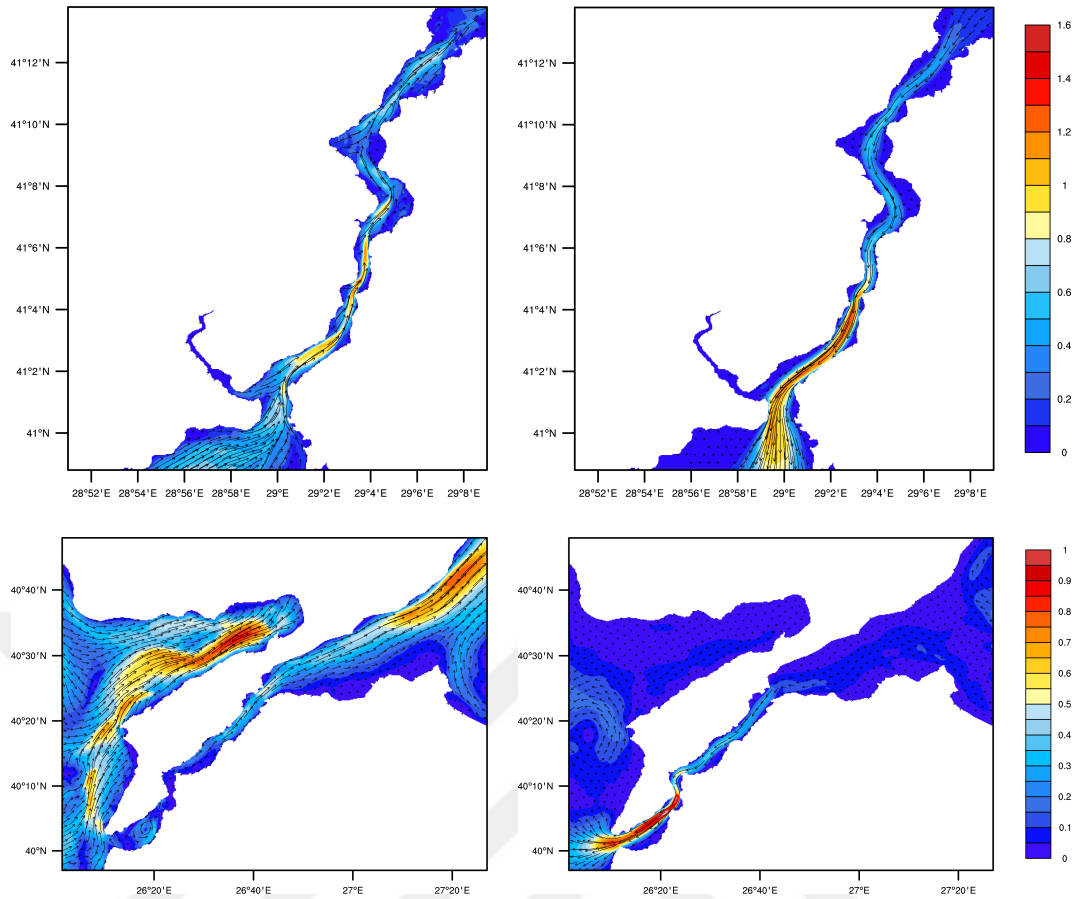


Figure 6.14: Simulated surface currents on November 21, 2008 in the Bosphorus (top left) and on November 20, 2008 in the Dardanelles (bottom left) and surface currents averaged over November 2008 (right).

correlation between the volume transport and the components of the SSH difference reveals that the bottom pressure is more important than the steric component ( $r_{steric} = 0.52$  and  $r_{bot-pres} = -0.86$ ). This is in agreement with the results presented by *Jarosz et al.* (2011a) and *Book et al.* (2014).

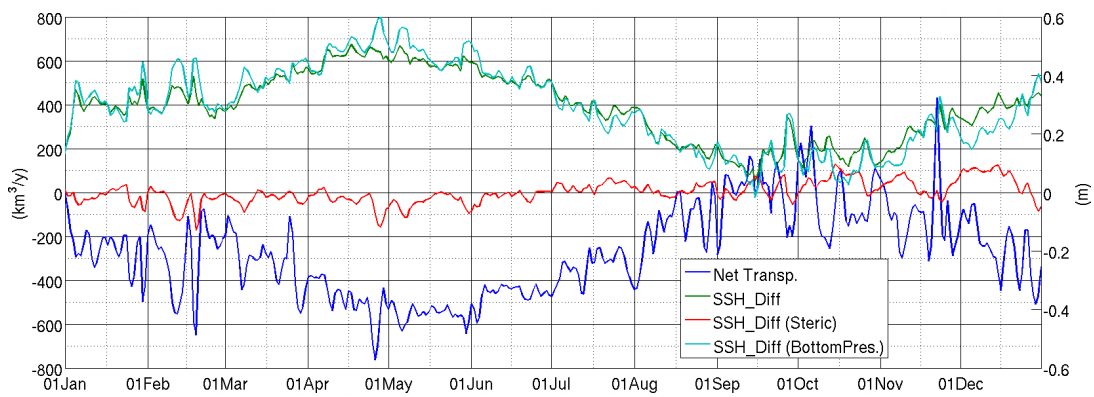


Figure 6.15: Net simulated transport through the Section A (blue) and sea surface height difference (green) between the Black and Aegean Seas and its steric (red) and bottom pressure components (cyan).

## CHAPTER 7

### DISCUSSION

The TSS model presented here produces consistent results with those described in the literature, but was different in one major respect: Previously, the response to the Black Sea inflow characteristics are artificially imposed as variations in volume fluxes or changes in tracer fields at the lateral boundaries of the Bosphorus (*Sözer, 2013*), the Dardanelles (*Kanarska and Maderich, 2008*) or in the Marmara Sea via highly idealized adjacent channels (*Demyshev et al., 2012; Chiggiato et al., 2012; Sannino et al., 2015*). The absence of the full geometry and topography does not permit these models to include the necessary physics (shear, mixing and entrainment) especially in the basin/channels they connect or near their junction zones. The model's temporal and spatial response to the Black Sea input variation is simulated in a coarse manner and is dependent strictly on the imposed boundary conditions. In FEOM-TSS model, the system is handled as a whole and the Black Sea freshwater budget is allowed freely to develop the volume fluxes through the Bosphorus. The boxes in the Black and Aegean Seas are used as adjustment zones to the initial disturbances before reaching the TSS as similar to the work in Mediterranean by *Tonani et al. (2008)*. One challenge of this modeling strategy is the limited size of the boxes that can impose artificial currents and sea surface elevation developing in both extremities of the straits that is further modified by the wind conditions over the region.

The remote sensing data from various satellites can be used to detect ocean color to visualize the circulation in the Marmara Sea (Figures 7.1 - 7.4). The waters of the Bosphorus and Dardanelles in the Marmara Sea can usually be easily identified because of large differences in their water properties.

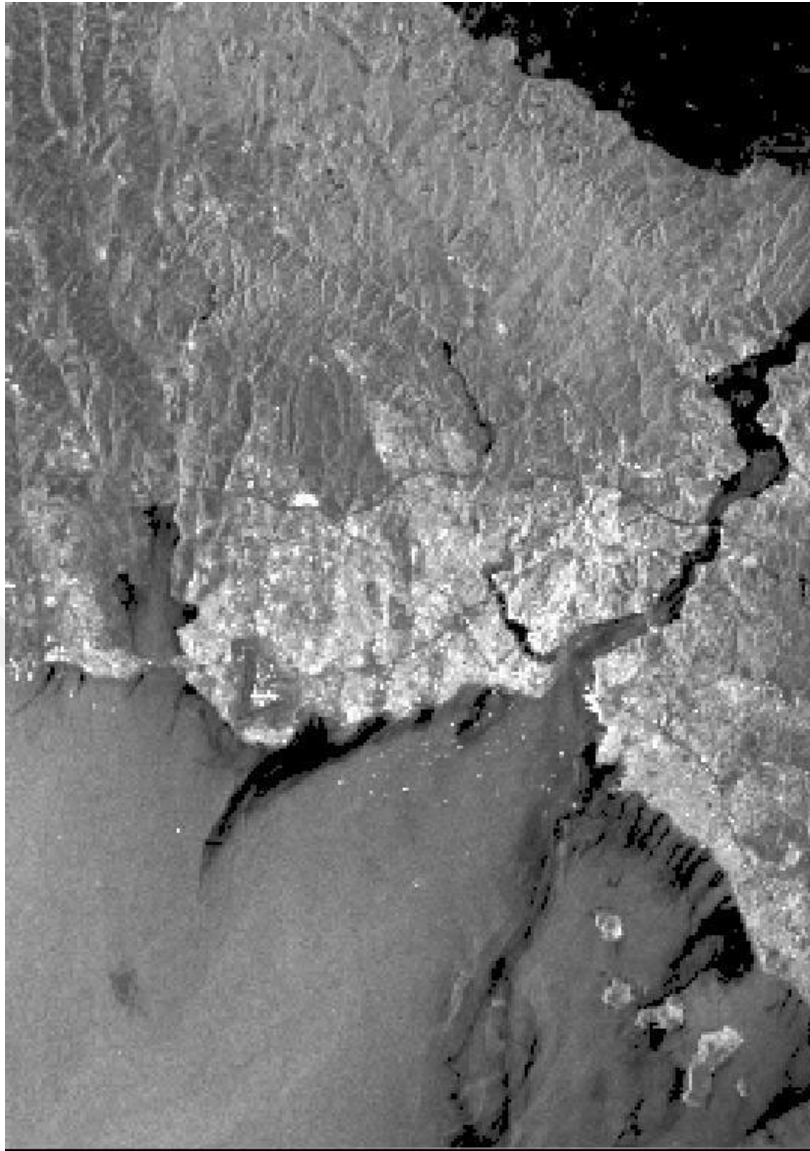


Figure 7.1: SAR (synthetic aperture radar) satellite image showing fine flow features near the Marmara exit of the Bosphorus Strait on May 29, 1995.

The SAR picture in Figure 7.1 shows a jet leaving the Bosphorus. The black patches and streaks extending in offshore direction are coastal discharges consisting of sewage and industrial waste from the city.

Recent Operational Land Imager on the Landsat 8 satellite captured this image of a phytoplankton bloom in the Sea of Marmara on May 17, 2015 (Figure 7.2). The swirling shapes on the water are the phytoplanktons, with the yellow-green and red-purple filaments likely representing different species. Those wavy colored lines not only show where the densest concentrations of plankton are floating, but also reveal

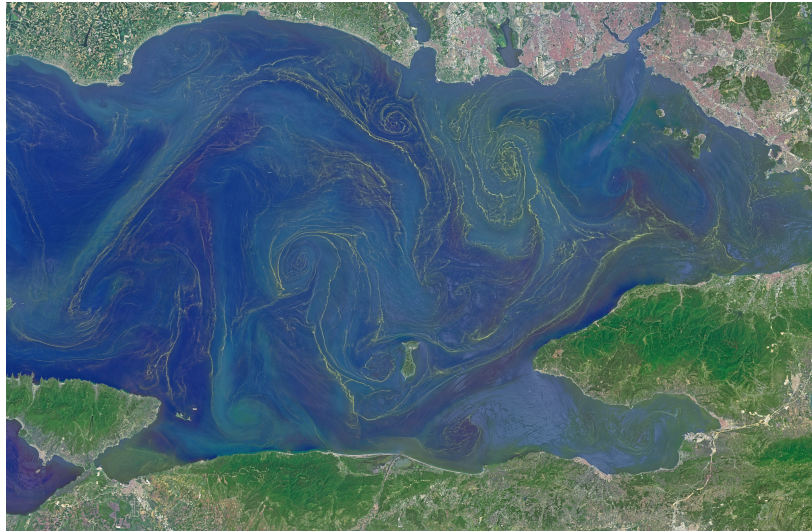


Figure 7.2: Landsat 8 satellite image showing the blooms in the Marmara Sea on May 17, 2015.

the eddies and currents within the small sea.



Figure 7.3: The Moderate Resolution Imaging Spectroradiometer (MODIS) on NASA's Terra satellite captured bloom events in the Sea of Marmara on May 23 (left) and May 25 (right), showing a coccolithophore bloom developed in the Turkish Straits System.

7.3 shows wider view of local bloom events observed in the Sea of Marmara by the Moderate Resolution Imaging Spectroradiometer (MODIS) on NASA's Terra satellite May 23 and May 25. The bright turquoise color in this image is typical for a bloom of the *Emiliana huxleyi*, coccolithophore species, known to occur in May-June in the Black Sea. Such a bloom typically follow is the earlier sequence of algae and dinoflagellate blooms, observed in the Black Sea. However, in this case it is purely a



local bloom of the Marmara Sea.



Figure 7.4: Aqua-MODIS recorded features in the Sea of Marmara on April 27, 2013 shows possible *Trichodesmium* blooms in the Turkish Straits System.

Aqua-MODIS recorded filamentous features in the Sea of Marmara on April 27th, 2013 (Figure 7.4). Features such as these have been identified in other satellite images as a result of *Trichodesmium* blooms. These cyanobacteria are not known to be native to the region, but a recent publication classify them as alien species in the Aegean Sea (*Çinar et al.*, 2011).

The formation of the FEOM-simulated Marmara Sea circulation is similar compared to drifter observations (*Gerin et al.*, 2013), satellite pictures (Figures 7.1 - 7.4) and the other modeling studies (*Demyshev and Dovgaya*, 2007; *Demyshev et al.*, 2012; *Chiggiato et al.*, 2012). Driven by the heat, salt, and momentum exchange through the Bosporus and Dardanelles straits with/without atmospheric forcing, the structure of the surface circulation field corresponds to an S-shaped jet directed from the Bosporus Strait to the Dardanelles and dividing the Marmara Sea into two regions. A mid-basin anticyclonic eddy is present in the Marmara Sea except strong wind conditions. Several small eddies are scattered around the S-shaped pathway.

The flow maintained a distinct two layer density character at all times in the TSS. Depth of the pycnocline and its oscillation under realistic atmospheric forcing in the Marmara Sea is studied by *Chiggiato et al.* (2012). Large amplitude variations under severe storms can cause up and downs in the position of the pycnocline and make it translate considerably in vertical. These findings can complement this work in a manner that the vertical position of the pycnocline depends not only the instantaneous meteorological changes but also the amount of water transported through the straits



hence the Black Sea freshwater input. In case of zero Black Sea freshwater inflow (the summation of evaporation, precipitation and runoff), the mean pycnocline level rises to the surface ( $\sim 2\text{m}$ ) and loses the seasonality on long term (Figure 6.9). This clearly is related to the net volume transport through the Bosphorus and Dardanelles and is bound to the density field through Knudsen relation. In other words, the salinity and temperature fields in the reservoirs determines the amount of the exchanged materials between them and in the end changes their own hydrographic properties. In BBExc case, low Bosphorus upper layer and higher Dardanelles bottom layer flows may be the reason for the rise of the interface towards the surface.

A sufficiently strong meteorological event as the storm over the Aegean Sea and Sea of Marmara was able to reverse the sea-level difference and hence the upper layer flow (Orkoz). This emphasizes the unpredictable character of the flow in the straits rather than the Marmara Sea. Upper layer flow reversal is generally expected to occur during the winter when the sea-level difference between the Black and the Aegean Seas is minimal. Starting on 22<sup>nd</sup> November, strong southwesterly winds caused the upper layers of the Dardanelles and the Bosphorus to be blocked and reversed in BBExc and BBInc cases when freshwater influx to the Black Sea are zero or very weak (namely, increase the sea-level difference between the Aegean and the Black Sea). Considering the bottom layers, for both hindcast simulations, the total blocking of the lower layer was not observed. However the conditions were very close to the blocking especially during the northwesterly storms in spring months. Correct initial conditions with multi-year model spin-up may give more accurate volume fluxes, basin averaged salinity and temperature values hence possibly bottom layer blocking in Bosphorus.

## **7.1 Impacts of inputs on the TSS exchange fluxes and Marmara Sea Ecosystem**

TSS is a buffer between two highly contrasting basins in terms of mean properties, fluxes of water and materials, and the structure of the ecosystems. It can sufficiently be revealed by this thesis only how complex are the exchanges through this system such as extreme gradients in water properties, mixing processes and negative buoyancy, nonlinear dynamics of various scales in the straits. Nevertheless, there are issues

requiring further study to obtain basic understanding of the underlying the biochemical transports and reactions, organism and human behavior that determine how the ecosystem responds to the complex environment in the Marmara Sea. The aspects of the ecosystem have not been sufficiently covered so far using a regional coupled ecosystem ocean model and await further efforts later.

The transport of sediments from a coastal site on the Black Sea entering directly into the Bosphorus and being injected into the Marmara Sea by the exiting jet are shown in Figure 7.1. Such transport of materials is not confined to sediments alone, but involves, nutrients, living matter and pollutants that are directly fed into the TSS from the Black Sea. The Bosphorus carries highly productive conditions of the Black Sea directly into the Marmara Sea, especially the coastal waters of the western Black Sea shelf. Furthermore, the Marmara Sea has its own biochemical cycle responding to nutrients fed from the Black Sea and by local mixing, leading to a further increase in production. In addition, there are many local land-based sources of pollution. The Metropolitan Area of Istanbul is the most important source, with other important sources located in the Izmit, Gemlik and Bandirma Bays and Tekirdağ area, and from small rivers such as the Susurluk carrying important agricultural loads. FEOM simulations show that under the weak wind conditions the areas of Izmit, Gemlik and Bandirma Bays are away from the influence of the inflow of the Bosphorus. In order to replenish the water in Izmit Bay, southwesterly winds are required especially.

Table 7.1 tabulates the estimates of the concentrations of inorganic nitrate and phosphate through the Bosphorus and Dardanelles Straits collected during 1990s (*Polat and Tuğrul, 1995*). The water fluxes and the measured concentrations of nutrients and isotopes permitted the calculation of the average nutrient fluxes through the TSS. In the Bosphorus Strait, the upper layer nitrate and phosphate concentration is high in winter and spring months and low in the rest of the year. Similarly, the nutrient fluxes in winter and spring are much greater than summer and autumn fluxes (Table 7.1), accounting for  $\sim 90\%$  of the annual nutrient fluxes into the Marmara Sea. In the lower layer of the Bosphorus, the nutrient concentrations and their fluxes are less variable throughout the year, but increases parallel to the volume fluxes (maximum values in spring and summer). The lower layer concentrations are  $\sim 10$  times and associated fluxes are 4-5 times greater than the surface fluxes of nutrients through the Bospho-

rus (Table 7.1). The Bosphorus lower layer plume mix with CIL waters and thus carry southwest Black Sea shelf water chemical materials to the upper subhalocline depths of the southwest Black Sea (Özsoy *et al.*, 2001; Stanev *et al.*, 2001). Analyses of Oxygen-18, deuterium and tritium (Rank *et al.*, 1998; Özsoy *et al.*, 2002) led us to estimate mixing ratios of the plume and CIL waters. Nutrient exchange fluxes in the straits vary markedly with season, due to changes in both the concentrations and volume fluxes (Polat and Tuğrul, 1995). The nutrient fluxes through the Dardanelles Strait upper layer shows similar behavior to the Bosphorus Strait (Table 7.1). They are high in winter and low in summer. The upper layer transport of nitrate and phosphate input to the Aegean Sea through the Dardanelles is greater than the Aegean input to Marmara (Polat and Tuğrul, 1995). The salty Mediterranean water of the lower layer enters from the Dardanelles Strait, with very low nitrate and phosphate concentration for most of the year though it is enriched by about 10-fold during its stay in the basin.

Table 7.1: Seasonal and annual fluxes of nitrate and phosphate exchanged between the adjacent seas through the Bosphorus and Dardanelles Straits for the period of 1990-2000 (after (Polat *et al.*, 1998; Tuğrul and Beşiktepe, 2007).

Flow Type	Season	Volume flux (*10 <sup>9</sup> m <sup>3</sup> )	Bosphorus				Dardanelles				
			NO3 conc. (mmole/m <sup>3</sup> )	NO3 flux (*10 <sup>8</sup> mol)	PO4 conc. (mmole/m <sup>3</sup> )	PO4 flux (*10 <sup>7</sup> mole)	NO3 conc. (mmole/m <sup>3</sup> )	NO3 flux (*10 <sup>8</sup> mol)	PO4 conc. (mmole/m <sup>3</sup> )	PO4 flux (*10 <sup>7</sup> mole)	
Upper	Spring	200	1,32	2,64	0,05	1	307	0,2	0,61	0,06	1,84
Upper	Summer	158	0,42	0,66	0,03	0,47	194	0,12	0,23	0,03	0,58
Upper	Autumn	105	0,22	0,23	0,05	0,52	142	0,3	0,42	0,05	0,71
Upper	Winter	145	3,2	4,64	0,14	2,03	234	0,36	0,84	0,09	2,1
Upper	Annual	608	1,29	8,17	0,07	4,02	877	0,24	2,1	0,06	5,23
Lower	Spring	94	9,17	8,62	0,92	8,65	202	1,14	2,3	0,05	1,01
Lower	Summer	76	10,46	7,95	0,99	7,52	112	0,47	0,53	0,03	0,34
Lower	Autumn	49	9,34	4,58	0,91	4,46	87	0,88	0,76	0,05	0,44
Lower	Winter	68	9,81	6,67	1,07	7,28	158	1,62	2,56	0,05	0,79
Lower	Annual	287	9,7	27,82	0,97	27,91	559	1,09	6,15	0,05	2,58

Material transport is directly related to the upper and lower transport in this two-layer system. Table 6.1 presents the upper and lower layer fluxes across the southern and northern Bosphorus. The results are almost half of the upper and lower layer volume fluxes presented in Table 7.1 having the same order of the net volume flux. The main discrepancy between the results are based on the consolidated model approach. The entire domain of the Black Sea is not included in the model. This is primarily because of demanding adjustment period. With time step 10s used, it would not be possible to spin-up the model for multiple years. Moreover, the Black Sea models generally suffers from the erosion of the CIL during interannual simulation. Before overcoming such challenges, it cannot be possible to model the entire Black Sea-Mediterranean Sea coupled system. Therefore, it can be expected that the amount

material transported to the Marmara Sea is lower than the values in Table 7.1.

In recent decades, despite the reduction in river runoff input into the Black Sea (Tolmazin, 1985), the increased Danube originated nutrient load is carried into the Marmara Sea via the surface flow of the the Bosphorus. Consequently, the organic matter production is enhanced near the surface of the Marmara Sea. This lead to lower light penetration and associated maximum depth of the euphotic zone. Consequently, the depth of the nutrient and dissolved oxygen gradient zones are changed in the Marmara Sea. Another notable factor that affects the ecology in the Marmara Sea is accumulation of the atmospheric deposition of the large amount of air pollutants as a result of heavily polluted urban areas located along the coastline. The nutrient contribution of atmosphere is an important subject particularly as a source of nitrogen entering into the Marmara Sea via the Mediterranean Sea (Kocak et al., 2004)



Figure 7.5: Red patches appeared on coastal band of Tekirdag in the Marmara Sea, which might be as a result of an increase in the population of probably dinoflagellates. courtesy: DHA; 2013, April 26.

The highly productive conditions of the western coastal Black Sea are directly reflected on the Marmara Sea. The living organic particle (phytoplankton) transport from the Black Sea to Marmara Sea has been documented in plankton studies carried out in the region (Uysal and Ünsal, 1996). In addition to that, the TSS is the only

route for the pelagic fishes migrating to the Black Sea in spring and returning to the north Aegean in autumn. These are either adversely influenced by, or in other cases may take advantage of, the various processes in their migration strategies. However, long-term changes of the oxycline has confined pelagic fish community to survive the oxygenated upper layer, leading to create pressure on fish ecosystem and migration between the adjacent seas through TSS. The timing of the migration is known with reasonable accuracy, however the hydrographic characteristics of the water masses determining the pathways of the migration is not known. Recent IMS-METU cruises made possible to access more fish data from the region to assess the changes in fish diversity and migrations through The TSS.

In conjunction with the dramatic changes in the Black Sea ecosystem via Bosphorus surface flow and increased direct input of both organic matter and inorganic nutrients through its coastline, the ecology of the Marmara Sea has significantly changed in the last few decades. Figure 7.5 exemplifies an extreme change of color in the surface layers of the Marmara Sea near Tekirdag which can be due to masses of dinoflagellates (the so-called red tides). Due to two layer structure, there are at least two different groups of marine organisms in the water column in the Sea of Marmara. In upper 20-25 m layer not only native fauna resides but also those belong to the Black Sea are continuously transported. This transport could be very important from time to time as in the case of western Atlantic originated ctenophore *Mnemiopsis leidyi* that disturbed the entire Black Sea ecosystem in the late 1980s and early 1990s. The bottom layer has Mediterranean fauna, but there may be some specifically adapted members of marine organisms, most notably of zooplankton and demersal fish community. Such water body structure (upper and lower) needs to sample separately to identify pelagic fauna and flora. The habitat diversity is not limited to vertical scale but also to spatial scale. There are diverse habitats in the Sea of Marmara and these regions are under variable effect of anthropogenic input.

Development of eutrophication conditions in the Marmara upper has not only altered the upper layer ecosystem but also the chemical properties of the subhalocline waters of Mediterranean origin. The Dardanelles under-current introduces the Aegean salty waters with almost saturated levels of dissolved oxygen but low values of nitrate and phosphate concentrations into the Marmara basin (*Polat and Tuğrul, 1995*). The sharp

halocline, separating the upper and lower layers of the Marmara Sea, also isolates the bottom layer from the atmosphere, essentially cutting off the supply of oxygen to this layer. Nevertheless, the input rate is still sufficient to prevent from developing anoxic conditions in the polluted Marmara (Özsoy *et al.*, 1986, 1988).

FEOM-simulated circulation and hydrographic fields under various scenarios can be a useful to track the eutrophication and associated mucilage events and their transport paths in the Marmara Sea in future. Moreover, the jellyfish transport paths and possible accumulation areas can be inferred from the model results. Moreover, the model results can be correlated with the data of migrating fishes detected acoustically. The depth of migrating schools and the hydrographic parameters of the migration depth can be further studied. These findings can help evaluating possible impacts of hydrographic changes (such as changes in the depth of oxycline or in the ecological state of the Black Sea and Mediterranean waters) on the pelagic fish and fishery that can update the Marine Policy in Turkey on long term.

## CHAPTER 8

### SUMMARY AND CONCLUSION

This dissertation describes the application of a finite element model (FEOM) with particularly enhanced resolution in the Bosphorus and Dardanelles to the topographically and bathymetrically complex region of the Turkish Straits System, where the Aegean Sea is linked to the Black Sea via the Sea of Marmara, connected by the Bosphorus and Dardanelles Straits. The narrow width of the straits combined with numerous shallow sills along their length render the finite element particularly suited to this type of application, capitalizing on the variable resolution that is possible with this type of model. This study emphasizes that although numerous modeling investigations have been previously undertaken, these studies were confined to specific parts of the system and undertaken under largely idealized conditions. In the first place, the benefits of using finite elements can be highlighted via the ability to model the system as a whole without necessitating any kind of nesting for sub-regions like other traditional ocean models do. Whilst the system is handled as a whole in this study, it also remains forced under largely idealized initial conditions. It is shown that the model is remarkable of reproducing main features of circulation and model characteristics are acknowledged to be consistent with previous modeling and observational studies summarized before. This included a two-layer flow system having fresh surface flow from the Black to Aegean Seas, with accompanying salty undercurrent in the opposite direction. The transit through the Sea of Marmara produces a quasi-stationary eddy with scale proportional of the sea itself, embedded in an S-shaped meandering flow. The model response was assessed to various parameter and forcing perturbations. Some of these experiments revealed the sensitivity of the model response to resolving the narrow straits. Finally two a year long simulations were presented that were

forced with realistic atmospheric forcing and were differ from each other in terms of the Black Sea freshwater fluxes. The best simulation (with the Black Sea freshwater budget) was compared to observational datasets collected over two months (April and October 2008). Besides, the volume fluxes through the Bosphorus and Dardanelles and their time variation are compared with the independent set of data.

The model domain is certainly challenging, and the application of the model appears both appropriate and sound. It can be gauged that the key message of this study is the quantification of the important driving mechanisms of the system. That is one of the unique scientific contributions this study is bringing. The study is structured in a way that the mean state of spin down experiment, i.e. the BASIC, whose solution should be comparable with the mean state of the fully forced system gives the system settings. The reference experiment, BASIC was initialized with a lock-exchange configuration, and spun down for three months. The qualitative agreement of BASIC with measurements is remarkable despite the missing forcing mechanisms such as winds, barometric pressure and net barotropic flow. The thickness and depth of the interface in the Bosphorus is well represented compared to observations (*Gregg and Özsoy, 2002*). However, the magnitude of upper (lower) layer transport through Bosphorus and Dardanelles does not correspond to observations given by *Ünlüata et al. (1990)*. The departure from this configuration is assessed through a series of sensitivity experiments which includes changes in mesh resolution, viscosity and diffusivity coefficients and wind forcing functions. The BASIC response and sensitivity experiments contain many qualitative assessments without involving the responsible underlying dynamical processes. Taking a big picture view after assimilating all the material presented, the reader can piece together key dynamic controls. The sensitivity studies may seem somewhat ill-conceived if key dynamic controls are to be uncovered, as many address numerical sensitivities of the modeling system rather than key contributing dynamic controls of the system such as sill depth or horizontal density gradient maintained by boundary relaxation. This issue has already been taken up by *Sözer (2013)* and not a novelty for this study and such tests are excluded. The horizontal resolution sensitivities are appropriate, since this demonstrates the effect of getting the flow in the straits correct (via adequately resolving them) on circulation in the Marmara Sea. Decreasing the horizontal resolution in the straits re-



duces the transports in each layer dramatically. Therefore, a reasonable compromise between resolution and computational cost should be provided. Sensitivities to vertical structure and horizontal mixing are seen to be less useful since modelers have a pretty good feel that decreased vertical resolution and increased horizontal mixing can degrade density gradients (via numerical and explicit diffusion respectively) that can lead to a suppression of baroclinic flow. These are sensitivities that are usually performed en route to an optimal calibration, and being of numerical nature don't really contribute to dynamic process understanding of the system. The wind sensitivity experiments reveal wind affects the solution; this is unsurprising, and to maintain a steady wind from one compass point for an extended period is also unrealistic, hence not quite relevant to system understanding.

Consequently, the influence of the fully forced system quantifies that it adequately validates to observation, then use this to investigate key dynamic controls. Two a-year long hindcast simulations were performed under realistic atmospheric forcing: one with and another one without considering the Black Sea freshwater budget (BBInc and BBExc). The simulation without the Black Sea freshwater forcing shows that the isopycnals in the Marmara Sea rise to the surface with time in the case of zero or very weak net volume transport through the Bosphorus. The remedy for this challenge comes with the consideration of the Black Sea water budget. Moreover, comparing the simulated surface circulation in the Marmara Sea in both experiments showed that it is dominated by the Bosphorus inflow which is maintained by the Black Sea runoff and modulated by the atmospheric forcing. The results were then compared with observed salinity and temperature CTD profiles in the Marmara Sea and transport measurements in the Bosphorus Straits. Including the Black Sea freshwater budget leads to a much better representation of the interface depth in the Marmara Sea compared to the simulation without including it. However, a surface salinity bias of about 2 psu is present in this simulation, requiring further model tuning in the future. The comparison with transport measurements in the Bosphorus revealed a very strong model skill in representing the variability and mean net transport, while upper layer and lower layer mean transport and standard deviation are lower than observed values.

The model-observation comparison revealed the significance of the Black Sea water budget and the atmospheric forcing. The stability of the depth of the interface in

the Marmara Sea is strongly coupled to the inflow from the Bosphorus. The model shows the isopycnals in the Marmara Sea rise to the surface with time in case of zero net volume transport through the Bosphorus. The sea surface elevation difference between the northern and the southern extremities of the TSS are only attained with the consideration of the Black Sea water budget. To summarize, barotropic forcing provides:

- net transport through the Bosphorus and the Dardanelles
- stability of the interface depth
- correct sea surface elevation difference between the Aegean and the Black Seas

The novelty in this study is that the model presented here includes all parts of the TSS due to the multi-resolution approach of the model. It has been shown that the key forcing functions, atmospheric and Black Sea freshwater forcing, are essential to provide a stable and realistic pycnocline depth in the Marmara Sea with correct seasonal cycle and improved variability and net transport through the Bosphorus. However, the model can be improved in several ways. (1) The comparison of transports revealed the significance of the atmospheric forcing on the high-frequency variability. In the simulations, a correction is applied to the sea points along the shore line to hinder the contamination of the land-based points in the ECMWF wind field. However, improvement in the FEOM simulations is possible by calling higher resolution wind-forcing data or using wind products from regional weather forecasting models such as Skiron (<http://openskiron.org/en/>). (2) So far, the choice for the initial and boundary conditions are idealized and the model set up is now ready to perform multi-year simulations with realistic initial conditions. (3) The current setup of the model shows a significant correlation between the sea level difference and transport through the southern Bosphorus ( $r = -0.87$ , not shown here). Sea surface height can be split into a steric component and a bottom pressure component. The correlation between the volume transport and the components of the SSH difference reveals that the bottom pressure is more important than the steric component ( $r_{steric} = 0.52$  and  $r_{bot-pres} = -0.86$ ). This is in agreement with the results presented by *Jarosz et al.* (2011a) and *Book et al.* (2014). The model domain should be extended to include the entire Black

and Mediterranean Seas to analyze the relationship between sea level and volume transport through the TSS.

The model assessment performed in this work revealed a faithful and physical reproduction of the circulation and mixing processes in the Marmara Sea and the Straits. The model set up is now ready to perform long term (few years) runs. This final goal within the current setting would help build the self-sufficient model system that could be evaluated and be adopted for operational use. The coupling to regional models of the Mediterranean and Black Seas would then be achieved with further confidence. It is foreseen that the artificial boundary conditions, Newtonian relaxation techniques and flux corrections can be continued to be used. The choices for other options for initial and boundary conditions, coupling and forcing are to be considered based on the evaluation of the above initial steps.

Mediterranean Sea and regional Aegean Sea numerical simulations add the diluting effect of Dardanelles outflow as diffusive river flow in order circumvent problems related to mass conservation (*Kourafalou and Tsiaras, 2007*). Three dimensional simulation of Dardanelles-North Aegean Junction with strait dynamics included reveal variability in the region and water mass distribution over the North Aegean. The impact of the North Aegean Sea on East Mediterranean Transient (EMT) is already known (*Zervakis et al., 2000, 2004*). The indirect role of the Black Sea on EMT will be an interesting subject for further research.



## Bibliography

- Adcroft, A., and D. Marshall (1998), How slippery are piecewise-constant coastlines in numerical ocean models?, *Tellus, Ser A. and Ser. B-Dyn. Meteorol. Oceanogr.*, 50, 95–108.
- Akten, N. (2004), Analysis of Shipping Casualties in the Bosphorus, *J. Navigation*, 57, 345–356.
- Alpar, B., and H. Yüce (1998), Sea-level variations and their interactions between the Black Sea and the Aegean Sea, *Estuar. Coast. Shelf S.*, 46, 609–619.
- Altiok, H. (2010), Temperature, Salinity and Flow Variations in the Strait of Istanbul (Bosphorus), in *2010-Rapp. Comm. Int. Mer Medit.*, vol. 39, p. 85, CIESM: Mediterranean Science Commission, Monaco, CIESM Congress, Venice (2010).
- Andersen, S., F. Jakobsen, and B. Alpar (1997), The water level in the Bosphorus Strait and its dependence on atmospheric forcing, *Deutsche Hydrographische Zeitschrift*, 49, 466–475.
- Androulidakis, Y. S., and V. H. Kourafalou (2011), Evolution of a buoyant outflow in the presence of complex topography: The Çanakkale plume (North Aegean Sea), *J. Geophys. Res. Oceans*, 116, C04,019, doi:10.1029/2010JC006316.
- Androulidakis, Y. S., Y. Krestenitis, and V. H. Kourafalou (2012), Connectivity of north Aegean circulation to the Black sea water budget, *Cont. Shelf Res.*, 48, 8–26.
- Armi, L., and D. Farmer (1987), A generalization of the concept of maximal exchange in a strait, *J. Geophys. Res.*, 92, 14,679–14,680.
- Aydoğan, B., B. Ayat, M. N. Öztürk, E. Ö. Çevik, and Y. Yüksel (2010), Current velocity Forecasting in Straits with Artificial Neural Networks, a Case Study: Strait of İstanbul, *Ocean Eng.*, 37, 443–453.

- Babuška, I. (1973), The finite element method with Lagrangian multipliers, *Numerische Mathematik*, 20, 179–192.
- Beşiktepe, Ş. T. (2003), Density currents in the two-layer flow: an example of Dardanelles outflow, *Oceanol. Acta*, 26, 243–253.
- Beşiktepe, Ş. T., E. Özsoy, and Ü. Ünlüata (1993), Filling of the Sea of Marmara by the Dardanelles lower layer inflow, *Deep-Sea Res.*, 40, 1815–1838.
- Beşiktepe, Ş. T., H. I. Sur, E. Özsoy, M. A. Latif, T. Oğuz, and Ü. Ünlüata (1994), The circulation and hydrography of the Marmara Sea, *Prog. Oceanogr.*, 34, 285–334.
- Bignami, F., S. Marullo, R. Santoleri, and M. E. Schiano (1995), Long wave radiation budget on the Mediterranean Sea, *J. Geophys. Res.*, 100, 2501–2514.
- Bogdanova, A. K. (1961), The distribution of Mediterranean waters in the Black Sea, *Okeanologiya*, 1, 983–991.
- Bogdanova, A. K. (1965), Seasonal fluctuations and distribution of the Mediterranean waters of the Black Sea. Basic features, geological structure of the hydrologic regime and biology of the Mediterranean Sea., Academy of Sciences, U.S.S.R., Moscow Eng. translation, 1960, Institute of Modern Languages, Washington D.C.
- Book, J. W., E. Jarosz, J. Chiggiato, and Ş. Beşiktepe (2014), The oceanic response of the Turkish Straits System to an extreme drop in atmospheric pressure, *J. Geophys. Res. Oceans*, 119, 3629–3644.
- Brezzi, F. (1974), On the existence, uniqueness and approximation of saddle-point problems arising from Lagrangian multipliers. *Revue française d'automatique informatique recherche operationnelle, Analyse Numérique*, 8, 129–151.
- Büyükay, M. (1989), The surface and internal oscillations the bosphorus related to the meteorological forces, Master's thesis, Middle East Technical University.
- Büyüközden, A., H. Yüce, and T. S. Bayraktar (1983), Temperature, salinity, density (sigma-t) variations along the Strait of Istanbul, *Tech. rep.*, TUBITAK Çevre Arastirmalari Grubu.
- Çetin, N. (1999), Analysis of the exchange flow through the bosphorus strait, Master's thesis, Middle East Technical University.

- Chiggiato, J., E. Jarosz, J. W. Book, J. Dykes, L. Torrisi, P. M. Poulain, R. Gerin, J. Horstmann, and Ş. Beşiktepe (2012), Dynamics of the circulation in the Sea of Marmara: Numerical modeling experiment and observations from the Turkish strait system experiment, *Ocean Dynam.*, 62, 139–159.
- Çinar, M. E., M. Bilecenoğlu, B. Öztürk, T. Katağan, M. B. Yokeş, V. Aysel, E. Dagli, S. Açıık, T. Özcan, and H. Erdoğan (2011), An updated review of alien species on the coasts of Turkey, *Medit. Mar. Sci.*, 12, 257–315.
- Codina, R., and O. Soto (1997), Finite element solution of the Stokes problem with dominating Coriolis force, *Comput. Meth. Appl. Mech. Engng.*, 142, 215–234.
- Codina, R., and O. C. Zienkiewicz (2002), CBS versus GLS stabilization of the incompressible Navier-Stokes equations and the role of the time step as stabilization parameter, *Commun. Numer. Methods Eng.*, 18, 99–112.
- Danilov, S., G. Kivman, and J. Schröter (2004), A finite-element ocean model: principles and evaluation, *Ocean Model.*, 6(2), 125–150.
- Danilov, S., Q. Wang, M. Losch, D. Sidorenko, and J. Schröter (2008), Modeling ocean circulation on unstructured meshes: comparison of two horizontal discretizations, *Ocean Dynam.*, 58(5-6), 365–374.
- De Filippi, G. L., L. Iovenitti, and A. Akyarlı (1989), Current analysis in the Marmara-Bosphorus Junction, 1st AIOM (Associazione di Ingegneria Offshore e Marina) Congress, Venice.
- Defant, A. (1961), *Physical Oceanography*, 729 pp., Pergamon Press, Oxford.
- Demyshev, S. G., and S. V. Dovgaya (2007), Numerical Experiment aimed at modeling the hydrophysical fields in the Sea of Marmara with regard for Bosphorus and Dardanelles, *Physical Oceanography*, 17, 141–153.
- Demyshev, S. G., S. V. Dovgaya, and V. A. Ivanov (2012), Numerical modeling of the influence of exchange through the Bosphorus and Dardanelles Straits on the hydrophysical fields of the Marmara Sea, *Atmospheric and Oceanic Physics*, 48, 418–426.

- Dupont, F., D. N. Straub, and C. A. Lin (2003), Influence of a step-like coastline on the basin scale vorticity budget of mid-latitude gyre models, *Tellus, Ser. A-Dyn. Meteorol. Oceanogr.*, 55, 255–272.
- Ergin, M., M. N. Bodur, D. Ediger, V. Ediger, and A. Yılmaz (1993), Organic carbon distribution in the surface sediments of the Sea of Marmara and its control by the inflow by adjacent water masses, *Marine Chemistry*, 41, 311–326.
- Farmer, D. M., and L. Armi (1986), Maximal two-layer exchange over a sill and through the combination of a sill and contraction with barotropic flow, *J. Fluid Mech.*, 164, 53–76.
- Gerin, R., P.-M. Poulain, Ş. T. Beşiktepe, and P. Zanasca (2013), On the surface circulation of the Marmara Sea as deduced from drifters, *Turkish Journal of Earth Sciences*, 22(6).
- Gökaşan, E., H. Tur, B. Ecevitoglu, T. Görüm, A. Türker, B. Tok, F. Çağlak, H. Birkan, and M. Şimşek (2005), Evidence and implications of massive erosion along the Strait of İstanbul (Bosphorus), *Geo-Mar. Lett.*, 25, 324–342.
- Gökaşan, E., M. Ergin, M. Özyalvaç, H. I. Sur, H. Tur, T. Görüm, T. Ustaömer, F. G. Batuk, H. Alp, H. Birkan, A. Türker, E. Gezgin, and M. Özturan (2007), Factors controlling the morphological evolution of the Çanakkale Strait (Dardanelles, Turkey), *Geo-Mar. Lett.*, 28, 107–129.
- Gregg, C. M., and E. Özsoy (1999), Mixing on the Black Sea Shelf North of the Bosphorus, *Geophys. Res. Lett.*, 26, 1869–1872.
- Gregg, C. M., and E. Özsoy (2002), Flow, water mass changes and hydraulics in the Bosphorus, *J. Geophys. Res.*, 107, 3016.
- Gregg, C. M., E. Özsoy, and M. A. Latif (1999), Quasi-steady exchange flow in the Bosphorus, *Geophys. Res. Lett.*, 26, 83–86.
- Griffies, S. M. (2004), *Fundamentals of Ocean Climate Models*, 250–263 pp., Princeton University Press, Princeton, NJ.



- Griffies, S. M., and R. W. Hallberg (2000), Biharmonic friction with a Smagorinsky-like viscosity for use in large-scale eddy-permitting ocean models, *Mon. Weather Rev.*, *128*, 2935–2946.
- Griffies, S. M., A. Gnanadesikan, R. C. Pacanowski, V. D. Larichev, J. K. Dukowicz, and R. D. Smith (1998), Isonutral diffusion in a z-coordinate ocean model, *J. Phys. Oceanogr.*, *28*, 805–830.
- Gündüz, C., and E. Özsoy (2015), Blocking of the upper layer flow in the Çanakkale (Dardanelles) Strait and its influence on fish catches, *J. Black Sea/Mediterranean Environment*, *21*, 99–115.
- Gunnerson, C. G., and E. Özturgut (1974), The Bosphorus. In: The Black Sea-Geology, Chemistry, and Biology (eds. Degens, ET and Ross, DA), *Amer. Asso. Petrol Geol. Mem.*, *20*, 99–115.
- Hüsrevoğlu, Y. S. (1999), Modelling of the dardanelles strait lower-layer flow into the marmara sea, Master's thesis, Middle East Technical University.
- Ilıcak, M., T. M. Özgökmen, E. Özsoy, and P. F. Fischer (2009), Flow, water mass changes and hydraulics in the Bosphorus, *Ocean Model.*, *29*, 159–175.
- Jackett, D., and T. Mcdougall (1995), Minimal Adjustment of Hydrographic Profiles to Achieve Static Stability, *J. Atmos. Oceanic Technol.*, *12*, 381–389, doi:10.1175/1520-0426(1995)012<0381:MAOHPT>2.0.CO;2.
- Jarosz, E., W. J. Teague, J. W. Book, and Ş. T. Beşiktepe (2011a), On flow variability in the Bosphorus Strait, *J. Geophys. Res.*, *116*, C08,038, doi:10.1029/2010JC006861.
- Jarosz, E., W. J. Teague, J. W. Book, and Ş. T. Beşiktepe (2011b), Observed volume fluxes in the Bosphorus Strait, *J. Geophys. Res.*, *38*, L21,608, doi:10.1029/2011GL049557.
- Jarosz, E., W. J. Teague, J. W. Book, and Ş. T. Beşiktepe (2012), Observations on the characteristics of the exchange flow in the Dardanelles Strait, *J. Geophys. Res.*, *117*, C11,012.

- Johns, B., and T. Oğuz (1989), The modelling of the flow of water through the Bosphorus, *Dyn. Atm. and Oceans.*, 14, 229–258.
- Kanarska, G., and M. Maderich (2008), Modeling of seasonal exchange flows through the Dardanelles Strait, *Estuar. Coast. Shelf S.*, 79, 449–458.
- Kara, A. B., A. J. Wallcraft, and H. E. Hulburt (2007), A Correction for Land Contamination of Atmospheric Variables near Land–Sea Boundaries, *J. Phys. Oceanogr.*, 37, 803–818.
- Kara, A. B., A. J. Wallcraft, H. E. Hulburt, and E. V. Stanev (2008), Air-sea fluxes and river discharges in the Black Sea with a focus on the Danube and Bosphorus, *J. Mar. Sys.*, 74, 74–95.
- Kondo, J. (1975), Air-Sea bulk transfer coefficients in diabatic condition, *Boundary Layer Meteorol.*, 9, 91–112.
- Kourafalou, V. H., and K. P. Tsiaras (2007), A nested circulation model for the North Aegean Sea, *Ocean Sci.*, 3, 1–16.
- Ladyzhenskaya, O. A. (1969), *The mathematical theory of viscous incompressible flow*, Gordon and Breach, New York.
- Latif, M. A., E. Özsoy, T. Oğuz, and Ü. Ünlüata (1991), Observations of the Mediterranean inflow into the Black Sea, *Deep-Sea Res.*, 38, S711–S723.
- Le Roux, D. Y., A. Staniforth, and C. A. Lin (1998), Finite elements for shallow-water equation ocean models, *Monthly Weather Review*, 126, 1931–1951.
- Löhner, R., K. Morgan, J. Peraire, and M. Vahdati (1987), Finite elements for shallow-water equation ocean models, *Int. J. Num. Meth. Fluids*, 126, 1093–1109.
- Lowe, P. R. (1977), An approximating polynomial for the computation of saturation vapor pressure, *J. Appl. Meteor.*, 16, 100–103.
- Maderich, V., and S. Konstantinov (2002), Seasonal dynamics of the system sea-strait: Black Sea-Bosphorus case study, *Estuar. Coast. Shelf S.*, 51, 183–196.
- Makarov, S. O. (1885), On water exchange between the Black Sea and the Mediterranean, *Appendix to Zapiski Imperatorskoy Akademi Nauk (Proceeding of Imperial Academy of Sciences)*, 31, 175.

- Marsigli, L. F. (1681), Internal observations on the Thracian Bosphorus, or true channel of Constantinople, presented in letters to Her Majesty, Queen Christina of Sweden, in *Internal observations on the Thracian Bosphorus, or true channel of Constantinople, presented in letters to Her Majesty, Queen Christina of Sweden*, vol. 11, pp. 734—758.
- Möller, L. (1928), Alfred Merz hydrographische Untersuchungen in Bosphorus und Dardanellen, in *Alfred Merz hydrographische Untersuchungen in Bosphorus und Dardanellen*, vol. Neue Folge A, pp. 3–284, Veröffentlichungen des Instituts für Meereskunde an der Universitaet Berlin.
- Nielsen, J. N. (1912), Hydrography of the Mediterranean and adjacent waters, In: *J. Schmidt (Ed.) Report of the Danish oceanographic expedition 1908–1910 to the Mediterranean and adjacent waters., 1*, 72—191.
- Oğuz, T. (2005), Hydraulic adjustments of the Bosphorus exchange flow, *Geophys. Res. Lett.*, 32, L06,604.
- Oğuz, T., and H. I. Sur (1989), A two-layer model of water exchange through the Dardanelles Strait, *Oceanol. Acta*, 12, 23–31.
- Oğuz, T., E. Özsoy, M. A. Latif, H. I. Sur, and Ü. Ünlüata (1990), Modeling of Hydraulically Controlled Exchange Flow in the Bosphorus Strait, *J. Phys. Oceanogr.*, 20, 945–965.
- Özsoy, E., and Ü. Ünlüata (1997), Oceanography of the Black Sea: a review of some recent results, *Earth-Science Reviews*, 42, 231–272.
- Özsoy, E., T. Oğuz, M. A. Latif, and Ü. Ünlüata (1986), Oceanography of the Turkish Straits, *Tech. Rep. 1*, Institute of Marine Sciences, Middle East Technical University.
- Özsoy, E., T. Oğuz, M. A. Latif, Ü. Ünlüata, H. I. Sur, and Ş. T. Beşiktepe (1988), Oceanography of the Turkish Straits, *Tech. Rep. 2*, Institute of Marine Sciences, Middle East Technical University.
- Özsoy, E., D. D. Iorio, M. Gregg, and J. Backhaus (2001), Mixing in the Bosphorus Strait and the Black Sea Continental Shelf: Observations and a Model of the Dense Water Outflow, *J. Mar. Sys.*, 31, 99–135.

- Özsoy, E., D. Rank, and I. Salihoğlu (2002), Pycnocline and Deep Vertical Mixing in the Black Sea: Stable Isotope and Transient Tracer Measurements, *Est. Coastal and Shelf Sci.*, 54, 621–629.
- Öztürk, M., B. Avat, B. Aydoğan, and Y. Yüksel (2012), 3D Numerical Modeling of Stratified Flows: Case Study of the Bosphorus Strait, *J. Waterway, Port, Coastal, Ocean Eng.*, 138, 406–419.
- Pacanowski, R., and S. Philander (1981), Parameterization of Vertical Mixing in Numerical Models of Tropical Oceans, *J. Geophys. Res.*, 11, 1443–1451.
- Payne, R. E. (1972), Albedo of the sea surface, *J. Atmos. Sci.*, 29, 959–970.
- Pektaş, H. (1953), Surface currents in the Bosphorus and the Sea of Marmara, *Publication of the Hydrobiology Research Institute, Faculty of Science, University of Istanbul, Hydrobiology Series*, 4, 154–169.
- Peneva, E., E. Stanev, V. Belokopytov, and P. Y. L. Traon (2001), Water transport in the Bosphorus Strait estimated from hydro-meteorological and altimeter data: Seasonal and decadal variability, *J. Mar. Syst.*, 31, 21–33.
- Persson, P. O., and G. Strang (2004), A Simple Mesh Generator in MATLAB, *Siam Rev.*, 46(2), 329–345.
- Pettenuzzo, D., W. G. Large, and N. Pinardi (2010), On the corrections of ERA-40 surface flux products consistent with the Mediterranean heat and water budgets and the connection between basin surface total heat flux and NAO, *J. Geophys. Res.*, 115, C06,022.
- Polat, Ç., and S. Tuğrul (1995), Nutrient and Organic Carbon Exchanges between the Black and Marmara Seas through the Bosphorus Strait, *Cont. Shelf Res.*, 15, 1115–1132.
- Polat, Ç., S. Tuğrul, Y. Çoban, O. Baştürk, and I. Salihoglu (1998), Elemental Composition of Seston and Nutrient Dynamics in the Sea of Marmara, *Hydrobiologia*, 363, 157–167.
- Poulos, S. E., P. G. Drakopoulos, and M. B. Collins (1997), Seasonal variability in sea

- surface oceanographic conditions in the Aegean Sea (Eastern Mediterranean): An overview, *J. Mar. Syst.*, *13*, 225–244.
- Rank, D., E. Özsoy, and I. Salihoğlu (1998), Deuterium and Tritium in the Black Sea and the Sea of Marmara, *J. Env. Rad.*, *43*, 231–245.
- Reed, R. K. (1977), On estimating insolation over the ocean, *J. Phys. Oceanogr.*, *7*, 482–485.
- Rosati, A., and K. Miyakoda (1988), A general circulation model for upper ocean simulation, *J. Phys. Oceanogr.*, *18*, 1601–1626.
- Sannino, G., A. Sözer, and E. Özsoy (2015), A High-Resolution Modelling Study of the Turkish Straits System, *Ocean Dynam.*, (submitted).
- Shchepetkin, A. F., and J. C. McWilliams (2005), The regional oceanic modeling system (ROMS): a split-explicit, free-surface, topography-following-coordinate oceanic model, *Ocean Model.*, *9*, 347–404.
- Shewchuk, J. (1996), Triangle: Engineering a 2D Quality Mesh Generator And Delaunay Triangulator, *Applied Computational Geometry Towards Geometric Engineering*, pp. 203–222.
- Sidorenko, D., Q. Wang, S. Danilov, and J. Schröter (2011), FESOM under Coordinated Ocean-ice Reference Experiment forcing, *Ocean Dynam.*, *61*, 881–890, doi:10.1007/s10236-011-0406-7.
- Sidorenko, D., T. Rackow, T. Jung, T. Semmler, D. Barbi, S. Danilov, K. Dethloff, W. Dorn, K. Fieg, H. F. Gößling, D. Handorf, S. Harig, W. Hiller, S. Juricke, M. Losch, J. Schröter, D. V. Sein, and Q. Wang (2015), Towards multi-resolution global climate modeling with ECHAM6–FESOM. Part I: model formulation and mean climate, *Ocean Dynam.*, *44*, 757–780, doi:10.1007/s00382-014-2290-6.
- Sözer, A. (2013), Numerical modeling of the bosphorus exchange flow dynamics, Ph.D. thesis, Middle East Technical University.
- Sözer, A., and E. Özsoy (2002), A three-dimensional model of bosphorus strait dynamics, in *A Three-Dimensional model of Bosphorus Strait Dynamics*, no. 2 in The

- 2nd Meeting on the Physical Oceanography of Sea Straits, pp. 207—210, Villefranche.
- Stanev, E. V., and E. L. Peneva (2002), Regional sea level response to global climatic change: Black Sea examples, *Global Planet. Change*, 32, 33—47.
- Stanev, E. V., J. A. Simeonov, and E. L. Peneva (2001), Ventilation of Black Sea Pycnocline by the Mediterranean plume, *J. Mar. Sys.*, 31, 77—97.
- Staschuk, N., and K. Hutter (2001), Modelling of water exchange through the Strait of Dardanelles, *Cont. Shelf Res.*, 21, 1361—1382.
- Sümer, B. M., and M. Bakıoğlu (1981), Sea strait flow with special reference to Bosphorus, *Tech. rep.*, Faculty of Civil Engineering, Istanbul Technical University.
- Timmermann, R., S. Danilov, J. Schröter, C. Böning, D. Sidorenko, and K. Rollenhagen (2009), Ocean circulation and sea ice distribution in a finite element global sea ice-ocean model, *Ocean Model.*, 27(3-4), 114–129.
- Tolmazin, D. (1985), Changing Coastal Oceanography of the Black Sea. II. Mediterranean Effluent, *Prog. Oceanog.*, 15, 277–313.
- Tonani, M., N. Pinardi, S. Dobricic, I. Pujol, and C. Fratianni (2008), A high-resolution free-surface model of the Mediterranean Sea, *Ocean Sci.*, 4, 1–14.
- Tuğrul, S., and Ş. T. Beşiktepe (2007), Nutrient exchange fluxes between the Black Sea and Mediterranean through the Turkish Strait System (Marmara Sea, Bosphorus and Dardanelles), in *CIESM*, CIESM Congress, Istanbul.
- Tuğrul, S., Ş. T. Beşiktepe, and I. Salihoğlu (1946), The hydrography of the Bosphorus: An introduction, *Geog. Rev.*, 36, 44–60.
- Tuğrul, S., Ş. T. Beşiktepe, and I. Salihoğlu (2002), Nutrient exchange fluxes between the Aegean and Black Seas through the Marmara Sea, *Mediterr. Mar. Sci.*, 3, 33–42.
- Ünlüata, Ü., and T. Oğuz (1983), A review of the dynamical aspects of the Bosphorus, NATO Workshop on the Atmospheric and Oceanic Circulation of the Mediterranean, La Spezia, Italy, Sept.

- Ünlüata, Ü., T. Oğuz, M. A. Latif, and E. Özsoy (1990), On the physical oceanography of the Turkish Straits, in *Physical Oceanography of the Sea Straits*, edited by L. J. Pratt, pp. 43–64, NATO/ ASI Series, Kluwer Academic Publishers, Dordrecht.
- Uysal, Z., and M. Ünsal (1996), Spatial distribution of net diatoms along adjacent water masses of different origin, *Turkish Journal of Botany.*, *20*, 519–525.
- Wallcraft, A. J., A. B. Kara, and H. E. Hurlburt (2005), Convergence of Laplacian diffusion versus resolution of an ocean model, *J. Geophys. Res.*, *32*, L07,604.
- Wang, Q., S. Danilov, and J. Schröter (2008), Finite element ocean circulation model based on triangular prismatic elements, with application in studying the effect of topography representation, *J. Geophys. Res.*, *113*(C05015), doi:10.1029/2007JC004482.
- Wang, Q., P. Myers, X. Hu, and A. Bush (2012), Flow constraints on pathways through the Canadian Arctic Archipelago, *Atm.-Oce.*, doi:10.1080/07055900.2012.704348.
- Wang, Q., S. Danilov, D. Sidorenko, R. Timmermann, C. Wekerle, X. Wang, T. Jung, and J. Schröter (2014), The finite element sea ice-ocean model (FESOM) v.1.4: formulation and ocean general circulation model, *Geosci. Model Dev.*, *7*, 663–693.
- Wekerle, C., Q. Wang, S. Danilov, T. Jung, and J. Schröter (2013), Freshwater transport through the Canadian Arctic Archipelago in a multi-resolution global model: model assessment and the driving mechanism of interannual variability, *J. Geophys. Res.*, *118*, 4525–4541.
- Wessel, P., W. H. F. Smith, R. Scharroo, J. F. Luis, and F. Wobbe (2013), Generic Mapping Tools: Improved Version Released, *EOS Trans. AGU*, *94*, 409–410.
- Wharton, W. J. L. (1872), Reports on currents of the Dardanelles and Bosphorus, *Tech. Rep. 20*, Hydrographic Office Admiralty.
- Yüce, H. (1990), Investigation of the Mediterranean water in the Strait of Istanbul (Bosphorus) and the Black Sea, *Oceanol. Acta*, *13*, 177–186.
- Yüce, H. (1994), Analyses of water level variations in the Strait of Çanakkale (Dardanelles), *Turkish J Eng Env Sci.*, *18*, 397–401.

- Yüce, H., and B. Alpar (1994), Investigation of low frequency sea level changes at the Strait of İstanbul (Bosphorus), *Turkish J Eng Env Sci.*, 18, 233–238.
- Zervakis, V., D. Georgopoulos, and P. G. Drakopoulos (2000), The role of the North Aegean in triggering the recent Eastern Mediterranean climatic changes, *J. Geophys. Res.*, 105, 26,103–26,116.
- Zervakis, V., D. Georgopoulos, A. P. Karageorgis, and A. Theocharis (2004), On the response of the Aegean Sea to climatic variability: A review, *Int. J. Climatol.*, 24, 1845–1858.
- Zienkiewicz, O., and R. Taylor (2000), *The Finite Element Method: The basis*, 689 pp., Butterworth-Heinemann, Oxford.
- Zienkiewicz, O. C., P. Nithiarasu, R. Codina, M. Vazquez, and P. Ortiz (1999), The characteristic-based-split (CBS) procedure: An efficient and accurate algorithm for fluid problems, *Int. J. Numer. Methods*, 31, 359–392.



## APPENDIX A

### VERTICAL RESOLUTION

The vertical resolution is high in the surface layers and decreases towards the bottom (see Table A.1).

Table A.1: Model z-layers with depths in m.

no.	1	2	3	4	5	6	7	8	9	10
depth	1	2	3	4	5	6	7	8	9	10
	11	12	13	14	15	16	17	18	19	20
	11	12	13	14	15	16	17	18	19	20
	21	22	23	24	25	26	27	28	29	30
	21	22	23	24	25	26	27	28	29	30
	31	32	33	34	35	36	37	38	39	40
	31	32	33	34	35	36	37	38	39	40
	41	42	43	44	45	46	47	48	49	50
	41	42	43	44	45	46	47	48	50	52
	51	52	53	54	55	56	57	58	59	60
	54	56	58	60	62	64	67	70	74	78
	61	62	63	64	65	66	67	68	69	70
	83	89	95	103	112	122	134	142	165	183
	71	72	73	74	75	76	77	78	79	80
	205	229	256	286	319	355	394	436	481	527
	81	82	83	84	85	86	87	88	89	80
	577	628	680	734	790	846	904	962	1021	1081
	91	92	93	94	95	96	97	98	99	100
	1141	1201	1262	1323	1384	1445	1507	1568	1630	1692
	101	102	103	104	105	106	107	108	109	110
	1754	1816	1878	1940	2002	2064	2126	2189	2200	2250

The vertical resolution used in the sensitivity experiment VERT\_0.5 (see Table A.2).

Table A.2: Model z-layers with depths in m.

no.	1	2	3	4	5	6	7	8	9	10
depth	1	4	7	10	13	16	19	22	25	28
	11	12	13	14	15	16	17	18	19	20
	31	34	37	40	43	46	50	56	62	70
	21	22	23	24	25	26	27	28	29	30
	83	89	95	103	112	122	134	149	165	183
	31	32	33	34	35	36	37	38	39	40
	205	229	256	286	319	355	394	436	481	527
	41	42	43	44	45	46	47	48	49	50
	577	680	790	904	1021	1141	1262	1384	1507	1630
	51	52	53	54	55	56	57	58	59	60
	1754	1878	2002	2126	2200	2250				

## APPENDIX B

### WATER FLUX FORMULATION

When we calculate the water balance at the surface and lateral boundaries of the model domain, we will find the fluxes  $Q(\vec{x}) = E - P - R$  as a function of horizontal position, where  $E(\vec{x})$ ,  $P(\vec{x})$  are evaporation and precipitation defined on the surface  $S$ , and  $R(\vec{x})$  is the river inflows defined on the enclosing coast  $C$ .

If we integrate over the model domain we find the total water fluxes in the model domain:

$$\int_{S_A} Q_{RA} dS + \int_{S_M} Q_{RM} dS + \int_{S_B} Q_{RB} dS = Q_R.$$

where each of the terms have components

$$\int_S Q dS = \int_S (P - E) dS + \sum_i R_i$$

where the summation is over the number of river mouths on  $C$ .

Here  $A$  is the Aegean,  $M$  is the TSS (inclusive of Marmara Sea and Bosphorus, Dardanelles Straits) and  $B$  is the Black Sea domains of the model, and the letter  $R$  denotes real fluxes. This is alternatively expressed as

$$\bar{Q}_{RA} * A_A + \bar{Q}_{RM} * A_M + \bar{Q}_{RB} * A_B = Q_R * (A_A + A_M + A_B)$$

using the bars for spatial averaging over the domain  $S$ . Because the calculated fluxes with the given  $E - P - R$  in the model domain do not necessarily add up to zero, we

will find that a net integrated flux occurs in the integrated domain over the climatic period.

However because our domain is limited and we prefer to use artificial closed boundaries at the outer boundaries of the model, we must in fact strictly impose

$$\bar{Q}_{MA} * A_A + \bar{Q}_{MM} * A_M + \bar{Q}_{MB} * A_B = 0.$$

Yet, we do not know these quantities beforehand when we initialize and start running the model. Therefore we could choose to impose at every time step

$$\bar{Q}_{MA} * A_A + \bar{Q}_{MM} * A_M + \bar{Q}_{MB} * A_B = 0,$$

so that the time integral is also satisfied. However, we note that this conservative version conflicts with the requirement in the physical world, that the sum actually adds up to  $Q_R$ , which therefore has to be re-distributed in the model.

The residual can only be assessed by actually calculating

$$Q_R = (\bar{Q}_{RA} * A_A + \bar{Q}_{RM} * A_M + \bar{Q}_{RB} * A_B) / (A_A + A_M + A_B)$$

at every time step. Therefore we need to decide how to redistribute  $Q_R$  in the three basins so that the model equivalents  $Q_{MA}$ ,  $Q_{MM}$ ,  $Q_{MB}$  add up to zero. We will decide what to do with this requirement after some other considerations.

First we note that in the entire model domain the usual surface and lateral flux boundary conditions (e.g. Tonani et al., 2008) on the transfer of water, heat, salt and momentum continue to apply, except at the falsified closed boundaries at model extremities.

The main physical constraint in the TSS model is related to the Black Sea balances which actually drive the whole TSS system, particularly because the most constraining element of the TSS, the hydraulically controlled Bosphorus Strait and its maximal exchange regime determines the outflow from the Black Sea.

The water flux balancing the Bosphorus net flux occurs over the entire domain of the

Black Sea denoted as  $GB$ , which is several times larger than the model domain  $B$ . The net flux of water in the greater Black Sea has to satisfy at the surface  $S_{GB}$

$$w = \frac{\partial \eta}{\partial t} - (P - E) \text{ on } z = 0.$$

and integrating over the model domain, taking also the lateral boundary conditions of rivers and Bosphorus flux,

$$\frac{\partial \bar{\eta}}{\partial t} = \int_{S_{GB}} (P - E) dS + \sum_{GB} R_i - Q_b.$$

where  $Q_b$  is the Bosphorus net flux. Integrating over an annual period of time, ideally we should find

$$0 = \int_0^\tau \left( \int_{S_{GB}} (P - E) dS + \sum_{GB} R_i - Q_b \right) dt.$$

where  $Q_b$  is the net flux through the Bosphorus, and also if  $\tau$  is selected to be one year, assuming there were no interannual variations.

In the above, the balance between the terms of sea level change, surface and water fluxes and the Bosphorus net flux is determined by the internal dynamics of the Bosphorus exchange flow. We also note the effects of other meteorological forcing on  $\eta$  that will determine the free surface oscillations and the consequent exit flow at the Bosphorus.

The major inconsistency between the model with Black Sea and Aegean 'boxes' with closed boundaries replacing physically open ones is that the term

$$Q_{GB} = \int_{S_{GB}} (P - E) dS + \sum_{GB} R_i$$

is not accounted for in the model, and should be artificially introduced to correctly obtain the through flow through the TSS. As a result, we propose to add these terms to the Black Sea budget, similarly for the term  $Q_B$  component due to flux contributions

from inside the model domain of the Black Sea. To choice to include these flux corrections into the model, dictates to have the  $Q_B$  component calculated in the model  $B$  domain as is done for the other regions, but to add a term to the appropriate relaxation area  $A_{Br}$ , so that

$$Q_{MB} = Q_{RB} = Q_{GB} \text{ in } A_B \text{ excluding } A_{Br},$$

$$Q_{MB} = (Q_{GB} + \bar{Q}_{GB} * (A_{GB} - A_B) / A_{Br}) \text{ in } A_{Br},$$

so that the total is

$$\begin{aligned} & \bar{Q}_{MB} * A_B \\ &= \bar{Q}_{GB} * (A_B - A_{Br}) + (\bar{Q}_{GB} + \bar{Q}_{GB} * (A_{GB} - A_B) / A_{Br}) * A_{Br} \\ &= \bar{Q}_{GB} * A_{GB}. \end{aligned}$$

In the Marmara Sea area,

$$Q_{MM} = Q_{RM} \text{ in } A_M,$$

is applied without change.

Finally we have to adjust the Aegean region in such a way to account for all the discrepancies coming from the Black Sea or the net flux of the model domain in order to make the net fluxes over the domain vanish at every time:

$$Q_{MA} = Q_{RA} \text{ in } A_A \text{ excluding } A_{Ar},$$

$$Q_{MA} = (Q_{RA} - \bar{Q}_{GB} * (A_{GB} - A_B) / A_{Br} - Q_R * (A_B + A_M + A_B)) \text{ in } A_A$$

There is also the specific requirement that the water input / output at the relaxation regions should be of the same salinity and temperature as the resident surface water, in order that anomalous waters would end up in the TSS.







# CURRICULUM VITAE

## PERSONAL INFORMATION

**Surname, Name:** Gürses, Özgür

**Nationality:** Turkish (TC)

**Date and Place of Birth:** 23.07.1978, Kayseri

**Marital Status:** Married

**Phone:** 0 324 5212406

**Fax:** 0 324 5212327

## EDUCATION

<b>Degree</b>	<b>Institution</b>	<b>Year of Graduation</b>
M.S.	TUM, Computational Engineering, Munich	2006
B.S.	METU, Civil Engineering, Ankara	2003
High School	Batikent Lisesi, Ankara	1996

## PROFESSIONAL EXPERIENCE

<b>Year</b>	<b>Place</b>	<b>Enrollment</b>
2013–2015	INGV, Bologna	Research Collaborator
2010–2013	AWI, Bremerhaven	Helmholtz Scholar
2008–2013	IMS-METU, Erdemli	Research Assistant

## **PUBLICATIONS**

### **Master Thesis**

Thesis Title: *On MpCCI as a coupling library for fluid-structure interaction with CFX.*

### **Publications (INTERNATIONAL)**

#### **Journal Papers**

Gürses Ö. , Aydocgdu A., Pinardi N., Özsoy E. (2015), A Finite Element Modeling Study of the Turkish Straits System, Ocean Dynamics, submitted

Crise A., Kaberi H., Ruiz J., Zatsepin A., ..., Gürses Ö, ..., Papathanassiou E. (2015), A MSFD complementary approach for the assessment of pressures, knowledge and data gaps in Southern European Seas: The PERSEUS experience, Marine Pollution Bulletin, 95, 28–39

#### **Conference Publications**

Özsoy, E., Sözer, A., Gürses, Ö., Gündüz, M. and G. Sannino, Nonlinear Hydrodynamics of the Atmosphere and Ocean, with Examples from Sea Straits. "Turkish Nonlinear Science Working Group, XIV. International Symposium on "Disorder Systems"", 2014

Özsoy E., Gürses Ö. , Tutsak E., "Turkish Straits System And Southern Black Sea: Exchange. Mixing And Shelf/Canyon Interactions", European Geosciences Union General Assembly, 2015

Özsoy E., Sannino G., Sözer A., Gürses Ö. "A Review of the Turkish Strait System: Challenges for Modeling, Inter-Basin Coupling and the Environment", European Geosciences Union General Assembly, 2015

## **Publications (NATIONAL)**

### **Conference Publications**

Özsoy, E., Sözer, A., Gürses, Ö., Gündüz, M., Tutsak, E. and G. Sannino, The Leading Role of the Turkish Straits System in Ocean Science and the Environmental Degradation Imposed on Unique Natural-Cultural Heritage by Canal İstanbul. "İstanbul'un Jeolojisi Sempozyumu 4", 2014

### **Book and Chapter in a Book**

Tutsak, E., Sözer, A., Gürses, Ö., Özsoy, E., Turkish Straits System Observation and Forecast Systems. "Proceedings of the Symposium "The Marmara Sea 2010"", 2010